

1 Distributed control circuits across a brain-and-cord connectome

2

3 Alexander Shakeel Bates^{1,2,*}, Jasper S. Phelps^{1,3,*}, Minsu Kim^{1,4,5,*}, Helen H. Yang^{1,*}, Arie Matsliah^{6,†}, Zaki
4 Ajabi^{1,†}, Eric Perlman^{7,†}, Kevin M. Delgado^{1,†}, Mohammed Abdal Monium Osman^{1,†}, Christopher K. Salmon⁶,
5 Jay Gager⁶, Benjamin Silverman⁶, Sophia Renauld¹, Matthew F. Collie¹, Jingxuan Fan¹, Diego A. Pacheco¹,
6 Yunzhi Zhao¹, Janki Patel¹, Wenyi Zhang¹, Laia Serratosa Capdevilla⁸, Ruairí J.V. Roberts⁸, Eva J. Munnely⁸,
7 Nina Griggs⁸, Helen Langley⁸, Borja Moya-Llamas⁸, Ryan T. Maloney^{9,10,11}, Szi-chieh Yu⁶, Amy R. Sterling⁶,
8 Marissa Sorek⁶, Krzysztof Kruk¹², Nikitas Serafetinidis¹², Serene Dhawan⁶, Tomke Stürner¹³, Finja Klemm¹⁴,
9 Paul Brooks¹⁵, Ellen Lesser¹⁶, Jessica M. Jones¹⁷, Sara E. Pierce-Lundgren¹⁷, Su-Yee Lee¹⁷, Yichen Luo¹⁷,
10 Andrew P. Cook¹⁸, Theresa H. McKim¹⁹, Emily C. Kophs²⁰, Tjalda Falt²¹, Alexa M. Negrón Morales²², Austin
11 Burke⁶, James Hebditch⁶, Kyle P. Willie⁶, Ryan Willie⁶, Sergiy Popovych²³, Nico Kemnitz²³, Dodam Ih²³, Kisuk
12 Lee²³, Ran Lu²³, Akhilesh Halageri²³, J. Alexander Bae²³, Ben Jourdan²⁴, Gregory Schwartzman²⁵, Damian D.
13 Demarest²⁶, Emily Behnke⁶, Doug Bland¹², Anne Kristiansen¹², Jaime Skelton¹², Tom Stocks¹², Dustin Garner¹²,
14 Farzaan Salman^{18,27}, Kevin C. Daly^{18,28}, Anthony Hernandez¹², Sandeep Kumar⁶, The BANC-FlyWire
15 Consortium[^], Sven Dorkenwald²⁹, Forrest Collman²⁹, Marie P. Suver²⁰, Lisa M. Fenk²¹, Michael J. Pankratz²⁶,
16 Gregory S.X.E. Jefferis¹³, Katharina Eichler¹⁴, Andrew M. Seeds²², Stefanie Hampel²², Sweta Agrawal³⁰, Meet
17 Zandawala^{31,32}, Thomas Macrina²³, Diane-Yayra Adjavon³³, Jan Funke³³, John C. Tuthill¹⁷, Anthony Azevedo¹⁷,
18 H. Sebastian Seung^{6,34}, Benjamin L. de Bivort^{9,10}, Mala Murthy^{6,*}, Jan Drugowitsch^{1,*}, Rachel I. Wilson^{1,*},
19 Wei-Chung Allen Lee^{1,35,*}

20

21 ¹Department of Neurobiology, Harvard Medical School, Boston, MA, USA

22 ²Centre for Neural Circuit and Behaviour, University of Oxford, Oxford, UK

23 ³Present address: Neuroengineering Laboratory, Brain Mind Institute and Institute of Bioengineering, EPFL, Lausanne, Switzerland

24 ⁴Present address: Department of Molecular and Cellular Biology, Harvard University, Cambridge, MA, USA

25 ⁵Present address: Center for Brain Science, Harvard University, Cambridge, MA, USA

26 ⁶Princeton Neuroscience Institute, Princeton University, Princeton, NJ, USA

27 ⁷Yikes LLC, Baltimore, MD, USA

28 ⁸Aelysia LTD, Bristol, UK

29 ⁹Department of Organismic and Evolutionary Biology, Harvard University, Cambridge, MA, USA

30 ¹⁰Center for Brain Science, Harvard University, Cambridge, MA, USA

31 ¹¹Present address: Psychology Department, Colorado College, Colorado Springs, CO, USA

32 ¹²Eyewire, Boston, MA, USA

33 ¹³Neurobiology Division, MRC Laboratory of Molecular Biology, Cambridge, UK

34 ¹⁴Genetics Department, Leipzig University, Leipzig, Germany

35 ¹⁵Zoology Department, University of Cambridge, Cambridge, UK

36 ¹⁶Department of Molecular Genetics and Cell Biology, The University of Chicago, Chicago, IL, USA

37 ¹⁷Department of Neurobiology and Biophysics, University of Washington, Seattle, WA, USA

38 ¹⁸Department of Biology, West Virginia University, Morgantown, WV, USA

39 ¹⁹Department of Biology, University of Nevada Reno, Reno, NV, USA

40 ²⁰Department of Biological Sciences, Vanderbilt University, Nashville, TN, USA

41 ²¹Max Planck Institute for Biological Intelligence, Martinsried, Germany

42 ²²Institute of Neurobiology, University of Puerto Rico Medical Sciences Campus, San Juan, Puerto Rico

43 ²³Zetta AI LLC, Sherrill, NY, USA

44 ²⁴School of Informatics, University of Edinburgh, Edinburgh, UK

45 ²⁵Japan Advanced Institute of Science and Technology (JAIST), Nomi, Japan

46 ²⁶Molecular Brain Physiology and Behavior, LIMES Institute, University of Bonn, Bonn, Germany

47 ²⁷Present address: Department of Neurobiology, Harvard Medical School, Boston, MA, USA

48 ²⁸Department of Neuroscience, West Virginia University, Morgantown, WV, USA

49 ²⁹Allen Institute for Brain Science, Seattle, WA, USA

50 ³⁰School of Neuroscience, Virginia Tech, Blacksburg, VA, USA

51 ³¹Department of Biochemistry and Molecular Biology, University of Nevada Reno, Reno, NV, USA

52 ³²Neurobiology and Genetics, Theodor-Boerner-Institute, Biocenter, Julius-Maximilians-University of Würzburg, Am Hubland, Würzburg, Germany.

53 ³³HHMI Janelia, Ashburn, VA, USA

54 ³⁴Computer Science Department, Princeton University, Princeton, NJ, USA

55 ³⁵F.M. Kirby Neurobiology Center, Boston Children's Hospital, Harvard Medical School, Boston, MA, USA

56

57 * These authors contributed equally to this work

58 † These authors contributed equally to this work

59 ^A list of additional members and their affiliations appears in The BANC-FlyWire Consortium

60 [✉]Correspondence: Alexander_Bates@hms.harvard.edu, jasper.s.phelps@gmail.com, mmurthy@princeton.edu,

61 jan_drugowitsch@hms.harvard.edu, rachel_wilson@hms.harvard.edu, wei-chung_lee@hms.harvard.edu

62 Abstract

63 Just as genomes revolutionized molecular genetics, connectomes (maps of neurons and synapses) are
64 transforming neuroscience. To date, the only species with complete connectomes are worms^{1–3} and sea
65 squirts⁴ (10^3 - 10^4 synapses). By contrast, the fruit fly is more complex (10^8 synaptic connections), with a brain
66 that supports learning and spatial memory^{5,6} and an intricate ventral nerve cord analogous to the vertebrate
67 spinal cord^{7–11}. Here we report the first adult fly connectome that unites the brain and ventral nerve cord, and
68 we leverage this resource to investigate principles of neural control. We show that effector cells (motor
69 neurons, endocrine cells and efferent neurons targeting the viscera) are primarily influenced by local sensory
70 cells in the same body part, forming local feedback loops. These local loops are linked by long-range circuits
71 involving ascending and descending neurons organized into behavior-centric modules. Single ascending and
72 descending neurons are often positioned to influence the voluntary movements of multiple body parts, together
73 with endocrine cells or visceral organs that support those movements. Brain regions involved in learning and
74 navigation supervise these circuits. These results reveal an architecture that is distributed, parallelized and
75 embodied (tightly connected to effectors), reminiscent of distributed control architectures in engineered
76 systems^{12,13}.

77 Main

78 A coherent understanding of the embodied nervous system remains a central challenge of neurobiology. The
79 fruit fly *Drosophila melanogaster* is the most complex organism for which this milestone is currently within
80 reach. Recent work has yielded connectomes for the adult *Drosophila* brain^{14–17} and ventral nerve cord
81 (VNC)^{7–11}. These structures are analogous to the brain and spinal cord of vertebrates, but they contain fewer
82 neurons, making them tractable for complete connectomes (brain: ~140,000 neurons, VNC: ~20,000 neurons).
83 The fly brain and VNC are connected by ~1300 descending neurons (DNs)^{18–21} and ~1900 ascending neurons
84 (ANs)^{21–25}. However, the existing fly brain^{14–17} and VNC^{7–11} connectomes were collected separately, and so DNs
85 and ANs are fragmentary in these datasets, though cross-mapping of some cell types have allowed some
86 ‘bridging’ analyses²¹. A unified *Drosophila* connectome would allow us to trace the pathways that connect the
87 brain, VNC and body.

88

89 Such a connectome would also shed light on the architecture of behavioral control. Different regions of the
90 central nervous system (CNS) have specialized functions—and this is true in arthropods just as in
91 vertebrates²⁶—but we lack a detailed understanding of the overall control architecture in any complex neural
92 system. In principle, behavioral control might flow through a central pathway for perception, action selection
93 and motor coordination; alternatively, it might be decentralized and distributed across many feedback control
94 modules that are loosely coupled in a hierarchical manner. These alternative scenarios are debated in the
95 literature on vertebrate intelligence, insect intelligence and artificial intelligence^{13,27–29}. A unified adult *Drosophila*
96 connectome would place important constraints on this debate. Adult flies are also limbed organisms that solve
97 many of the basic control problems that confront other limbed species, including vertebrates³⁰.

98

99 In this study, we describe the first unified and embodied brain-and-cord connectome of an adult fly. To analyze
100 this dataset, we develop an influence metric to predict the functional connection between any pair of cells, and
101 we apply this at scale to the entire nervous system. We show that the strongest influences on effectors (motor
102 neurons, endocrine cells and efferent neurons targeting the viscera) are generally local sensory signals,
103 forming a distributed set of tight feedback loops. Long-range connections involving ANs and DNs coordinate
104 these local loops. Many of these AN/DN circuits can be linked to specific behaviors, such as escape, feeding,
105 reproduction and locomotion. We describe the interactions between these circuits, and we explicitly link these
106 circuits to supervisory brain regions involved in learning and navigation. Our results establish clear empirical
107 support for theories of behavioral control organized around distributed sensory-motor modules, where
108 “cognitive” regions are supervisory but not essential for action.

109 Results

110 An open-source brain-and-nerve-cord connectome

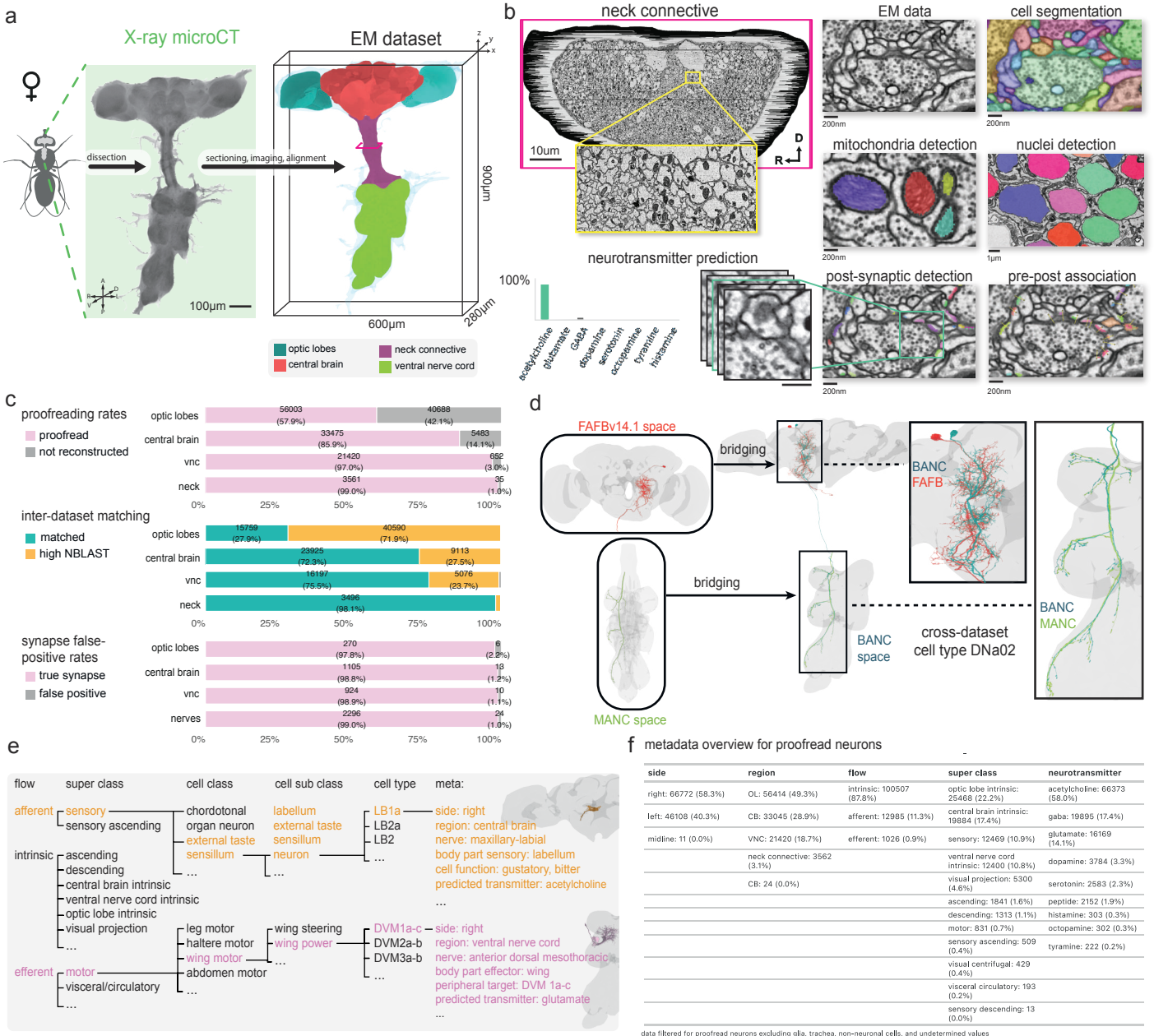
111 We generated a serial-section electron microscopy (EM) volume comprising the CNS of an adult female *D.*
112 *melanogaster* at synapse resolution ($4 \times 4 \times 45 \text{ nm}^3$) (**Fig. 1a**). Using our semi-automated sectioning and imaging
113 platform (GridTape⁷) (**Extended Data Fig. 1a**), we collected 7,010 serial sections onto film-coated tape,
114 compatible with transmission EM. This approach enabled visualization of fine neural processes (<200 nm),
115 synaptic vesicles (~40 nm) and synaptic clefts (~10 nm). After imaging each section, we computationally
116 reassembled the entire Brain and Nerve Cord dataset (BANC, pronounced “bank”) into a 3D volume^{8,31}. We
117 then used convolutional neural networks (CNNs) to automatically segment and reconstruct individual cells^{8,31},
118 nuclei, and mitochondria (**Fig. 1b**). To proofread and annotate the expected ~160,000 neurons^{10,15} in the
119 dataset, we followed the approach created by FlyWire for the whole-brain connectome (FAFB-FlyWire)^{15,32,33}.
120 We used automatically identified nuclei to account for all neurons with their cell bodies in the CNS. For neurons
121 with cell bodies outside the CNS (e.g., sensory neurons), we manually identified 48 nerves^{34–37} and verified that
122 each axon in these nerves was associated with a segmented neuron. For neurons traversing the neck
123 connective, we verified that every axon at both anterior and posterior neck levels was associated with a
124 segmented neuron. A team of 155 proofreaders corrected errors in the automatic segmentation over about 2
125 years, a total effort of ~30 work-years (**Fig. 1c**).
126

127 We assigned cell type labels by automatically identifying potential matches between BANC neurons and earlier
128 datasets^{8–10,14,15,17,38}, based on neuron morphology and position (using NBLAST³⁹, **Fig. 1c-e, Extended Data**
129 **Fig. 1b**) and based on connectivity⁴⁰ (A.M., C.K.S., et. al., in preparation). We then manually reviewed and
130 corrected these cell type matches; this process is largely complete but is still ongoing in the left optic lobe (**Fig.**
131 **1c**). Some neurons are still not cross-matched (26% of BANC neurons excluding the optic lobes), and some of
132 these neurons likely cannot be matched even with more effort, due to inter-individual variability in cell
133 morphology^{41–43}. Inter-individual variability can result from genetic variation, developmental noise and
134 limitations in data quality or reconstruction. Importantly, in the course of making cell type assignments, we
135 generated the first comprehensive accounting of DN and AN cell types, and we matched AN/DN cell-type
136 labels across the existing whole-brain connectome¹⁵ and VNC connectomes^{8–10}.
137

138 To automatically identify synapses in the BANC, we trained another CNN^{44,45} to predict pre- and postsynaptic
139 locations with high accuracy (F-score: .79, precision: .68, recall: .95; **Fig. 1b,c, Extended Data Fig. 1c**).
140 Overall, 65% of detected presynaptic links are attached to identified cells (**Extended Data Fig. 1d,e**).
141 Comparing the normalized synaptic count between all pairs of cross-matched, identified cell types in the CNS
142 revealed strong concordance between the BANC and other adult fly connectomes (**Extended Data Fig. 1f**).
143

144 We used another CNN to predict the neurotransmitter released by each neuron⁴⁶. Our identifications of neurons
145 releasing acetylcholine, glutamate, GABA, dopamine, serotonin and octopamine largely agree with previous
146 predictions⁴⁶. We also used this approach to identify cells that release tyramine and histamine, which have not
147 been previously incorporated into automatic neurotransmitter predictions (**Extended Data Fig. 1g**).
148

149 Next, we identified many cell types linking the CNS with the rest of the body (**Fig. 1c-f**). To do so, we annotated
150 BANC cells based on literature review, neuron matching and refined labels from prior connectomes. For
151 example, we identified motor neurons targeting muscles of the limbs, antennae, eyes, neck, crop, pharynx,
152 proboscis, salivary glands and uterus^{8,10,47–54}. We found putative sensory nociceptors from the abdomen¹⁰ (J.J.
153 & J.C.T., in preparation), sensory neurons from the aorta⁵⁵, the cibarium⁵⁶ (the pre-oral food chamber), putative
154 oxygen-sensing neurons in the abdomen^{57,58} and sensory neurons from the abdominal terminalia^{52,59}. We
155 identified multiple distinct types of endocrine cells in the brain and VNC, many of which could be matched with
156 the neuropeptides they release^{58,60–64} and their sites of action, including the ureter^{65,66}, neurohemal release
157 sites, the digestive tract^{55,67}, and the reproductive tract^{68–70}. We also identified chemosensory, tactile and
158 proprioceptive afferents from the head, eyes, antennas, proboscis, legs, abdomen, wings and halteres^{10,37,71–75}.
159 Taken together, these cell type identifications make the BANC a highly ‘embodied’ connectome, with explicit
160 connections to specific muscles, sense organs and viscera throughout the body.



161

162 **Figure 1: An open-source brain-and-nerve-cord connectome.**

163 a. (*left*) X-ray micro-computed tomography (microCT) projection of the BANC sample following dissection, staining, and embedding for
 164 EM. (*right*) Surface mesh rendering of the CNS EM dataset with regions colored. A: anterior, P: posterior, D: dorsal, V: ventral, L: left,
 165 R: right.
 166 b. (*top left*) Aligned EM micrographs through a cross-section of the neck connective ([y=92500](#)) (magenta box in (a)). D: dorsal, R: right.
 167 (*yellow box*) Zoom-in of the EM data. (*columns to right*) Example EM image data from the BANC dataset. Neurons were automatically
 168 segmented using convolutional neural networks (CNNs)^{31,76}, with each segmented cell shaded with a different color. Mitochondria ([x:
 169 137533, y: 35220, z: 2493](#)) and nuclei ([x: 192977, y: 51679, z: 2493](#)) (both overlaid with different colors) were segmented⁷⁷.
 170 Postsynaptic locations (shaded with different colors, example: [x: 140988, y: 36705, z: 2498](#)) were automatically predicted and
 171 presynaptic locations (end of yellow lines) were automatically assigned using CNNs⁴⁵. (*bottom left*). The predicted neurotransmitter
 172 for the selected synapse (center of the green box) is acetylcholine.
 173 c. (*top*) Fraction of proofread neurons in gross divisions of the CNS. Neurons are labeled as proofread when their primary neurites or
 174 'backbones' have been reviewed¹⁵. (*middle*) Fraction of proofread neurons in the BANC matched with neurons in other connectomes,
 175 by gross divisions of the CNS. Morphological cell type level matches were confirmed by experts (teal), or matched to a likely class
 176 based on high NBLAST scores³⁹. (*bottom*) Fraction of true and false positive synapse predictions in different divisions of the CNS.
 177 Full CNS inventory inferred from summing counts from FAFB and MANC, and subtracting photoreceptors not captured by BANC
 178 (11468).
 179 d. Neurons were matched to metadata from previous projects by transforming their morphologies from other connectomes^{8,10,11,14,15,17}
 180 into BANC space⁷⁸. We used NBLAST³⁹ to identify potential morphological matches. An example with DN02 is shown, illustrating the
 181 process. [Neuroglancer link](#) for morphology, [Codex link](#) for metadata/connectivity.
 182 e. Hierarchy of cell annotations, based on previous work^{17,79}, but adopting clearer terms. Exemplified for LB1a ([Neuroglancer link](#),
 183 [Codex search](#)) and DVm1a-c ([Neuroglancer link](#), [Codex search](#)). See (**Supplementary Data 1**).
 184 f. The proportion of proofread neurons (of 114518) in the BANC by metadata label. Fast-acting neurotransmitter identities are assigned
 185 by our native BANC neurotransmitter predictions, based on⁴⁶. The 'peptide' class was added in cases where evidence from the
 186 literature supports neuropeptide expression, but our prediction is for a monoamine. In these cases we suspect the predictions are
 187 more likely to be incorrect⁴⁶.

188 Our ability to describe all these connections relied crucially on BANC being an open science effort³² since July
189 2023, and this project continues to grow with ongoing community input. Users can visualize the latest version
190 of our data via Neuroglancer⁸⁰ and add annotations through CAVE³³. Users can also browse metadata and
191 connectivity data via FlyWire Codex¹⁵ (codex.flywire.ai/banc) and CAVE³³, as well as programmatically⁷⁸ and
192 via direct downloads⁸¹ (**Extended Data Fig. 1h,i**). We have also modified typology annotations for the
193 whole-brain (FAFB) and VNC (MANC) connectomes^{10,11,15–17} to facilitate comparisons between these datasets
194 and our work in BANC (**Supplementary Data 1-3**).

195 A metric of influence

196 To interpret a whole-CNS connectome, we need a way to estimate the influence of cell A on cell B, for any pair
197 of cells. To date, there has been no computationally efficient method of estimating these influences. Efficiency
198 is crucial, as there are billions of pairwise interactions between cells in the full CNS. It would be ideal to
199 precompute all these influences, so that users can simply query any cell pair of interest.

200

201 To tackle this problem, we developed an approach based on linear dynamical modeling^{82–85}. Specifically, to
202 compute the influence of one or more source neurons on any target neuron(s), we simulate the effect of
203 injecting a sustained step of activity into the source neurons, taking every downstream neuron's activity as the
204 weighted sum of its inputs. The weight is the number of synapses in that input connection⁸⁶, as a fraction of the
205 postsynaptic cell's total synaptic input. For a target cell of interest, we take its steady-state activity (**Fig. 2a**),
206 log-transform it, and add a constant to ensure that the result is nonnegative. The metric (called 'adjusted
207 influence') is approximately linear with network distance from source to target (**Fig. 2b, Extended Data Fig.**
208 **2a**). Indeed, adjusted influence is in excellent agreement with previous network distance metrics^{15,22,41}. Like
209 previous distance metrics^{15,22,41}, adjusted influence is an unsigned quantity. However, unlike those metrics, our
210 metric is deterministic, linear and scalable. This allowed us to precompute the pairwise adjusted influence of all
211 individual neurons in the entire CNS onto all other individual neurons, yielding 24 billion scores in total. Across
212 the CNS, the modal adjusted influence score is 14 for direct connections and 8 for indirect connections (**Fig.**
213 **2c**). All scores are available to users via codex.flywire.ai/banc.

214

215 In the following sections, we say A "influences" B, as shorthand for a high adjusted influence score (A→B).
216 These scores do not demonstrate functional connections, and they are no substitute for experiments. The
217 value of these scores is that they allow us to make provisional inferences on a large scale. In the sections that
218 follow, we will use influence scores to make inferences, and to bolster these inferences, we will show example
219 circuit motifs. These inferences are merely predictions, and their value is to generate testable hypotheses.

220 Modules for local feedback control

221 Other large-scale connectome analyses have focused mainly on cells deep in the CNS^{5,6,87}. Here, we take a
222 complementary approach; we start by focusing on sensors and effectors. A 'sensor' is a presumptive peripheral
223 sensory neuron (either external or internal) and an 'effector' is a presumptive motor neuron, endocrine cell, or
224 an efferent neuron targeting the viscera (**Fig. 2d**). Importantly, sensors are distributed across the body, and
225 effectors are widely distributed as well: the brain contains motor neurons that control the eyes, antennae,
226 mouth parts, as well as the foregut⁸⁸, while the VNC contains motor neurons that control the limbs, abdomen,
227 reproductive organs, and hindgut⁷. Similarly, endocrine cells are found in both the brain and the VNC^{89,90}. As an
228 embodied brain-and-VNC connectome, the BANC offers a new opportunity to reconsider sensor-effector
229 relationships.

230

231 As a general rule, we found that effector cells receive their strongest influence from sensors in the same body
232 part (**Fig. 2e**). To take an arbitrary example, we find that pharynx motor neurons are most strongly influenced
233 by pharynx sensory cells. Ongoing pharynx movements will also immediately alter the activity of pharynx
234 sensory neurons, and so these motor neurons form a tight reciprocal feedback loop with local sensory neurons
235 (**Fig. 2f**). Local feedback is useful because it minimizes delays^{71,91,92}. Previous work has described local
236 feedback loops in proboscis control⁴⁷, enteric control⁵⁵, and VNC premotor networks^{9,93}, and our analysis
237 extends this work to argue that tight local feedback is a systematic principle across the CNS.

238

239 At the same time, the BANC dataset also shows that each local loop is influenced by a select group of more
240 distant sensors (**Fig. 2e**). For example, pharynx motor neurons are influenced by sensors in the labellum,
241 cibarium, crop, and abdomen. These longer-range connections can also be seen as forming feedback loops:
242 for example, pharynx movements during feeding should trigger not only immediate sensory signals in the
243 pharynx, but also more delayed changes in sensory signals along the length of the gastrointestinal tract, which
244 might then (for example) limit feeding if the gut is filling too quickly (**Fig. 2f**). In this way, long-range loops can
245 provide important feedback signals that local loops cannot directly access⁹¹. The BANC dataset shows that
246 long-range influences are generally weaker than local influences (**Fig. 2e**), and this implies that local loops are
247 the core elements of behavioral control, with a secondary role for long-range loops.

248 Linking DNs and ANs to effectors

249 Thus far, we have seen evidence for strong local feedback loops. These local loops are linked by selective
250 longer-range sensory-motor connections. To better understand these long-range connections, we focused on
251 the neurons that link the brain with the VNC, namely DNs and ANs.
252

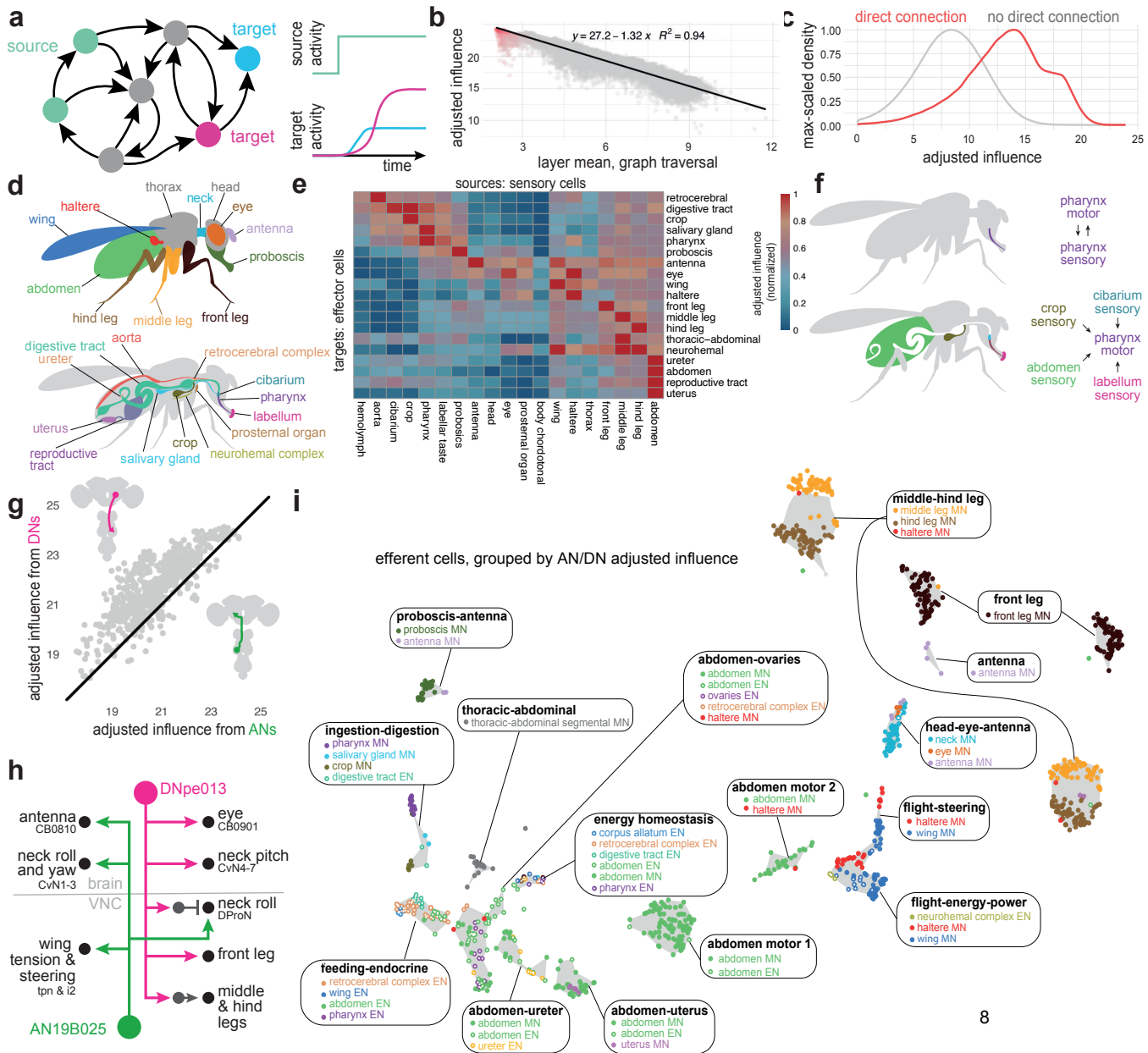
253 It is sometimes suggested that DNs send motor commands from the brain to the VNC, whereas ANs send
254 sensory signals and predictive motor signals back from the VNC to the brain^{24,94}. But recent work has shown
255 that ANs can also form output synapses in the VNC^{9,10}, while DNs can form output synapses in the brain^{21,95}.
256 The BANC dataset allows us to reconstruct DNs and ANs comprehensively, and it shows clearly that both DNs
257 and ANs have substantial output in both the brain and the VNC (**Extended Data Fig. 2b,c**). Moreover, the
258 BANC dataset shows that most effector cells are influenced by both DNs and ANs (**Fig. 2g**). The majority of
259 individual DNs exert influence over effector cells in multiple body parts, and the same is true of ANs (**Extended**
260 **Data Fig. 2d-g**). For example, DNpe013 influences motor neurons in the eyes, neck and legs, whereas
261 AN19B025 influences motor neurons controlling the eyes, antennae, neck and wings (**Fig. 2h**). Together, all
262 these observations imply that DNs and ANs work together to coordinate motor patterns and internal organs in
263 different body parts.
264

265 Next, we asked how DNs and ANs organize effector cells. We computed the influence of every DN and AN on
266 every effector cell, and we divided effector cells into groups according to the influence they receive. This
267 effector cell map (**Fig. 2i, Extended Data Fig. 2h**) identifies sets of coordinated motor neurons and endocrine
268 neurons. For example, this map shows DNs and ANs co-regulate pharynx motor neurons, salivary gland motor
269 neurons, crop motor neurons, and endocrine cells of the digestive tract; we call this the “ingestion-digestion
270 group”. Similarly, DNs and ANs coordinate wing power motor neurons, haltere motor neurons and endocrine
271 cells of the neurohemal complex; we call this the “flight-energy-power group”. As these examples illustrate,
272 DNs and ANs often unite cells in different body parts (**Fig. 2i**).
273

274 To recap, we find that many individual DNs and ANs have distributed patterns of influence over effector cells.
275 Both DNs and ANs are positioned to coordinate the actions of effectors across the body. Finally, DNs and ANs
276 coordinately control distinct groups of endocrine cells and motor neurons, allowing the body’s internal state to
277 be coordinated with specific motor patterns.

278 Clustering DNs and ANs into behavior-centric modules

279 To identify functional divisions among DNs and ANs, we constructed a map of these neurons based on their
280 direct synaptic connections, both pre- and postsynaptic (**Fig. 3a**). DNs and ANs are intermingled in this map
281 because, as it turns out, their connections are often similar. We verified that cells with similar known functions
282 are frequently colocalized on this map (**Fig. 3b, Extended Data Fig. 3a-c**; DNs and ANs with known functions
283 are taken from previous work^{9,20,21,24,70,95–126}). We then assessed the influence associated with different AN/DN
284 clusters, considering both influence from sensors and influence onto effectors (**Fig. 3c; Extended Data Fig.**
285 **3d-f**). Based on this information, we grouped related clusters of DNs and ANs into superclusters (**Extended**
286 **Data Fig. 4**). Most individual superclusters are influenced by multiple sensory organs (**Fig. 3d**), and they exert
287 influence onto multiple effector organs (**Fig. 3e**). Based on these influences, as well as known cells, we were
288 able to link each supercluster with a putative behavior (**Fig. 3f**).
289



290 **Figure 2: Linking sensors and effectors through local and long-range circuits.**

- 291 a. The influence of source cells on target cells is estimated via linear dynamical modeling.
292 b. Adjusted influence (see Methods) is proportional to the number of network 'layers' in a graph traversal model⁴¹. Direct and
293 indirect connections are shown in red and gray, respectively. Here the source neurons are olfactory receptor neurons in the
294 FAFB dataset, following previous work¹⁷, and adjusted influence is averaged over the number of neurons in the source and
295 target groups. Regression line in black ($R^2=0.94$, $n = 94278$).
296 c. Distribution of adjusted influence scores between all ANs (1841) and DNs (1313) and all other neurons (155936) in the
297 dataset. Direct and indirect connections are shown in separate histograms, with the peak of each histogram normalized to its
298 own maximum.
299 d. Schematic of body parts associated with annotated effector cells in the BANC. Not all neurohemal organs shown.
300 [Neuroglancer link](#), explore on [Codex here](#).
301 e. Mean adjusted influence of sensory cells (columns) on effector cells. Sensory and effector cells are pooled by body part. Each
302 row is minmax normalized to the same range (0-1). This plot summarizes data from 14410 sensory cells and 1026 effector
303 cells. We omitted 3188 putative sensory cells whose corresponding organs could not be identified.
304 f. Schematic: an example local loop (top) that is also linked to specific sensors via long-range connections (bottom).
305 g. Scatterplot showing the mean adjusted influence on each effector cell from DNs versus ANs. Black, unity line. Insets: a DN
306 soma is located in the head, whereas an AN soma is located in the body.
307 h. An example AN and DN with strong adjusted influence on effector cells in multiple body parts. [Neuroglancer link](#), [Codex](#)
308 [network](#).
309 i. UMAP embedding of effector cells, based on the cosine similarity between the adjusted influences these cells receive from
310 individual ANs and DNs. The major cell types in each effector cell group are listed (MNs, 833 motor neurons; ENs, 193
311 endocrine neurons some of which are putative). [Neuroglancer link](#), [Codex search](#). See **(Supplementary Data 5)**.

312 For example, one supercluster is most likely associated with threat response behaviors. This supercluster
313 contains all the known DNs associated with escape takeoff (**Fig. 3b**), as well as many DNs and ANs with
314 unknown functions. As a group, these DNs and ANs are influenced by visual loom detectors, visual small
315 object detectors, and specific mechanoreceptors (**Fig. 3d**). They output to endocrine neurons that regulate
316 internal state, as well as wings and leg motor neurons. All this is consistent with the idea that these DNs and
317 ANs trigger reiative maneuvers, while also recruiting the energy stores needed to support these maneuvers
318 (**Fig. 3e**).
319

320 Another supercluster is most likely involved in reproductive behaviors. As a group, these cells are influenced by
321 tactile sensors, taste sensors, and nociceptors (**Fig. 3d**). They influence the uterus and reproductive tract, as
322 well as neurohemal complexes, which release signals into the circulatory system (**Fig. 3e**).
323

324 Using a similar process of inference, we linked other superclusters with walking, walking steering, flight
325 steering, flight power, head-and-eye-orienting, grooming, landing, visceral control, feeding, and probing (**Fig.**
326 **3f**). The term “probing” refers to tactile sampling prior to feeding initiation¹²⁷; we propose that this behavior is
327 mediated by the supercluster receiving strong input from labellar tactile afferents and external taste sensors
328 (**Fig. 3d**), and exerting coordinated influence over the forelegs, proboscis and pharynx (**Fig. 3e**). Meanwhile,
329 we suggest that a distinct supercluster is associated with feeding: this supercluster receives the highest
330 influence from internal taste sensors (**Fig. 3d**), and it has strong influence over the pharynx, crop, and salivary
331 glands, as well as endocrine cells targeting the digestive tract (**Fig. 3e**). The influence of the feeding cluster is
332 strongly correlated with the overall influence of pharynx taste and leg taste receptors (**Extended Data Fig. 3f**).
333

334 The visceral control supercluster contains ANs and DNs that seem to coordinate endocrine cells in different
335 body parts (**Fig. 3e**). **Fig. 3g** shows an example circuit involving cells from this supercluster. In this circuit,
336 AN27X017 relays signals from putative abdominal oxygen sensors⁵⁸ (Y.L. and J. T., in preparation) directly to
337 brain endocrine cells that release insulin-like peptide (DILP), which regulates feeding¹²⁸; these ANs converge
338 with the projections of aorta sensory neurons⁵⁵. Meanwhile, AN27X017 also synapses onto DNp65, which
339 targets abdominal leukokinin neurons that regulate feeding and diuresis¹²⁹. This circuit might regulate energy
340 and water balance during physical stress.
341

342 Any attempt to put DNs and ANs into categories involves some over-simplification, as many of these cells
343 seem to have multiple functions. Consider, for instance, DNg27, in the flight power supercluster (**Fig. 3h**). This
344 DN synapses onto wing power motor neurons, as well as brain endocrine neurons that release corazonin
345 (which mobilizes energy stores^{58,130}). Thus, this DN is positioned to increase flight power, while also releasing
346 energy needed to sustain flight. Some of the excitatory drive to DNg27 comes from interoceptive neurons in the
347 brain that are suppressed by thirst^{118,131}; this connection may help control flight power based on water balance,
348 because high flight power involves high metabolic demand, and thus water loss via respiration¹³². Meanwhile,
349 the same corazonin neurons downstream from DNg27 are postsynaptic to ANXXX139, an AN in the visceral
350 control supercluster that is positioned to relay signals from putative nociceptors. This AN may respond to
351 painful stimuli by recruiting energy reserves, to prepare for struggle or escape. Like many DNs and ANs, these
352 cells are multi-functional.
353

354 Within a given supercluster, ANs and DNs can sometimes form extended loops. An example in the
355 reproduction supercluster involves SAG-ANs¹¹¹. The BANC connectome shows that these cells are
356 downstream from sensory neurons in the uterus, oviduct, and spermatheca (**Fig. 3i**), consistent with their
357 known role as monitors of the reproductive tract¹¹¹. SAG-ANs signal to pC1 cells in the female brain^{70,111}, which
358 lie upstream from several DNs in the female reproduction supercluster, including oviDNA_a⁷⁰ and DNp37¹³³.
359 DNp37 is positioned to regulate uterine motor neurons⁵², whereas oviDNA_a is positioned to modulate
360 ascending sensory signals from the uterus via interposed ANs (**Fig. 3i**). Together, these cells form an extended
361 feedback loop linking uterus sensory signals with uterus motor neurons.
362

363 We found two superclusters with particularly strong sensory associations: one is dominated by tactile influence,
364 and the other by proprioceptive influence (**Fig. 3d**). These cells may be involved in whole-body integration of
365 tactile or proprioceptive cues. For example, DNge104 is a cell in the tactile supercluster that is downstream

366 from tactile afferents across the body (**Fig. 3j**), but also upstream from tactile sensors from those same body
367 parts. Because DNge104 is inhibitory, this circuit could produce tactile contrast enhancement. For example,
368 touching the head or thorax is predicted to excite a specific AN which then increases DNge104 activity, thereby
369 suppressing tactile input to the rest of the body. It is interesting that some DNs and ANs are positioned to
370 primarily influence sensory signals, as targeting a sensory signal can be a powerful way to control a behavior:
371 many sensory neurons will carry a feedback signal to one or more loops, and modulating a feedback signal can
372 cause that loop, in essence, to operate with a different setpoint^{53,134,135}.
373

374 Even in the behavior-centric superclusters, we can find cells positioned to influence sensory processing. For
375 example, AN09B011 in the walking-steering supercluster (**Fig. 3k**) makes a strong direct connection onto a
376 visual centrifugal neuron (mALC5), which is positioned to suppress neurons with ventral visual fields, including
377 visual optic flow detectors (LPLC1¹³⁶, Nod3¹³⁷) and loom detectors (LPLC2¹³⁸). This AN is directly postsynaptic
378 to many types of leg proprioceptors, and so it might function to relay leg movement information to mALC5,
379 allowing this circuit to suppress visual responses to leg movement¹³⁹.
380

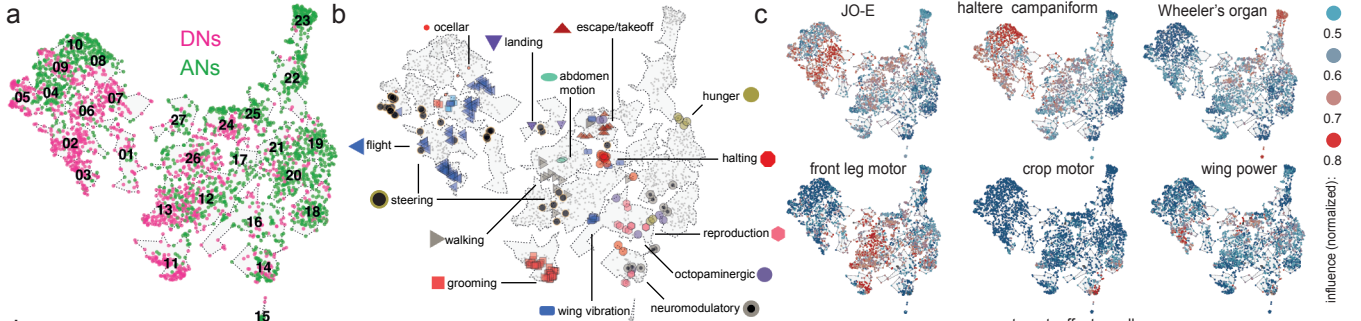
381 In summary, while some AN/DN superclusters seem to specialize in tactile or proprioceptive sensing, most can
382 be associated with a specific behavioral task. This is conceptually analogous to behavior-centric control
383 modules in robotic design^{12,13}. Behavior-centric control modules can be useful because they reduce the need
384 for centralized planning and coordination.

385 Specialization and coordination among DNs and ANs

386 Thus far, we have seen that DNs and ANs can be divided into superclusters. Importantly, the cells in these
387 superclusters are not redundant: their inputs and outputs are specialized. As an illustrative example, consider
388 the head-and-eye-orienting supercluster. Different ANs and DNs in this supercluster are influenced by distinct
389 visual or mechanosensory signals, and they influence different combinations of neck and eye motor neurons
390 (**Fig. 4a-c**).
391

392 Within a supercluster, cells having different specializations are often linked via direct and/or indirect
393 connections. In some cases, particular DNs or ANs are positioned to recruit (or suppress) many other cells in
394 their home supercluster⁹⁵. Again, the head-and-eye-orienting supercluster provides examples of this. For
395 instance, DNA06 is an excitatory DN with connections onto eye motor neurons as well as neck motor neurons
396 that control all three axes of movement (roll, pitch, yaw; **Fig. 4d**). DNA06 also targets two ANs that are
397 positioned to excite neck and/or eye motor neurons. Meanwhile, DNA06 targets DNg89, which is positioned to
398 inhibit neck-pitch neurons⁵³, directly and indirectly through an AN that targets neck-pitch and neck-roll neurons
399 (**Fig. 4d**). In short, each DN and AN in this circuit is specialized to influence a specific combination of neck and
400 eye motor neurons, and their interactions might serve to coordinate head and eye movements in different
401 directions.
402

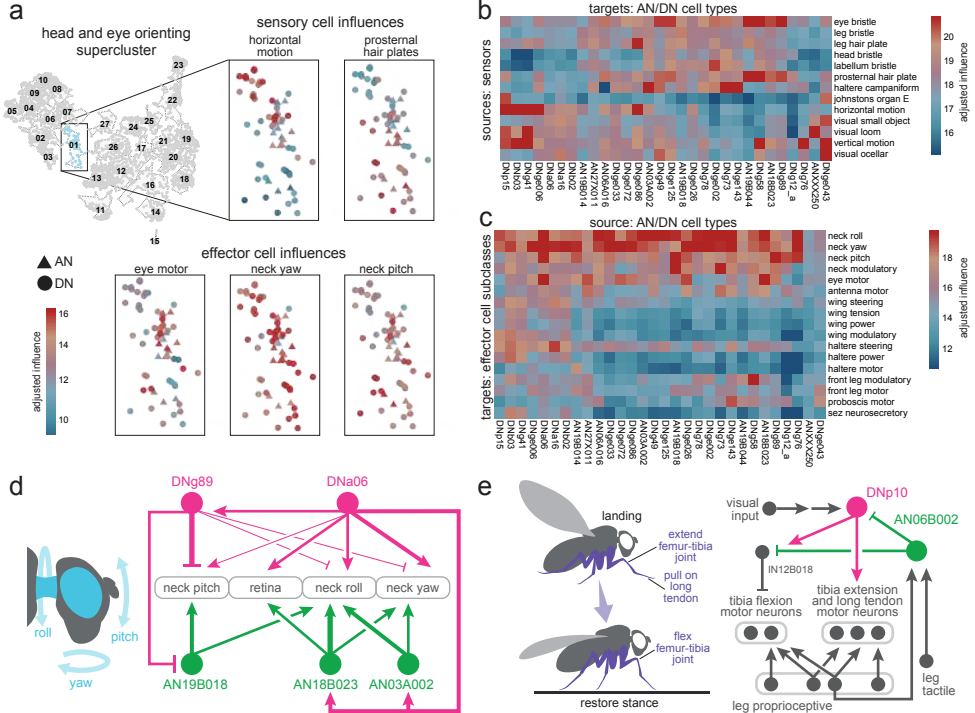
403 Within a supercluster, specialized ANs and DNs can also be organized into feedback loops. An example of this
404 from the landing supercluster involves DNp10 and AN06B002. DNp10 drives landing maneuvers in response to
405 looming visual stimuli¹⁰⁰, and we found this cell is positioned to excite tibial extensor motor neurons and also to
406 inhibit tibial flexor motor neurons via an interposed VNC inhibitory interneuron (**Fig. 4e**), implying that it drives
407 tibia extension during landing. At the same time, we found that AN06B002 is positioned to inhibit DNp10,
408 thereby arresting tibia extension. AN06B002 is postsynaptic to proprioceptive and tactile sensory neurons from
409 the leg (**Fig. 4e**), and so this circuit motif could form a negative feedback loop that arrests tibia extension when
410 the leg has made contact with the surface during landing, allowing the leg to relax into its normal standing
411 posture as the landing maneuver terminates.
412



413 Figure 3: Clustering ANs and DNs into behavior-centric modules.

- 414** a. UMAP embedding of all ANs and DNs based on cosine similarity between their direct connectivity vectors (connections to any other
415 proofread neuron in BANC). Neuroglancer link to ANs [here](#) and DNs [here](#).
- 416** b. Previously characterized ANs and DNs highlighted in this map (**Supplementary Data 7**).
- 417** c. In each copy of this same map, each point is an AN or DN, color-coded by the adjusted influence that cell receives from example
418 sensory neurons (top) or color-coded by the adjusted influence that cell sends to example effector cells (bottom). Based on these
419 adjusted influence scores, we lumped the 27 clusters into 15 superclusters.
- 420** d. Mean adjusted influence onto each AN/DN supercluster from select groups of sensory neurons. Superclusters are rows; sensory
421 neurons are columns. A subset of visual project neurons were used to determine processed visual streams from the optic lobes
422 123,137,139–152, see methods.
- 423** e. Mean adjusted influence from each supercluster onto select groups of effectors. Superclusters are rows; effectors are columns.
- 424** f. The same map, here colored by supercluster membership. [Neuroglancer link](#). See (**Supplementary Data 4**).
- 425** g. Example circuit involving visceral control ANs and DNs. [Neuroglancer link](#), [Codex network](#).
- 426** h. Example circuit involving the flight power supercluster and visceral control supercluster. [Neuroglancer link](#), [Codex network](#).
- 427** i. Example circuit for coordinated visceral sensing and reproductive control. ANXXX986 is female-specific^{8,21}. [Neuroglancer link](#).
- 428** j. Example circuit involving a DN in the tactile supercluster. [Neuroglancer link](#), [Codex network](#).
- 429** k. Example circuit illustrating proprioceptive input to visual neurons. [Neuroglancer link](#), [Codex network](#).

430
431
432



433 **Figure 4: Specializations and coordination within a functional supercluster.**

- 434 a. Enlarged view of the head-and-eye orienting supercluster, taken from the UMAP embedding of all DNs and ANs (**Fig. 3d**). Top: cells
435 are color-coded by their incoming adjusted influence from two different sensory sources. Same as (a), but now cells are color-coded
436 by their outgoing adjusted influence onto three different effector cell groups. [Neuroglancer link](#), [Codex search](#).
437 b. Mean adjusted influence from sensor sources, for all cell types in the head-and-eye orienting supercluster.
438 c. Mean adjusted influence onto effector cells, for these same ANs and DNs.
439 d. An example circuit with five cell types in the head and eye orienting supercluster. Thick arrows indicate connections with >100
440 synapses; intermediate arrows indicate connections with 20-100 synapses; thin arrows indicate connections with 5-20 synapses. This
441 example was chosen to illustrate the concept of diverse but overlapping patterns of connectivity within a supercluster, as well as
442 hierarchical interactions between cells in the same supercluster. [Neuroglancer link](#), [Codex network](#).
443 e. An example circuit with two cell types in the landing supercluster (DNp10¹⁰⁰, AN06B002). This example was chosen to illustrate the
444 concept that ANs and DNs in the same supercluster can be organized into loops. [Neuroglancer link](#), [Codex network](#).
445
446

447 In summary, we find that cells in the same supercluster can have specialized connections to sensors and
448 effectors. For each general behavioral task, there is a set of DNs and ANs that link sensors and effectors in
449 diverse, overlapping combinations. Often, these related cells are interconnected, sometimes in loops. These
450 circuits of finely specialized cells should allow for flexible behavioral control which can be rapidly fine-tuned to
451 the current state of the body and the environment.

452 Interactions between behavior-centric modules

453 In a system with behavior-centric modules, there should be ways for one module to influence another. In
454 robotic design, this can help prioritize behaviors, resolve conflicts among behavioral drives, and link related
455 behaviors in sequences^{12,13}. Indeed, the BANC dataset reveals a specific pattern of influence among AN/DN
456 superclusters (**Fig. 5a**). Focusing on the strongest of these influences, we can begin to reconstruct
457 relationships between AN/DN behavioral modules (**Fig. 5b**).

458

459 For example, the threat response supercluster strongly influences the walking supercluster (**Fig. 5a,b**),
460 consistent with the idea that threat responses generally require interruption of ongoing walking. Similarly, flight
461 steering and walking steering strongly influence head-and-eye-orienting (**Fig. 5a,b**), reflecting the close
462 coupling between head orientation and steering during flight and walking^{153,154}. Finally, walking steering
463 influences probing, a behavior that involves pivoting maneuvers where the fly dances around a food source¹⁵⁵,
464 this interaction might help coordinate proboscis movements with leg movements.

465

466 To better understand the circuits that mediate interactions between superclusters, it is useful to drill down to
467 some specific examples. Consider the circuit (**Fig. 5c**) that involves cells from the proprioceptive supercluster
468 (AN09B029_b), the threat response supercluster (DNp38), and the walking supercluster (DNg100 and
469 AN02A002). Here, AN09B029_b sends ascending mechanosensory signals to DNp38, which also receives
470 antennal mechanosensory signals (via WPNs¹⁵⁶). DNp38 is positioned to drive co-contraction of antagonistic
471 muscle pairs in all the legs, which would likely increase leg stiffness. Thus, this circuit motif might function to
472 integrate whole-body mechanosensory signals to trigger defensive posture stabilization. Meanwhile, DNp38 is
473 also positioned to recruit AN02A002, which inhibits DNg100, a cell in the walking supercluster downstream
474 from pro-walking Bolt neurons⁹⁹. In this manner, a mechanical threat could stabilize the resting stance while
475 also suppressing walking drive.

476

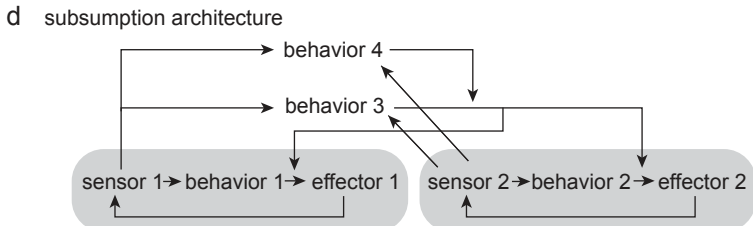
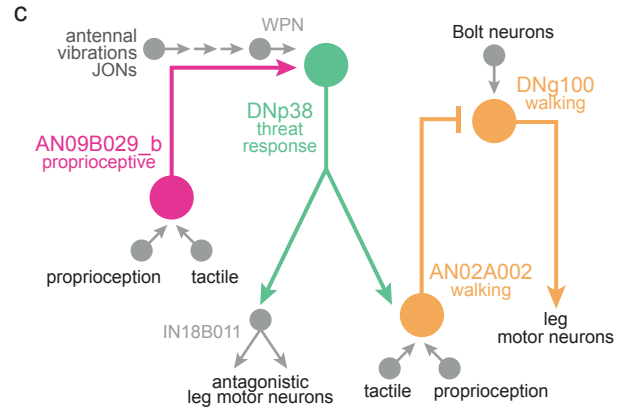
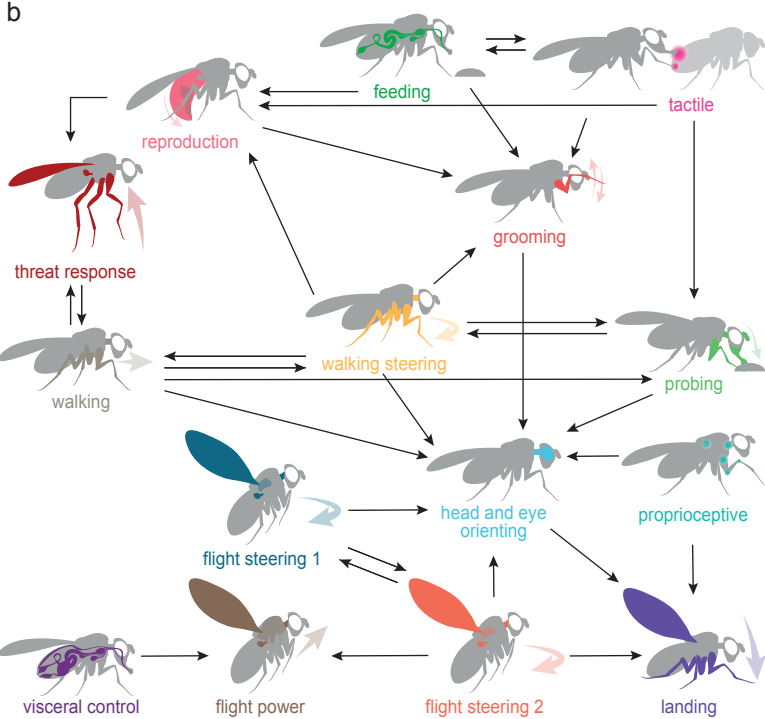
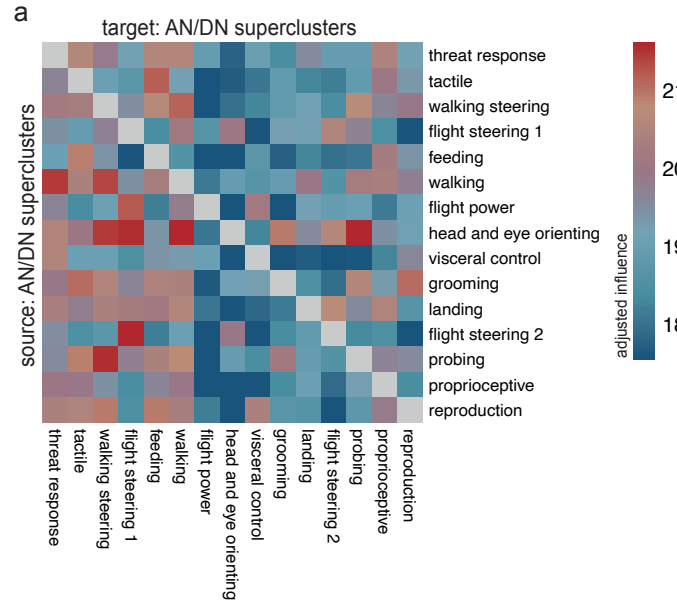
477 Overall, the arrangement of influences between superclusters (**Fig. 5b**) is conceptually analogous to
478 subsumption architecture in robots (**Fig. 5d**). In such architecture, some behavior-centric modules are
479 positioned to influence, or “subsume”, another module, in order to exploit its functionality or override it^{12,13}. A set
480 of semi-autonomous modules, loosely linked in a subsumption hierarchy, can produce complex, emergent
481 behaviors¹³. This architecture can also potentially account for some hierarchical relationships among animal
482 behaviors^{157,158}.

483 Linking behavior-centric modules with other divisions of the nervous system

484 Finally, we asked how DNs and ANs are integrated with the rest of the CNS. We began by dividing the CNS
485 into 13 discrete networks, based on each neuron’s direct synaptic connections, using a spectral clustering
486 algorithm that seeks to maximize within-network connectivity while minimizing across-network connectivity
487 (**Fig. 6a, Extended Data Fig. 5a**). Our aim was to find large groups of interconnected neurons, as these would
488 be candidate coarse functional divisions of the CNS.

489

490



491 Figure 5: Interactions between behavior-centric modules

492 a. Mean adjusted influence of each AN/DN supercluster on every other supercluster. Values are normalized by the number of cells in
493 each supercluster.

494 b. Summary of the strongest adjusted influences between superclusters.

495 c. A circuit illustrating an example of cross-cluster interactions between DNs and ANs. This circuit links cells in the proprioceptive,
496 threat-response, and walking superclusters. [Neuroglancer link](#), [Codex network](#).

497 d. Schematic example of subsumption architecture. This example has two local loops (behavior 1 and behavior 2), corresponding e.g.
498 the control of individual legs. Behavior 3 is positioned to take control of both local loops (subsumption), contingent on some input from
499 both sensors. Behavior 4 is positioned to subsume all other behaviors, based on some other input from both sensors.

500

501

502 Notably, many of these CNS networks contain ANs and DNs (**Fig. 6a**, **Extended Data Fig. 5b**). Most CNS
503 networks also have a high influence on effector cells (**Fig. 6b**, **Extended Data Fig. 5a-f**). Together, these
504 results suggest that behavioral control is highly distributed across CNS networks. The CNS networks with a
505 high influence on effectors are directly linked in a nearly all-to-all pattern of reciprocal connectivity (**Fig. 6c,d**,
506 **Extended Data Fig. 5f**). Interestingly, these links are disproportionately composed of DNs: when we counted
507 each neuron's synaptic partners outside its assigned network, we found DNs had a relatively high proportion of
508 outside partners (**Fig. 6e**). We found the same trend for ANs, although this trend was weaker. Most AN/DN
509 superclusters are divided between two or three CNS networks (**Fig. 6f**), consistent with the notion that ANs and
510 DNs often form bridges between networks. Together, these results argue that ANs and (particularly) DNs have
511 a key role in bridging different functional divisions of the CNS.

512

513 Interestingly, the central complex and the olfactory system emerged as networks with distinctive properties.
514 These networks have relatively low influence on effectors (**Fig. 6b**), weak input from other networks (**Fig. 6c,d**),
515 and low AN/DN membership (**Extended Data Fig. 5b**). These networks are likely to have a relatively indirect
516 role in behavioral control: they may merely “supervise” actions, rather than directly controlling actions.

517

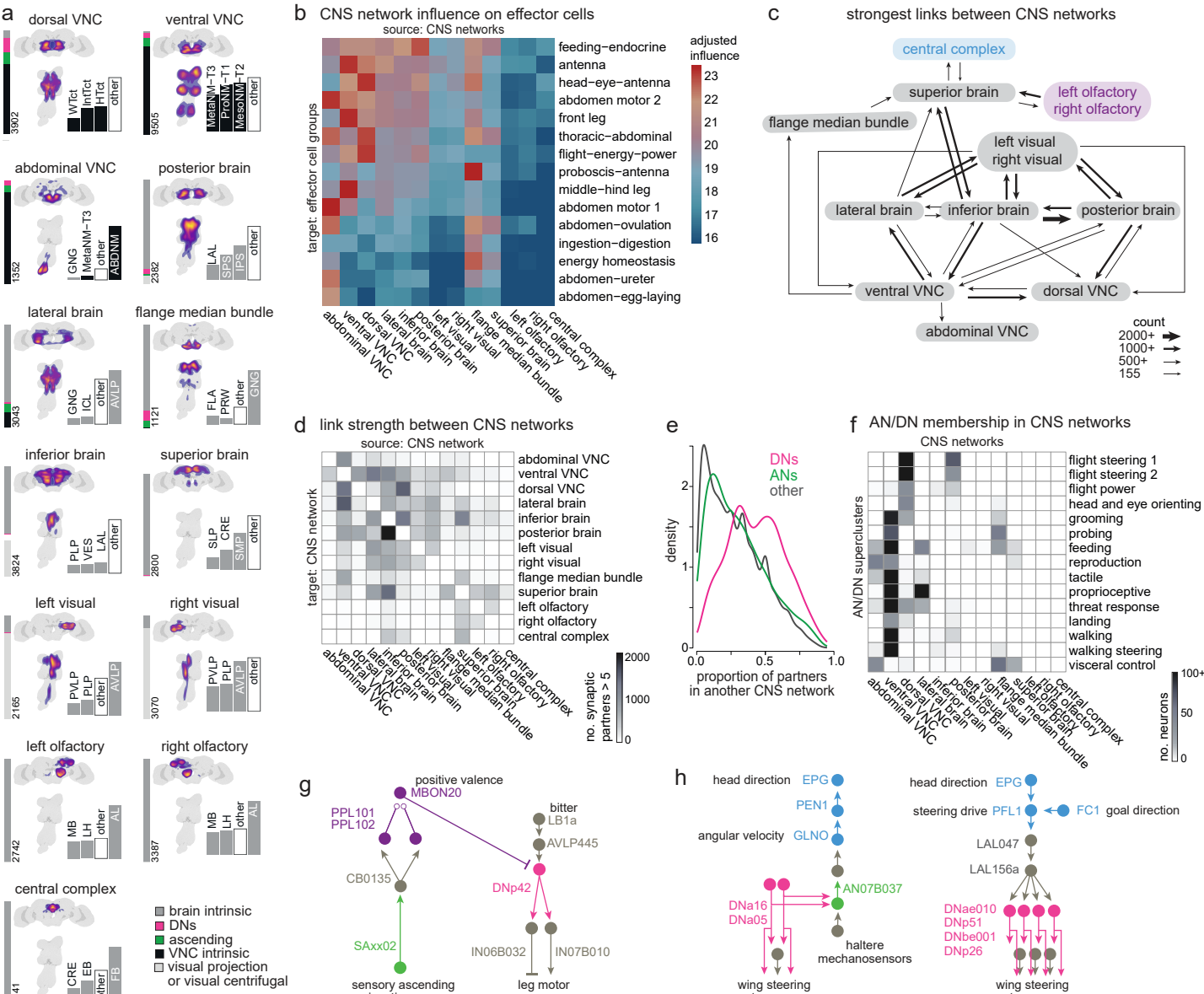
518 Several example circuits illustrate how these supervisory networks might communicate with lower networks via
519 DNs and ANs (**Fig. 6g-h**, **Extended Data Fig. 5c-d**). For example, the BANC dataset shows that putative
520 nociceptive cells in the legs (SNaxx02) project directly to the brain, where they are positioned to excite several
521 mushroom body dopamine neurons, including PPL101 and PPL102 (**Fig. 6g**). These dopamine neurons
522 encode negative valence^{5,159,160}, and they are positioned to instruct olfactory learning in several mushroom body
523 output neurons, including MBON20⁵. Given the synaptic learning rules governing olfactory learning in the
524 mushroom body, we would expect that these dopamine neurons will “teach” MBON20 to respond selectively to
525 odors lacking negative associations -- i.e., odors associated with safety. Notably, MBON20 is positioned to
526 inhibit DNp42, which drives backward walking in response to noxious stimuli¹⁰³. Thus, odors associated with
527 safety should excite MBON20, which is then positioned to suppress avoidance behavior (**Fig. 6g**). This
528 example circuit illustrates how the olfactory network can supervise behavior by interacting with ANs and DNs.

529

530 Another example circuit comes from the central complex, the brain’s navigation center. In the central complex,
531 angular path integration is driven by an internal estimate of the fly’s rotational velocity, encoded by GLNO
532 neurons¹⁶¹. The BANC dataset reveals that GLNO neurons receive a strong disynaptic excitatory input from a
533 specific AN (**Fig. 6h**). This AN receives direct input from DNA16 and DNA05, which likely contribute to steering
534 in flight, via direct and indirect connections onto wing steering motor neurons. Thus, this AN is positioned to
535 send copies of descending flight steering signals back up to the central complex, to update the head direction
536 system in anticipation of an upcoming change in heading. The central complex continuously compares the fly’s
537 estimated head direction against its internal goal direction. This comparison is performed by several cell types,
538 including PFL1^{6,162,163}, but the DN targets of PFL1 have not been fully identifiable until now, as DNs were
539 fragmentary in available connectomes. The BANC dataset shows that DNs downstream from PFL1 are in fact
540 putative flight steering neurons (**Fig. 6h**). Thus, PFL1 is positioned to compare head direction with its goal
541 direction and to generate corrective steering commands in flight when these directions are misaligned. Again,
542 this example illustrates how the central complex can supervise behavior by interacting with ANs and DNs.

543

544



545 **Figure 6: Linking CNS networks with superclusters of ANs and DNs.**

546 a. CNS networks, obtained via spectral clustering of 51,502 backbone proofread neurons in the BANC dataset (excluding peripheral
547 neurons and optic lobe neurons but including visual projection neurons and visual centrifugal neurons). Each panel includes a 2D
548 kernel density estimation, a bar plot indicating the network composition, and cell count. Two pairs of networks are mirror images of
549 each other (olfaction right/left and visual right/left), while all other networks are bilaterally symmetric, indicating high bilateral
550 integration in those networks. Anatomical density images are normalized separately for the brain and VNC, based on a random
551 sample of 100k synapses from each CNS network, the hotter the color the denser the synapses.

552 b. Mean adjusted influence of each CNS network on each effector cell group (**Fig. 2i**).

553 c. Strongest links between CNS networks. The size of each arrow represents the number of postsynaptic cells in that link. One weaker
554 link is shown (155 cells), because this is the strongest output link of the central complex.

555 d. Link strength between CNS networks, measured as the number of postsynaptic cells in that link. The color scale is capped at 2000
556 cells.

557 e. Out-of-network connections, measured as the proportion of partners each cell has in another CNS network. DNs and ANs have an
558 unusually high proportion of out-of-network connections. The area under each curve is normalized to 1. All three distributions are
559 significantly different from each other (DN vs. other $p = 1.92 \times 10^{-97}$, AN vs. other $p = 6.03 \times 10^{-5}$, AN vs. DN $p = 6.74 \times 10^{-43}$; 2-sample
560 Kolmogorov-Smirnov tests).

561 f. Number of ANs and DNs in each CNS network. ANs and DNs are grouped by supercluster (**Fig. 3f**).

562 g. Example circuit connecting mushroom body neurons (purple) to ANs and DNs. [Neuroglancer link](#), [Codex network](#).

563 h. Example circuit connecting central complex neurons (blue) to ANs and DNs. Neuroglancer links [here](#) and [here](#). [Codex network](#).

564

565

566 Discussion

567 The BANC dataset is the first connectome to span the full CNS of a limbed animal. Previous work^{7,9–11,14–16} has
568 used connectome data to analyze the adult fly CNS, but the neurons connecting the brain and VNC were
569 fragmentary in all these datasets²¹, and this limited our ability to connect neurons with behavior. The BANC
570 dataset unifies the brain and VNC for the first time.

571

572 The BANC represents a major advance in scale and complexity, compared to other complete connectomes (*C.*
573 *elegans*^{1,2}, *Ciona intestinalis*⁴, and *Platynereis dumerilii*³). Tackling a problem of this scale required us to
574 leverage new methods for semi-automated sectioning and EM imaging, computational section alignment, cell
575 segmentation, synapse identification, neurotransmitter assignment, and cell type matching. Because we could
576 draw on the expertise of a large community, we were also able to assemble an embodied connectome with
577 explicit connections to many organ systems.

578

579 An embodied connectome of this scale offers new clues about the control architecture of the CNS. In principle,
580 behavioral control could work in a top-down manner, where actions are selected centrally and then relayed to
581 lower regions for implementation, and this has been suggested even for insects²⁷. Recently, however, there is
582 new interest in the notion that behavioral control is not centralized, but distributed, in both insects and in
583 vertebrates^{29,91,164,165}. Our findings support this latter view. Specifically, our results argue that the core elements
584 of behavioral control are a set of local feedback loops, where effectors are primarily influenced by local
585 sensors. These local loops may be analogous to short feedback loops in the vertebrate spinal cord and
586 brainstem^{166,167}. In general terms, local loops are useful because they simplify control and minimize delays. At
587 the same time, purposeful behavior also requires long-range coordination among body parts, and this is
588 mediated, in part, by DNs and ANs. The BANC dataset allowed us to systematically analyze *Drosophila* DNs
589 and ANs for the first time. We found these cells could be divided into superclusters, with each supercluster
590 linking a specific set of sensory cells and effector cells. Moreover, we found that DNs and ANs organize effector
591 cells into discrete clusters of co-regulated motor/endocrine units. We were able to link many AN/DN
592 superclusters with putative behavioral functions, reminiscent of behavior-centric control modules in robotic
593 architecture¹³.

594

595 The gap between the brain and the VNC is often called a bottleneck of information transfer within the CNS^{19,21},
596 but in fact, the sheer number of DNs (~1300 cells) and ANs (~2400 cells) is much larger than the number of
597 effector cells in the BANC dataset (~1000). If we think of DNs and ANs as “wires” for actuating effector cells in
598 different combinations, then the large number of DNs and ANs suggests that effector cells can be actuated in
599 many different combinations. Indeed, within each AN/DN supercluster, we find many fine-grained variations on
600 the same connection pattern, forming parallel pathways with slightly different inputs and/or outputs. This
601 arrangement should promote flexibility, by offering many available action patterns. It should also promote
602 precision, by pre-selecting the specialized action patterns that can result from particular patterns of sensory
603 input. These sorts of connectivity specializations could explain why, for example, different threat response DNs
604 can produce different escape takeoff maneuvers¹⁶⁸, and why different walking-steering DNs can produce
605 distinct changes in leg movement¹⁰⁵.

606

607 Finally, when we analyzed the network structure of the entire CNS, we found that the links between different
608 networks are enriched for ANs and (particularly) DNs. Importantly, we found that many CNS networks have a
609 high influence on effectors, supporting the idea that behavioral control is distributed, rather than centralized.
610 We found that a few CNS networks -- particularly the central complex and the olfactory system -- have a
611 relatively low influence on effectors, suggesting these networks have a supervisory role, rather than a direct
612 role in behavioral control. This type of supervision is characteristic of subsumption architecture in robotic
613 design, where high-level modules have the ability to recruit or suppress lower-level modules, but these
614 high-level modules are not actually required for any but the most complex behaviors^{12,13}. In the future, it will be
615 interesting to investigate why supervisory networks like the central complex can have such profound behavioral
616 effects^{169,170}, given their weak anatomical connection to effector cells.

617

618 This project illustrates how insight can arise from new technologies, combined with the accumulation of many
619 small biological facts. Just as early cartographers amalgamated the work of other map-makers, we have

620 deliberately amalgamated typology and metadata from prior *Drosophila* connectomes. The workflow we
621 developed is conceptually similar to the workflow that amalgamates information from emerging genomes. The
622 BANC is a living public dataset which should progressively improve as long as users continue to interact with it.
623 This open science effort should generate even more testable experimental hypotheses and, ultimately, new
624 theories.

625 Acknowledgements

626 We thank Aaron Kuan for discussions, advice and assistance with specimen preparation and the imaging
627 pipeline; Philipp Schlegel and Casey Schnieder-Mizell for advice and assistance with computational
628 infrastructure and maintaining open source connectomics tools; members of SixEleven (Jenny Esteban Abelo,
629 Rimalyn Enopli Silay, Anthony Ralph Piccio, Renzo D. Requintina, Micah Colinares Molinas, Shaina Rose
630 Araneta, Jazel R. Digamon, Carine E. Estrella, Marlon Kedet Roda, Michael Manayaga Mates, David Benjamin
631 D. Conquilla, Romilyn Bardonido, Alvin Josh Mandahay, Rey Mark Asares, Brion Glee Baliña Gloria, Aleanne
632 May Hopkins, Jessa Calambro, Christine Joy Maquilan Tac-an, Cj Christine Cordova Tan, Cj Pilapil, Lea Lovely
633 Joy Jimenez Pelingon, Mary Rose Golez, Prince Lloyd Sy Cagampang, Jacqilyn Laude, Ehreca Mae Jongco
634 Pojio, Jayanne Biodes Mayormita, Mike Quibo Tambuco, Madiemie Inguito, Cedrick Earl Bernasol, Roden Rey
635 Nuiz Dizon, Francis Rainer Lindo, Noroddin Balambag, Cathy Pilapil, Tutor, Larben Milagrosa, Clyde Albero,
636 Cesar Jun M. Subtenente, Elison Rovic Monte, Sherwin Salem, Estephani A. Lim, Enriq Gerald Pacaldo,
637 Julianne Maquiling Bulaclac, Yna Bustria Jallorina, Catherine Gasi Colminas, Michael Carlo M. Pabroquez,
638 Jonalyn S. Revilleza, Nina Mae Dulaca, marchan manaytay, Rommel Roa, Glenda Malda Dawa, Baby Jane
639 Getizo, April Grace Delantes Alagaban, Krystel Joy Domingo, Mark Lester Avila, Nelsie Panes, Dwight
640 Jumaag, Hugh Ven Kyle Tecson, Jansen Seguido, James Nicle Cano, John David Asis, Althea Lou Alojipan
641 Aligria, Philip Ampo, Mary Grace Ybanez, Charmelyn Urboda, Vanessa C. Dal, Rhosly Jay Bumaya, Regine
642 Salem, Jan Marinie Ferraren, Mark Lester Caño, Joseph Enoc Roilo, Aljon Lastimoso, Romelita Maignos,
643 Kendrick Joules Vinson, Hella Jones Dulay, Celso Gonzales, Raffy Acosta, Irish Quijada Bonso, Johnclyde
644 Saguimpa, Wilbur Hernando De la Torre, Mark Lloyd Pielago, Clerk Derecho, Jaypee Balco, Remer
645 Tancontian, Allien Mae Gogo, Joshua Bañez, Nashra Hadjerol, Leslie Labaya Bongcales, Chereb Martinez,
646 Ianloyd B. Polinar, Jeanity Dominguez, Charlotte B. Solana, Queendolyn Pama, John Niño M. Ugdang, Melcris
647 Damasco, Marianne Marie Villarba, Edrian R. Navaja, Janice Salocot, Daril Bautista, James Andrew A.
648 Campos, Elanur Jimlani Acmad, Jet Dolorosa, Zairene Lenizo, Rey Adrian Candilada, Logic Domme Sauro
649 Ybañez, Mark Clint Encallado and Jovie Cano) for proofreading; May Husseini for project administration; Celia
650 David for creating training materials and helping to manage citizen scientists; the management at SixEleven for
651 coordination and professional proofreader management; Alexander Malakov for assistance with software
652 development; Stephen Holtz for discussions on chordotonal organs; Pablo Reimers for ground truth related to
653 LPSp neurotransmission; Noah Pettit for insights on PFL1 neurons; Lydia Hamburg for discussions on
654 connectome analysis; Anton Miroshnikow for discussions on Hugin neurons; Rosalinda Maggio for
655 unpublished insights into neurohormone expression in VNC neurons; Lisa Marin for discussions on MANC
656 annotations; Yijie Yin and Volker Hartenstein for discussions on hemilineages; Richard Schalek for help with
657 X-ray microCT scanning and processing; David Masao Zimmerman for advice and discussions on analysis;
658 and Lee and Wilson lab members for feedback on the manuscript. This work was supported by NIH grants
659 R01NS121874 (to B.d.B and W.C.A.L), RF1MH117808 (to J.C.T., H.S.S., and W.C.A.L.), U19NS118246 (to
660 J.D.), U24NS126935 and RF1MH117815 (to M.M. and H.S.S.) to perform large-scale proofreading, annotation,
661 and dissemination of the BANC dataset. Our work has benefited from the O2 High-Performance Compute
662 Cluster, supported by the Research Computing Group, at Harvard Medical School
663 (<https://it.hms.harvard.edu/our-services/research-computing>). A.S.B. was supported by a Sir Henry Wellcome
664 Postdoctoral Fellowship (222782/Z/21/Z); H.H.Y by a NIH K99 award (K99NS129759); B.d.B. by a Smith
665 Family Odyssey Award; R.M. and B.d.B. by a Harvard/MIT Joint Research Grant; D.A.P by a HHMI Awardee of
666 the Life Sciences Research Foundation Postdoctoral Fellowship (PJ100000343); S.A. by the NIH
667 (R00NS117657); J.C.T by the NIH (R01NS102333 and RF1NS128785) and a New York Stem Cell Foundation
668 Robertson Neuroscience Investigator Award; M.P.S. by the NIH (R01NS140174); M.Z. by the Deutsche
669 Forschungsgemeinschaft (ZA1296/1-1) and NV INBRE (GM103440); K.D. by the NSF (2127379); G.S. by the
670 JSPS (KAKENHI 25K00370) and JST (ASPIRE JPMJAP2302 and CRONOS JPMJCS24K2); M.J.P. by the
671 Deutsche Forschungsgemeinschaft (EXC2151-390873048, PA787/7-3, and PA787/9-3); F.C. by the NIH

672 (UM1NS132253, U24NS139927, RF1MH128840); J.M.J by a HHMI Gilliam Fellowship (GT15790); L.M.F and
673 T.F. by the Max Planck Society; S.D. by the Shanahan Family Foundation; M.A.M.O. by a Kempner Graduate
674 Fellowship; A.M.S. and S.H by the NIH (R01NS121911); G.S.X.E.J. by the NSF (2014862) and MRC
675 (MC_EX_MR/T046279/1); Z.A. by the Alice and Joseph Brooks Fund; and S.R. by the NIH (T32GM144273).
676 We thank Bradley Dickerson for his support of S.D. and E.B (NIH grant U01NS131438, NSF grant
677 IOS2221458, Searle Scholar and McKnight Scholar Awards). R.I.W. is an HHMI Investigator.

678 The BANC-FlyWire Consortium

679 Includes the listed authors of this paper and additionally: Anna Verbe¹, Gabriel A. Nieves-Sanabria², Devon
680 Jones³, Zijin Huang¹, Sofia Pinto⁴, Celia David³, Omaris Y. De Pablo-Crespo², Emily Ye⁵, Wolf Huetteroth⁶,
681 Zequan Liu⁷, Fernando J. Figueroa Santiago²

682

683 ¹Princeton Neuroscience Institute, Princeton University, Princeton, NJ, USA

684 ²Institute of Neurobiology, University of Puerto Rico Medical Sciences Campus, San Juan, Puerto Rico

685 ³Eyewire, Boston, MA, USA

686 ⁴Champalimaud Neuroscience Programme, Champalimaud Centre for the Unknown, Lisbon, Portugal

687 ⁵Department of Neurobiology, Harvard Medical School, Boston, MA, USA

688 ⁶Department of Biology, Leipzig University, Leipzig, Germany

689 ⁷RWTH Aachen University, Aachen, Germany

690 Author Contributions

691 R.M. and B.D.B. selected and behaviorally characterized the sample fly. M.K. generated synapse ground-truth.
692 J.S.P and M.K. prepared the sample and collected and aligned the EM dataset. S.P., N.K., D.I., K.L., R.L., A.H.,
693 A.B. and T.M. at Zetta.ai ran automatic cell, nuclei and mitochondrial segmentation on the dataset. M.K. and
694 R.J.V.R. evaluated the automatic segmentation and synapse prediction. K.M.D., D-Y.A., A.S.B and J.F. collated
695 neurotransmitter ground-truth and developed a fast-acting neurotransmitter prediction for BANC. E.P., S.D. F.C.
696 and A.H. lead data management through CAVE and Neuroglancer. M.M. and H.S.S. managed the FlyWire
697 team and led the proofreading and dissemination efforts. C.S., S.-C.Y. and B.S. oversaw proofreading efforts
698 through SixEleven. Specialist proofreading was conducted by L.S.C., R.J.V.R., H.L., E.M., N.G., B.M.L., A.C.,
699 J.G., B.S., A.B., J.H., K.W. and R.W., managed by H.H.Y. FlyWire citizen scientist members K.K. and N.S.
700 contributed proofreading and annotations. A.R.S., and M.S. managed the FlyWire community and onboarded
701 new members. J.S.P., H.H.Y. and A.S.B designed and implemented the annotation meta data scheme for
702 neuronal cell types in BANC. J.S.P. bridged the dataset to template spaces. M.K., H.H.Y. and R.J.V.R. identified
703 and seeded neuronal profiles of the neck and nerves. Key neuron annotations were contibuted by H.H.Y.,
704 A.S.B., J.S.P., M.K., C.S., S.D., T.S., F.K., P.B., E.L., S.E.P-L, J.J., S.P., S-Y.L., A.C., B.J., G.S., A.M., D.D,
705 M.J.P., K.E., S.H., S.A., T.M., M.Z., Jx.F., D.A.P., J.P., J.T., A.A., J.G., B.S., A.B., J.H., K.W., R.I.W and the
706 BANC-FlyWire Consortium, particularly a large number of motor neurons by A.A. S.E.P-L., Y.L., A.A., J.J., S.A.,
707 A.C., M.J.P., D.D., M.Z. and J.T. shared unpublished experimental observations that benefitted this work. The
708 influence metric was designed by Z.A., J.D., A.S.B. and R.I.W. Jx.F. implemented the cascade method for
709 validating the influence metric. J.S.P., E.P., A.M., G.S.X.E.J., K.K., Z.A., Jx.F., H.H.Y., and A.S.B. built
710 programmatic tools for data access and analysis. A.M. disseminated data and analysis results through FlyWire
711 Codex. Data analysis was conducted by A.S.B, M.O. and R.I.W. Circuit vignettes were built by A.S.B, S.R.,
712 M.F.C., Jx.F., D.A.P., Y.Z., W.Z, H.H.Y. and R.I.W. A.S.B., W.C.A.L. and R.I.W. wrote the manuscript with
713 feedback from the authors. A.S.B, H.H.Y., J.S.P., M.M., R.I.W. and W.C.A.L. managed the project. M.F.C. and
714 A.R.S. produced graphics and illustrations, H.L. and L.S.C. copy edited the manuscript. Correspondence on
715 cell typing, data and data analysis can go to A.S.B. and J.S.P. Correspondence on FlyWire and proofreading
716 can go to M.M. Correspondence on influence scores can go to J.D. Correspondence on science and data
717 collection can go to R.I.W. and W.C.A.L.

718 Competing Interests

719 Harvard University filed a patent application regarding GridTape (WO2017184621A1) on behalf of the
720 inventors, including W.C.A.L. and negotiated licensing agreements with interested partners. T.M., S.P., N.K.,

721 D.I., K.L., R.L., A.H., J.A.B., and H.S.S. declare financial interest in Zetta AI. L.S.C., R.J.V.R., H.L., E.M., N.G.,
722 B.M.L. declare financial interest in Aelysia LTD. E.P. is a principal of Yikes LLC.

723 Methods

724 Specimen

725 The Brain and Nerve Cord (BANC) sample came from a female adult fly. We behaviorally screened 5-6 day
726 post-eclosion wild-type *Drosophila melanogaster* (F1 progeny of a w¹¹¹⁸ × Canton-S cross) female flies^{171,172}.
727 The fly used for the BANC dataset turned right 70% of the time over 582 choices when walking in an acrylic
728 Y-maze for 2 hours. We raised the flies on standard cornmeal-dextrose medium at room temperature (~20 °C)
729 in natural lighting conditions. We collected flies on the day after eclosion, housed them in vials with other flies
730 for 4-5 days, behaviorally tested them and then subsequently housed them individually in vials for ~1 day at
731 25°C until dissection.

732

733 To dissect the flies, we pinned them individually onto a dissection pad then submerged them in a drop of ice
734 cold Karnovsky's fixative (2.5% formaldehyde, 2.5% glutaraldehyde in 0.1M cacodylate buffer, pH 7.4)
735 containing 0.04% CaCl₂. We removed the legs and proboscis removed to allow fixative to access the nervous
736 tissue. Next, we carefully removed the head capsule and the cuticle of the ventral thorax to expose the nervous
737 tissue for dissection. Within 5 minutes, we completely dissected the brain and connected VNC, and we
738 transferred it to an Eppendorf tube containing the same Karnovsky's fixative. We fixed the sample at 4 °C
739 overnight. On the subsequent day, we washed the sample with 0.02M 3-amino-1,2,4-triazole (A-TRA) in
740 cacodylate buffer (3x10min) and then we stained it with 1% OsO₄ in 0.1M A-TRA for 90 minutes on ice. On the
741 same day, we stained the sample with 1% thiocarbohydrazide for 8 minutes at 40 °C, 2% OsO₄ (aqueous) at
742 room temperature for 60 minutes, and 1% uranyl acetate in maleate buffer at 4 °C overnight. On the next day,
743 the sample was stained with lead aspartate for 3 hours at 60 °C, then dehydrated in a graded ethanol series,
744 washed with propylene oxide, and infiltrated with 2:1 and 1:2 propylene oxide:LX-112 resin consecutively for 30
745 minutes each. The sample was then placed in pure LX-112 resin overnight at 4 °C and was embedded in fresh
746 pure resin the following day and cured at 60 °C for 48 hours.

747

748 The resin-embedded sample was scanned on a microCT X-ray scanner (Zeiss) before serial sectioning to
749 screen for obvious defects or damage. Importantly, the neck connective appeared intact. The specimen
750 includes the central brain, neck connective, VNC and the medulla, lobula and lobula plate of the optic lobes. It
751 lacks the lamina (part of the optic lobes), the ocelli and the ocellar ganglion. Thus, the R1-6 photoreceptors and
752 the ocellar photoreceptors are missing from BANC (~10000 cells) and intrinsic neurons that arborize in the
753 lamina and ocellar ganglion are incomplete (cell types: L1-5, Lai, T1, C2, C3, Lat, Lawf1, Lawf2, OCG01,
754 OCG02, OCC01, OCC02, DNp28 and the ocellar local neurons). The BANC is the only available dataset for
755 which the complete female abdominal neuromere is available.

756 Serial sectioning

757 We cut serial 45-50 nm thin sections and collected them on a 7500-slot reel of GridTape (Luxel) as previously
758 described in⁷.

759 Transmission electron microscopy (TEM) imaging

760 We used one TEM (JEOL 1200 EX) with a custom vacuum extension and scintillator (Grant Scientific), 2 x 2
761 array of SCIMOS cameras (Andor, Zyla 4.2), and custom modified with a reel-to-reel, GridTape imaging stage to
762 acquire the dataset as described previously⁷. Imaging spanned 7.5 calendar months, but 96.5% of the images
763 were acquired during the 4 months of November 2021 to February 2022.

764 Missing data

765 Of the 7010 sections, 6970 (99.43%) were collected and imaged without data loss. Ten (0.14%) have no data
766 due to the section being lost (sections 856, 885, 3755, 5746, 5772, 5778, 5793, 5801, 5822 and 5869). Notably
767 none of the losses are consecutive serial sections. One of these losses (3755) was because the section was

768 collected onto the wrong location on the GridTape (not over the slot) and so it could not be imaged with TEM.
769 The other 9 losses were due to the support film rupturing after section collection but before the section could be
770 imaged. An additional 30 sections (0.43%) have partial data: 11 sections are missing all images for the brain:
771 914, 1462, 5841, 5849, 5888, 5896, 5916, 6207, 6208, 6209 and 6210; 7 sections are missing all images for
772 the VNC: 874, 2784, 2822, 3064, 3102, 4566 and 5840; 12 sections are missing a fraction of brain and/or VNC
773 images: 2828, 2860, 2912, 2986, 3054, 3080, 3586, 3605, 3833, 4648, 4768 and 5935. The large majority of
774 these losses were also caused by partial rupturing of the support film before the tissue was imaged.

775 TEM dataset alignment and segmentation

776 We performed initial BANC image alignment with a custom software pipeline that deployed AlignTK alignment
777 functions (<https://mmbios.pitt.edu/aligntk-home>) on a computing cluster⁷. We refined the alignment of the data
778 using self-supervised CNNs and online optimization to produce displacement fields that were combined with a
779 global relaxation^{173,174}. We next trained a CNN to identify regions that were damaged during serial sectioning.
780 We then used CNNs to segment the dataset into cells and fragments of cells at 16 x 16 x 45 nm³, excluding
781 regions that decreased cell segmentation performance including areas with damage, as well as organelles
782 including nuclei and mitochondria^{8,31}. We then ingested the automated segmentation into the Connectome
783 Annotation Versioning Engine (CAVE)³³ for distributed proofreading.

784 Synapse detection

785 We generated synapses in two-steps: (1) postsynaptic terminal detection and (2) synaptic partner
786 assignment¹⁷⁵. We pretrained both models with data from FAFB, and we tuned the detection model with
787 additional labels from the BANC. The detection operated on 8 x 8 x 45 nm³ images, with an output at 16 x 16 x
788 45 nm³. We removed detection objects <3 voxels. Assignment operated at 16 x 16 x 45 nm³. We merged
789 terminals with identical assignments that were within 200 nm of each other into a single terminal. This detection
790 is known as synapses_250226 and is available through CAVE. It comprises 218460852 synaptic links, of which
791 65% of presynaptic ends and 22% of postsynaptic ends are connected to a proofread neuron.

792 Synapse prediction evaluation

793 To determine the false-positive rate of the synapse detection, we randomly selected 1000 synapses from
794 across the dataset (~70 synapses per neuropil region and for all of the nerves combined, total: 4648) and
795 manually scored them as true synapses, ambiguous, or false positives (**Extended Data Fig. 1c**). We also
796 evaluated synapses on a 2 x 2 x 2 μm³ cutout from the mushroom body, a known problem area for our
797 detection method: F-score: .79, Precision: .68, Recall: .95. Because this detection relies on identifying
798 postsynaptic profiles, some classes of synaptic connection for which postsynaptic sites are less distinct may be
799 under-detected. We know that our average number of outgoing connections for Kenyon cells (139) is far
800 smaller than in FAFB (213, cleft score threshold > 50). Another area of under-detection may be axo-axonic
801 connections between sensory neurons. The BANC detection has an autapse rate of 2.1%, a majority of which
802 we expect to be a misassignment of the presynaptic link from a correctly detected postsynaptic link. We
803 recommend users filter out autapses in their analyses.

804 Neurotransmitter prediction

805 We used a recently described approach to predict neurotransmitter type at each automatically predicted
806 synapse⁴⁶. Briefly, we trained a 3D convolutional neural network (CNN) to classify presynapses into one of
807 eight neurotransmitter classes: acetylcholine, dopamine, GABA, glutamate, histamine, octopamine, serotonin,
808 or tyramine. We compiled ground truth data for synaptic transmission from the
809 literature^{6,9,60,61,63,64,67,70,118,120,121,130,133,137,140,176–255}, totaling 4545 identified cell types from FAFB/MANC/Hemibrain.
810 Of these, members of 2930 cell types (37878 neurons) could be found in BANC. We removed motor neurons
811 from the ground truth, as they have few presynapses within the CNS. The complete dataset was split by
812 neuron into training and testing sets, with 80% of the data for training and the remaining 20% for testing. This
813 resulted in 16448 neurons for training and 4124 for testing. We used the following sampling strategy to ensure
814 a balanced dataset across different neuron types. For neurons associated with the most common
815 neurotransmitters (acetylcholine, GABA and glutamate), we randomly sampled a maximum of 10 presynaptic

816 sites from each neuron. For all other neurotransmitters, we included all identified presynaptic sites. This
817 approach ensured that all cell types that had ground-truth were represented in both training and testing sets.
818 The input data for the network consisted of 3D cutouts from the EM volume, each centered on a presynaptic
819 site. These local cutouts had dimensions of 640 x 640 x 630 nm. We used a 3D CNN architecture based on the
820 18-layer residual network (ResNet-18)²⁵⁶. ResNet-18 includes 3D convolutional layers, batch normalization and
821 ReLU activation functions, with the core of the architecture consisting of residual blocks that use skip
822 connections to enable effective training. The model architecture was adapted for our task by modifying the
823 initial convolutional block to accept single-channel grayscale input from EM data. Finally, we replaced the
824 model's original fully-connected output layer with a linear layer that maps the learned features to our eight
825 specific neurotransmitter classes, followed by a softmax activation to produce the final probability distribution.
826 The network was trained using the Adam optimizer²⁵⁷ to minimize the focal loss function²⁵⁸. This loss function
827 is a variant of the standard cross-entropy loss, which is effective for datasets with a significant class imbalance
828 as it down-weights the loss assigned to well classified samples, allowing the model to focus on
829 difficult-to-classify samples. To further improve generalization of the model, we applied several data
830 augmentation techniques during training. These included random affine transformations, random noise, and
831 random gamma correction. The probability of applying these augmentations was increased for less frequent
832 neurotransmitter classes to further mitigate the class imbalance. We trained the model for 1,060,000 iterations
833 using a batch size of 16 samples. The final model selected was the one that achieved the highest classification
834 accuracy on the separate testing set. A neuron-level transmitter prediction is obtained by summing the class
835 classification probabilities for each predicted class across all presynaptic detections, and selecting the class
836 with the highest total confidence as the most likely neurotransmitter; we assume Dale's law²⁵⁹ holds even
837 though we know that an unknown proportion of neurons in the CNS co-transmit with multiple fast-acting
838 transmitters^{46,190,192,260}. Though marginally improved, as in⁴⁶, we expect a large proportion of our serotonin
839 predictions in particular to be incorrect, as the network seems to guess serotonin for peptidergic neurons that
840 lack clear signs for another classification. A fully cited compilation of ground truth labels per cell type can be
841 found here: https://github.com/funkelab/drosophila_neurotransmitters/tree/main, collated by A.S.B., D-Y.A. and
842 J.F.

843 Neuropils and template alignment

844 To transform the BANC data into a standard template space for analysis and inter-dataset comparisons, we
845 computationally generated a 'neuropil stain' based on the synapse prediction¹⁷⁵. To do this, we downsampled
846 and Gaussian blurred ($\sigma = \sim 900$ nm) the predicted synapse locations to produce a synapse density map at the
847 approximate resolution of light microscopy data used in the Drosophila standard templates. We then registered
848 the synapse density map of the EM dataset to the JRC 2018 Female brain and JRC 2018 Female VNC
849 templates²⁶¹ separately using elastix (<https://elastix.lumc.nl/>). Leveraging this alignment, neuropils and neurons
850 were transformed between different connectome datasets for visualization and quantitative comparison in the
851 same coordinate system. Meshes for individual neuropils in the central brain³⁵ and VNC³⁶ were based on
852 previous work. We generated a left-right registration for BANC based on a thinplate-spline warping registration
853 built from matched points on identified pairs of ~30 DNs, available through the bancr R package.

854 Proofreading

855 We proofread neurons to correct automated cell segmentation errors as we described previously¹⁵. Members of
856 our respective laboratories, dedicated proofreading teams at Princeton, SixEleven (Davao City, Philippines),
857 and Aelysia (Bristol, United Kingdom), as well as a community of citizen scientists collaboratively undertook
858 this effort. We used a multi-pronged strategy. To capture neurons with cell bodies in the CNS, we proofread
859 segments associated with automatically-detected nuclei, which were then extended to reconstruct their full
860 morphology and remove false mergers. To include sensory neurons, whose cell bodies typically reside outside
861 the CNS, we seeded every neuron profile in planes that cut a cross-section through a nerve (1 plane per nerve,
862 except in cases where 1 plane could not capture the full cross-section of the nerve; 47 seed planes total) and
863 then reconstructed starting from those seeds. To capture all neurons in the neck connective, we seeded two
864 planes that were cross-sections through the neck connective ($y = 92500$ and $y = 121000$). These transverse
865 planes were positioned posterior to the central brain and anterior to the VNC. Additionally, we proofread orphan
866 segments containing >100 presynaptic links in decreasing order of synapse count for the central brain and

867 VNC. We considered a neuron ‘backbone proofread’ when its primary neurites (if not sensory), or major
868 microtubule-rich processes had undergone a thorough review³². This indicated that we expected the overall
869 morphology of the cell to be correct and that, while minor branches or a small number of synapses might still
870 require adjustment, we did not anticipate future proofreading to radically alter the neuron’s core shape or
871 identity. We proofread 114,610 neurons to ‘backbone proofread’. In total, 155 people served as proofreaders for
872 the project (defined as people who made ≥100 edits).

873 Color MIPs

874 We generated color-depth maximum intensity projections (colorMIPs) of all proofread neurons using the BANC
875 python package (<https://pypi.org/project/banc/>). We registered neuronal reconstructions to
876 JRC2018_Unisex_20x_HR (1210x566 px) and/or JRC2018_VNC_Unisex_40x_DS (573x1119 px), for
877 compatibility with NeuronBridge²⁶².

878 Cell-type matching and annotation

879 Overview

880 Previous studies have invested substantial effort in cell typing both the brain^{5,6,14,17,41} and VNC^{7,8,10}, employing a
881 combination of manual annotation and computational methods. Our approach leverages morphology and
882 connectivity matching to cell type the ~160,000 neurons in the BANC dataset by associating them with
883 published reconstructions, namely FlyWire-FAFB v783¹⁵ and MANC v1.2.1¹¹. We have successfully assigned
884 cell type labels to 53% of BANC neurons (82813 neurons, 74% excluding the optic lobes), with an estimated
885 error rate of ~7% based on sampling 1,000 matched neurons. The mismatched neuron was almost always a
886 similar cell type within the same hemilineage. For the remaining neurons that could not be confidently matched,
887 we have classified them based on gross morphology and identified their closest associated neurons in other
888 datasets with NBLAST. We estimate that ~10% of these unmatched neurons will prove unmatchable due to
889 reconstruction quality issues or developmental differences in neuron wiring. Notably, we estimate that as many
890 as 1177 neurons of the VNC may be sexually dimorphic and cannot be matched well to MANC (which is a VNC
891 sample from a male fly). Our VNC annotation work (A.M, C.K.S et al., in prep) significantly advances
892 connectome analysis by enabling direct comparisons with established identified cell types in the field and
893 facilitating integration with existing datasets, particularly FAFB and MANC, which can be done with FlyWire
894 Codex.

895 Process

896 Using NBLAST³⁹, which quantifies pairwise neuronal similarity by considering both the position and morphology
897 of neuronal arbors and calculating similarity scores by comparing matched morphological segments, we
898 automatically identified potential matches between BANC neurons and those FlyWire-FAFB v783^{15,17} and
899 MANC v1.2.1¹⁰. Following automated NBLAST scoring, we manually reviewed candidate matches. For sensory
900 neurons, ANs and DNs and intrinsic neurons of the brain, this manual review involved co-visualizing the
901 meshes of matched neurons in 3 orthogonal 2D projections and evaluating the correspondence. For ANs and
902 DNs, we followed up this 2D comparison with co-visualization and manual evaluation in 3D using neuroglancer.
903 For intrinsic neurons of the VNC, we also used connectivity to automatically determine their similarity to MANC
904 neurons. When the top matched cell type agreed between NBLAST and connectivity, we assigned the neuron
905 to that cell type; when these potential matches were in conflict, we co-visualized the BANC and MANC neurons
906 in 3D in neuroglancer and manually reviewed them to determine the correct cell type. High NBLAST scores
907 (e.g., above 0.3) generally indicated a strong likelihood of a correct match. Iterative proofreading and matching
908 increased the population of identified cells as sometimes, low NBLAST scores indicated issues with neuron
909 reconstruction, which suggested additional proofreading was necessary.

910

911 For many afferent and efferent neurons, in addition to matching to FAFB and MANC, we used comparisons to
912 the literature and the domain expertise of our authors to determine their cell types and functions. In particular,
913 we identified leg and wing motor neurons by their morphology and connectivity, as previously described⁸. The
914 key identifying features we used were the exit nerve of the axon, the relative trajectory of the primary neurite,
915 the relative position of the soma, and unique features of the dendritic morphology. Front, middle, and hind limb

916 neuropils differ in terms of specific morphology yet the identifying motor neuron features largely retain their
917 relationships, allowing us to identify homologous motor neurons in each neuropil⁹. We confirmed morphological
918 identification by comparing these motor neurons on the basis of the sources of common synaptic input⁸. We
919 identified endocrine neurons of the brain based on morphology and the cosine similarity of their connectivity
920 with each other and with the FAFB endocrine neurons. We used morphological comparisons to the literature to
921 identify the motor neurons of the antennae, eyes, neck, crop, haltere, pharynx, proboscis, pharynx, salivary
922 glands and uterus; octopaminergic effector neurons involved in ovulation; endocrine neurons of the VNC; and
923 chemosensory, tactile and proprioceptive sensory neurons from the head, eyes, antennas, proboscis, legs,
924 abdomen, wings and halteres⁹². In some cases, we used data from the larval fly (putative nociceptive, putative
925 oxygenation and aorta sensory neurons^{10,55,57,58,263–266}) to annotate suspected homologous neurons. Adult
926 nociceptors will be reported (J.J. & J.C.T., in preparation). We subjected chordotonal, campaniform and hair
927 plate neurons of the VNC, including those of Wheeler's organ, the prothoracic organ and the metathoracic
928 organ, to additional careful review and re-annotation^{7,73,267–269}.

929 Neurons of the neck connective

930 We reviewed all profiles in the two seed planes through the neck connective. We successfully proofread 98.3%
931 of the neuronal profiles to 'backbone proofread' status, for a total of 3695 proofread neurons. We then matched
932 these neurons to cell types in FAFB and MANC, as described above. We identified 1841 ANs, of which we
933 matched 1725 (corresponding to 538 cell types), and 1313 DNs, of which we matched 1288 (corresponding to
934 474 cell types). In addition, we identified 13 sensory DNs (afferent axons that enter through a brain nerve and
935 project through the neck connective to the VNC, discussed in more detail here²¹) corresponding to 5 cell types,
936 511 sensory ANs (afferent axons that enter a VNC nerve and project through the neck connective to the brain)
937 corresponding to 39 cell types and 5 efferent ANs (ANs that also project out of other nerves) corresponding to
938 3 cell types, including EAXXX079, which may be the leucokinin ANs in²⁷⁰. For ANs, sensory ANs and efferent
939 ANs, we use the MANC cell type name; for DNs and sensory DNs, we use the FAFB name. When this resulted
940 in the same name for different cell types (which became apparent when considering the full neuron rather than
941 just the brain or VNC half), we appended an underscore and a letter to the FAFB/MANC name. We also
942 identified and proofread 49 efferent neurons of the neck that leave through the cervical nerve. These are neck
943 motor neurons, and we named them as in⁵³. Note that because they do not traverse the entire extent of the
944 neck connective, they are not included in our count of 3695 "backbone proofread" neurons of the neck
945 connective. We do not use sensory or efferent ANs and DNs in our analysis of ANs and DNs. In our review of
946 the neck connective, we identified 31 ANs and DNs that appeared to have developed abnormally or were
947 stochastic in whether they had an ascending/descending arbor. For example, DNge079 on the right-side (in
948 MANC named DNxl080) has a mis-targeted dendrite located in the VNC, rather than the central brain.
949 However, we note that both the left and right IN08B003 neurons are ANs in this dataset but are intrinsic
950 neurons of the VNC in MANC and in FANC. We determined that the cell type DNg28 leaves the brain through
951 the maxillary-labial nerve and after it re-enters through the same nerve, its processes remain outside of the
952 glial sheath surrounding the CNS as it then traverses the neck to envelop the outside of the VNC and target
953 neurohemal release sites. Therefore, we re-classified it from a DN to solely an efferent cell type. As in FAFB,
954 we could not find DNg25, and DNd01 was not a DN but rather a central brain intrinsic neuron²¹. Important prior
955 work bridged a proportion of ANs and DNs between FAFB and MANC using available experimental data²¹,
956 which was a valuable resource of our matching efforts.

957 Annotation taxonomy

958 We annotated neurons hierarchically by flow (afferent, intrinsic, efferent), super class (eg. sensory, motor,
959 visceral/circulatory, ascending, descending), cell class (eg. chordotonal organ neuron, leg motor neuron,
960 kenyon cell), cell subclass (eg. wing steering motor neuron, front leg hair plate neuron, PPL1 dopaminergic
961 neuron), individual cell type, and with associated metadata (region, side, nerve, body part sensory, body part
962 effector, peripheral target type, cell function, cell function detailed, hemilineage, neurotransmitter verified,
963 neuropeptide verified, FAFB v783 match ID, MANC v1.2.1 match ID and other names). The full list of terms
964 used in each category are listed in **Supplementary Data 1**. This framework enabled both broad and
965 fine-grained categorization, such as distinguishing different and specific classes of sensory neurons. We
966 imported annotations from cell type matching to existing *Drosophila* connectomes^{10,15,17} as well as those that

967 proofreaders and the community contributed through a custom Slackbot
 968 (https://github.com/jasper-tms/the-BANC-fly-connectome/blob/main/slackbots/annotation_bot.py) directly to
 969 CAVE, facilitating real-time tagging and collaborative refinement. We updated annotations as proofreading
 970 progressed, and they are publicly available through FlyWire Codex and on CAVE (cell_info and
 971 codex_annotations tables).

972 Influence

973 The influence score²⁷¹ quantifies the influence of the activity of a neuron or group of neurons, called the seed,
 974 on each of the other neurons in the network. It is a measure of steady-state activity, resulting from continuous
 975 stimulation of seed neurons. We compute steady-state activity assuming a linear dynamical model of neural
 976 activity,

977

$$978 \quad \tau \frac{dr(t)}{dt} = -r(t) + Wr(t) + s(t)$$

979

980 where r is the vector of neural activity, W is the connectivity matrix, τ is the network time constant, and s is the
 981 simulated neural stimulation. For each seed, all elements in s corresponding to the seeded neurons are set to
 982 one, while the remaining elements were fixed at zero.

983

984 The weight of each connection is taken as the number of synapses in that connection, normalized by the total
 985 count of input synapses onto the postsynaptic cell in question. That is, if c_{ij} is the synapse count from

986 presynaptic neuron j onto postsynaptic neuron i , then the total input count for neuron i is $N_i = \sum_j c_{ij}$, and the
 987 connectivity weights were set to $w_{ij} = c_{ij}/N_i$. This type of normalization follows previous work and has been
 988 shown to qualitatively capture experimental observations^{41,272}. All connectivity weights are treated as
 989 nonnegative values, because our goal was to generate a proxy for the number of ‘hops’ in a connection, and
 990 previous synaptic hop metrics have been unsigned^{17,22}; moreover, the signs of many connections are still
 991 unknown. To ensure stable neural dynamics, we re-scaled W such that its largest real eigenvalue is 0.99.

992

993 We compute the steady-state solution for the assumed network dynamics by

994

$$995 \quad r_\infty = - (W - I)^{-1} s,$$

996

997 separately for each seed vector s . As W is a highly sparse matrix, we could compute this solution efficiently
 998 using the sparse matrix parallel computing libraries PETSc and SLEPc (<https://petsc.org/release/> and
<https://slepc.upv.es/>).

1000

1001 If the seed is one cell, and we are interested in a single target cell, we simply take the steady-state activity of
 1002 the target r in response to the seed. We define r_{ij} as the steady-state response of target cell j , given
 1003 stimulation of seed cell i . Often, we are interested in pools of related target cells (e.g., a pool of related motor
 1004 neurons). Thus, for a target pool T that contains the indices of the $|T| = N$ target neurons, we take the average

1005 steady-state response of each cell in the target pool, $\bar{r}_T = \frac{1}{N} \sum_{j \in T} r_{ij}$. Similarly, we are often interested in a pool S

1006 of related seed cells, where S contains the seed cells’ indices. Here, we could simulate activity in all seeds
 1007 individually, and average the results. In this case, for a seed pool of size $|S| = M$, the average response is

$$1008 \quad \bar{r}_{T,S} = \frac{1}{NM} \sum_{i \in S, j \in T} r_{ij}$$

1009 Alternatively, because the steady-state solution r_∞ is linear in the seed vector, it is sometimes more convenient
1010 to just simulate activity in all seed cells simultaneously. In this case, if r_j is the response of the j th target cell to

1011 the simultaneous activity of all seed cells, we take $\bar{r}_T = \frac{1}{NM} \sum_{j \in T} r_j$.

1012

1013 In this type of simulated network, \bar{r} will generally decay exponentially as the distance increases between the
1014 seed and the target (in network space). To correct for this, we take the logarithm of \bar{r} . And because $\log(\bar{r})$ is
1015 generally negative, we add a constant c that brings the values of $\log(\bar{r})$ into the nonnegative range, for ease of
1016 display. The resulting value is called the “adjusted influence”:

$$\text{adjusted influence} = \log(\bar{r}) + c$$

1017
1018 We used $c = 24$, because this ensured that all adjusted influence values were non-negative (given that -24 was
1019 approximately the minimum value of $\log(\bar{r})$ we observed). Across the entire CNS, a small and discrete group of
1020 cells had $\log(\bar{r}) < -24$ for any seed, as these cells were not well-connected to the graph; we set these adjusted
1021 influence values to 0.

1022

1023 We confirmed that adjusted influence is proportional to the number of synaptic ‘hops’ separating the seed cells
1024 and target cells, as expected, and this was true for two different published metrics of hops length (**Fig. 2b.** and
1025 **Extended Data Fig. 2a**; see below for details of these previous metrics). Thus, adjusted influence is essentially
1026 a computationally efficient and deterministic method of estimating the effective number of hops separating the
1027 seed and the target. Because the number of hops is an unsigned quantity^{17,22}, it is reasonable that adjusted
1028 influence is also unsigned. As compared to previous metrics of hop number, adjusted influence has several
1029 advantages. First, we have an explicit expression for the steady-state solution, making the computation more
1030 efficient relative to comparable activity propagation approaches^{15,22,41}. Second, the steady-state solution is
1031 linear in the seed vector, such that it can in principle be summed across different seeds.

1032

1033 Rather than taking the steady-state activity as the basis for this influence metric, we also considered using the
1034 initial slope of the neural activity. However, the initial slope turned out to be directly proportional to the chosen
1035 seed vector, which made it unsuitable as a measure to quantify network-wide influences. We furthermore
1036 considered projections of the above dynamics into the top 1000 eigencircuits, similar to previous work⁸², but we
1037 found this truncation to be unsuitable for our purposes to well-approximate the full network dynamics.

1038

1039 We computed the influence scores reported in this paper using Python 3.13.2, and we executed all
1040 computations using a MacBook Pro running macOS Monterey version 12.6.9. The code used to compute the
1041 influence scores is available as a separate Python package (see ‘Code availability’ section).

1042

1043 Alternative metrics of polysynaptic connectivity

1044 For comparison with our influence scores, we used two complementary probabilistic graph traversal algorithms
1045 to model information flow through the CNS. First, we applied the signal cascade approach²², in which activity
1046 propagates from a set of seed neurons to downstream targets based on synapse counts, treated as proxies for
1047 synaptic strength. A key feature of this model is that neurons are activated only once and then enter a
1048 deactivated state, enabling assessment of potential temporal sequences of activation.

1049

1050 Second, we used an information flow model^{15,41}, in which neurons are probabilistically recruited based on the
1051 fraction of synapses received from already recruited neurons. This model allows ongoing activation from
1052 previously active neurons and assigns each neuron a rank that reflects its integration point in the circuit. While
1053 these ranks do not correspond to true physiological latency, this approach enables systematic inference of
1054 information flow directionality and network layering across the CNS.

1055 Spectral clustering

1056 We adapted a spectral clustering algorithm²⁷³ to partition the CNS into modules of highly interconnected cells.
1057 For this analysis, we focused on intrinsic neurons of the central brain and VNC, ANs, DNs, visual

1058 projection neurons, and visual centrifugal neurons. (We chose to exclude optic lobe neurons because they
1059 are so numerous that they end up dominating the analysis.) Starting with these 42,639 cells, we iteratively
1060 pruned cells that did not have at least one input and output partner among the remaining cells (e.g.
1061 because all their input comes from sensory neurons, or all their output goes to motor neurons, etc.). This
1062 left 41,951 cells as the input to this analysis.

1063

1064 To apply spectral clustering, we first specified our population of N cells of interest and a desired number of
1065 clusters k . We then constructed a weighted, undirected graph whose nodes corresponded to these N cells and
1066 whose edge weights were derived from the connectome. More formally, edge $\{i, j\}$ was assigned weight

1067

$$a_{ij} = \frac{1}{2}(w_{ij} + w_{ji})$$

1068

1069 where w_{ij} is the normalized synaptic input from presynaptic cell j to postsynaptic cell i , as defined above. We
1070 then computed the first k eigenvectors of the graph Laplacian, which resulted in a $k \times N$ matrix of unit-norm
1071 eigenvectors X . Each node then received a k -dimensional feature vector that was determined by its loadings
1072 onto the eigenvectors, yielding an $N \times k$ feature matrix Y with entries

1073

$$y_{im} = \frac{x_{mi}}{\sqrt{\sum_m x_{mi}^2}}.$$

1074 Finally, we applied k-means clustering to these feature vectors to assign each node to a cluster. We decided to
1075 use 13 clusters because this produced a coarse-grained division at the approximate level of resolution we
1076 found relevant to our analysis, and also because the resulting cluster divisions largely corresponded to
1077 salient boundaries in the UMAP space of CNS neurons.

1078 Data analysis

1079 Visual projection neuron functions were used to account for different visual information streams as ‘sensors’.
1080 This is an incomplete survey of visual functions bounded by the literature^{123,137,139–152}. We used for
1081 visual_chromatic - aMe12, MeTu3b, MeTu3c, MTe50; visual leg feedback - LT52; visual horizontal wide field
1082 motion - dCH, FD1, FD3, H1, LPT04_HST, LPT21, LPT22, LPT23, LPT26, LPT42_Nod4, Nod1, Nod2, Nod3,
1083 vCH; visual large_objects and visual thin vertical bar - LC15; visual loom - LC16, LC4, LPLC1; visual object
1084 and visual loom - LC12, LC17; visual polarized light - MeMe_e10, MeTu2a, MeTu2b, MeTu3a; visual
1085 small_object - LC10a, LC10b, LC10c, LC10d, LC11, LC13, LC18, LC21; visual small_object,visual_loom -
1086 LC26, LC6, LC9, LPLC2; visual thin vertical bar - LC25, MeTu1; visual vertical wide field motion - LPT27,
1087 LPT28, LPT30, LPT31, LPT45_dCal1, LPT47 vCal2, LPT48 vCal3, LPT49, LPT50, Nod5, V1, vCal1, VST1,
1088 VST2. Sensory neuron cell functions were determined by a literature search and search of extant connectome
1089 meta data, for information on their peripheral sensory organs/structures. Through this manuscript, we clustered
1090 heatmaps using hierarchical clustering based on Ward’s distance using functions from base R. We applied
1091 dynamic tree cut²⁷⁴ (implemented as dynamicTreeCut::cutreeDynamic, using deepSplit = 4) clustering to
1092 UMAPs to delineate effector and AN/DN clusters, other than in **Fig. 6 and Extended Data Fig. 5**, in which
1093 spectral clustering was used, see above. We conducted data analysis in R using the uwot²⁷⁵, tidyverse²⁷⁶ and
1094 ggplot2²⁷⁷ packages. We made the Kernel density estimates for **Fig. 6a** using MASS::kde2d, n=100, cubes with
1095 densities above the first percentile colored²⁷⁸. We calculated cosine similarity using the lsq R package²⁷⁹, and
1096 we applied it to direct connectivity between BANC neurons to build the space used in **Fig. 3**. To perform the
1097 Kolmogorov-Smirnov test in **Fig. 6e**, we used the kstest2 function in MATLAB 2024a (Mathworks).

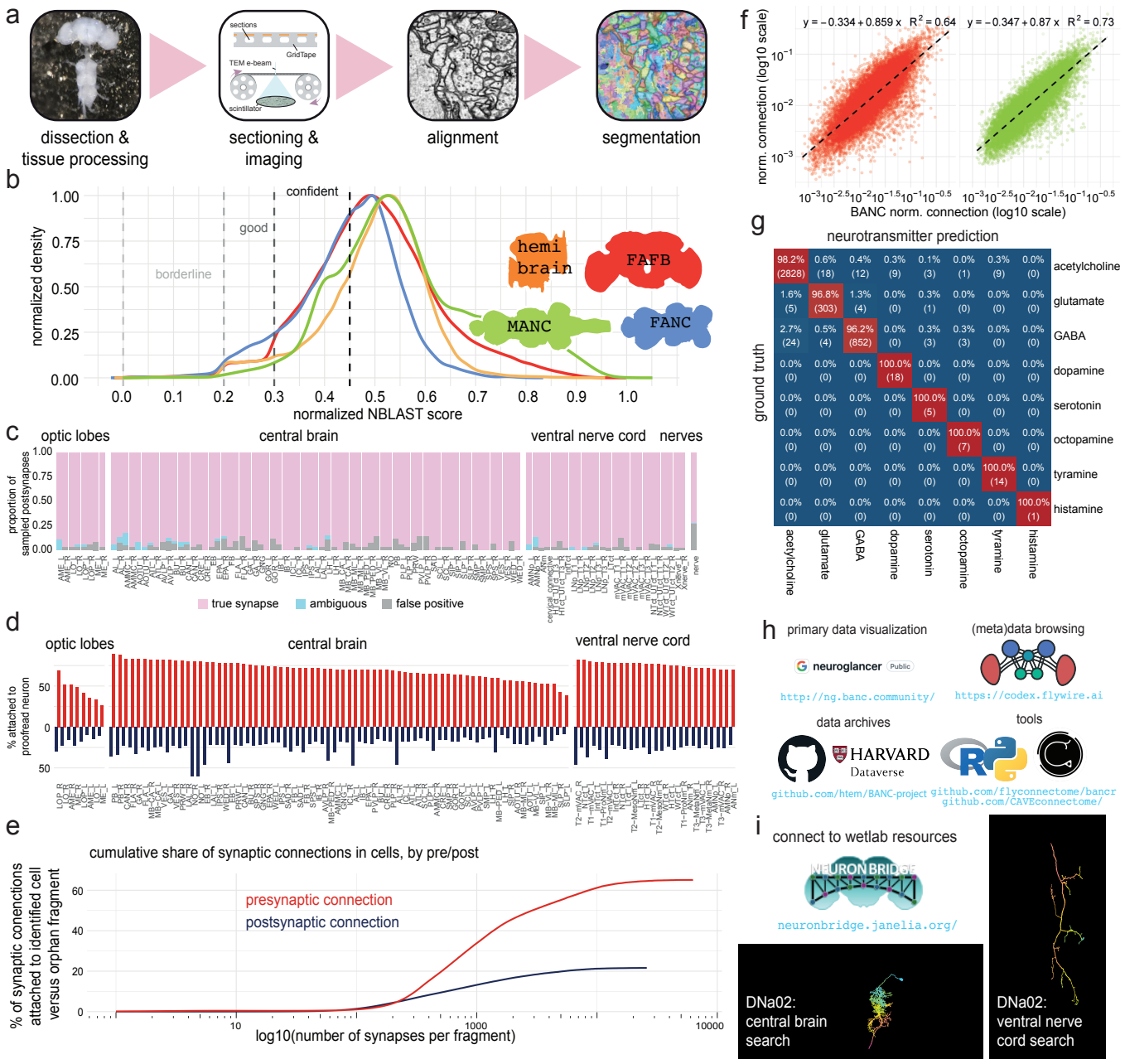
1098 Data availability

1099 Data is freely accessible through multiple platforms. A general overview of the resource and links to these tools
1100 are available at the BANC portal (<https://banc.community>). The FlyWire Codex²⁸⁰ (<https://codex.flywire.ai/banc>)
1101 provides an interactive web interface for exploring the BANC connectome, enabling users to search for
1102 neurons, visualize morphology, traverse synaptic pathways and download metadata such as cell-type
1103 annotations, neurotransmitter predictions and connectivity matrices. Volumetric EM data, including 3D neuron
1104 meshes and annotations, can be viewed at <https://ng.banc.community/view> or accessed programmatically via
1105 CAVE³³. We snapshotted CAVE materialization version 626 (July 21, 2025) for this manuscript. Static data

1106 dumps are also available for download from the Harvard Dataverse (<https://doi.org/10.7910/DVN/8TFGGB>).
1107 Direct downloads include: the synaptic connectivity edgelist, NBLAST results of BANC neurons against
1108 Hemibrain, FAFB, FANC and MANC as well as BANC all-by-all; neuronal L2 skeletons (made using:
1109 https://github.com/CAVEconnectome/pcg_skel); neuronal colorMIPs; influence scores from defined sources as
1110 used in this manuscript and our aligned BANC metadata. Schematics are available here as vector graphics:
1111 <https://github.com/wilson-lab/schematics?tab=readme-ov-file>.

1112 Code availability

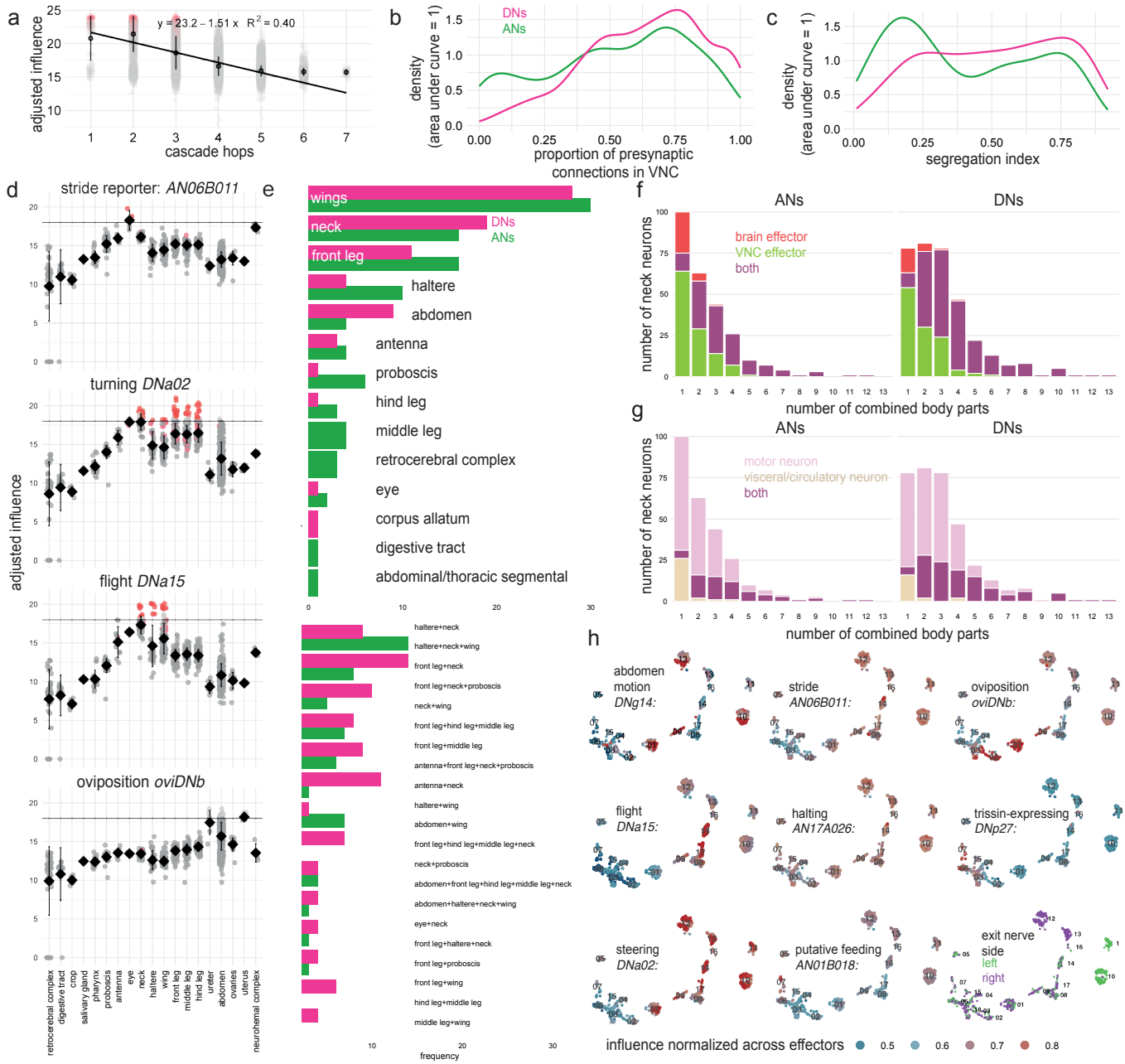
1113 All code developed for this project is open-source and publicly available. Our connectome data is most
1114 accessibly through FlyWire codex, where it is browsable and from where up-to-date direct downloads can be
1115 obtained, as the project progresses (<https://codex.flywire.ai/?dataset=banc>). A comprehensive collection of
1116 community tools and software packages for working with the BANC dataset can be found at the project hub
1117 (<https://banc.community>) and the FlyWire Apps portal (<https://flywire.ai/apps>). The specific code used to
1118 perform the analyses and generate the figures for this manuscript is shared in a dedicated GitHub repository:
1119 <https://github.com/hitem/BANC-project/>. Code for computing influence scores is available at:
1120 <https://doi.org/10.5281/zenodo.15999930>²⁷¹. Code for neurotransmitter predictions is available at:
1121 https://github.com/hitem/synister_banc. We have also made available python code for BANC
1122 (<https://pypi.org/project/banc/>), and an R package, `bancr` (<https://github.com/flyconnectome/bancr>), for
1123 querying BANC data, compatible with the natverse⁷⁸. A static snapshot of the code and analysis tools are also
1124 available on our Harvard Dataverse Dataset (<https://doi.org/10.7910/DVN/8TFGGB>).
1125
1126



1127 Extended Data Figures

1128 Extended Data Fig. 1: central nervous system connectome generation, quality, and neuron identification

- 1129 a. Workflow for serial EM dataset generation. The specimen is dissected and prepared for sectioning and EM imaging. Acquired EM
1130 micrographs are then aligned into a dataset, which is subsequently segmented into cellular fragments.
- 1131 b. Density of the normalized NBLAST scores³⁹ of ‘proofread’ neurons¹⁵ in the BANC against all neurons in other connectomic datasets
1132 (different colors). We consider normalized NBLAST scores > 0.3 as high and suggest score bins to help guide data users (dashed
1133 lines). Normalized NBLAST scores are “raw” NBLAST scores divided by self-match score. All density curves are normalized to their
1134 own peak.
- 1135 c. We sampled 4648 postsynaptic links evenly across 67 standard neuropils^{35,36} for a false positive review (_L, left neuropil, _R, right
1136 neuropil).
- 1137 d. Attachment rates for presynaptic (red) and postsynaptic (navy) links to an identified cell (neuron, glia) across neuropils. We used the
1138 BANC synapse version: synapses_250226.
- 1139 e. The cumulative share of pre- and postsynaptic links in identified cells versus orphan fragments (not part of an identified cell). Plot is
1140 by fragment size as inferred by number of links on fragment (version 626).
- 1141 f. Scatter plots show the correlation between matched pairs of connected cell types in the BANC versus FAFB¹⁵ and MANC¹¹ (and the
1142 most complete extant connectomes). Each point is a cell-type-to-cell-type normalized connection (synaptic connections from
1143 source-to-target / total number of postsynaptic links on the target cell type). FAFB-BANC: 34174 matched cell type connections,
1144 MANC-BANC: 29350 matched cell type connections.
- 1145 g. Confusion matrix of neurotransmitter prediction evaluated at the level of whole neurons on the held-out test set. Whole neuron
1146 prediction is based on the summed classification probabilities across all presynaptic links, selecting the most confident class. The
1147 ground-truth included 20572 neurons (from 2900 cell types, see Methods), of which 16448 were used for training and 4124 for
1148 testing.
- 1149 h. Users can browse BANC data via Codex (codex.flywire.ai/banc), and they can download data for programmatic analysis (via
1150 Codex¹⁵, CAVE³³, and Dataverse at <https://doi.org/10.7910/DVN/8TFGGB>).
- 1151 i. Color-depth MIPs²⁸¹ (maximum intensity projection images where color encodes depth) in JRC2018U space²⁶¹ for BANC dataset
1152 neurons (version 626) available from our Dataverse archive. These can be used to search for genetic driver lines enabling functional
1153 investigation into BANC neurons, for example using NeuronBridge²⁶². Examples are shown for a specific cell type (DNa02).



1154

1155 **Extended Data Fig. 2: Individual DNs and ANs often influence effectors in multiple body parts.**1156 a. **Fig. 2b** shows that the adjusted influence is proportional to ‘layers’ of a published graph traversal model⁴¹ applied to the FAFB
1157 dataset¹⁷. Here we show that the adjusted influence is also proportional to the output of a different published layering algorithm²². As
1158 in **Fig. 2b**, we used olfactory seeds annotated in the FAFB dataset.

1159 b. Distribution of presynaptic links in the VNC versus the brain, for all DNs (1313 cells) and ANs (1841 cells) in the BANC dataset.

1160 c. Distribution of segregation index²⁸² values for these same DNs and ANs. Segregation index is a measure of polarization which
1161 quantifies the entropy of pre- and postsynaptic connections between the axonal and dendritic compartments of a neuron. A
1162 segregation index closer to 1 indicates a more polarized neuron.1163 d. Here we chose three DNs and one AN that have clear behavioral effects, and we examined their adjusted influence on effector cells
1164 in different body parts. Within each subplot, each point is an effector cell, with direct connections in red. The horizontal line marks a
1165 value of 17.18, which we take as a conservative cutoff for “high influence” (see note below). All four cells have some effector
1166 influence above this cutoff. For each cell, the above-cutoff effector influences are compatible with the cell’s function.1167 e. After discarding connections below this cutoff, we counted the number of AN and DN cell types that influence effectors in single body
1168 parts (top) or multiple body parts (bottom). The bottom plot shows only the most common 20 combinations of body parts.1169 f. The number of AN and DN cell types that combine different numbers of body parts. Gross CNS division for combined effectors shown
1170 in color (‘both’ can appear when only one body part is targeted, because neck motor neurons can exist in both the brain and VNC⁵³).

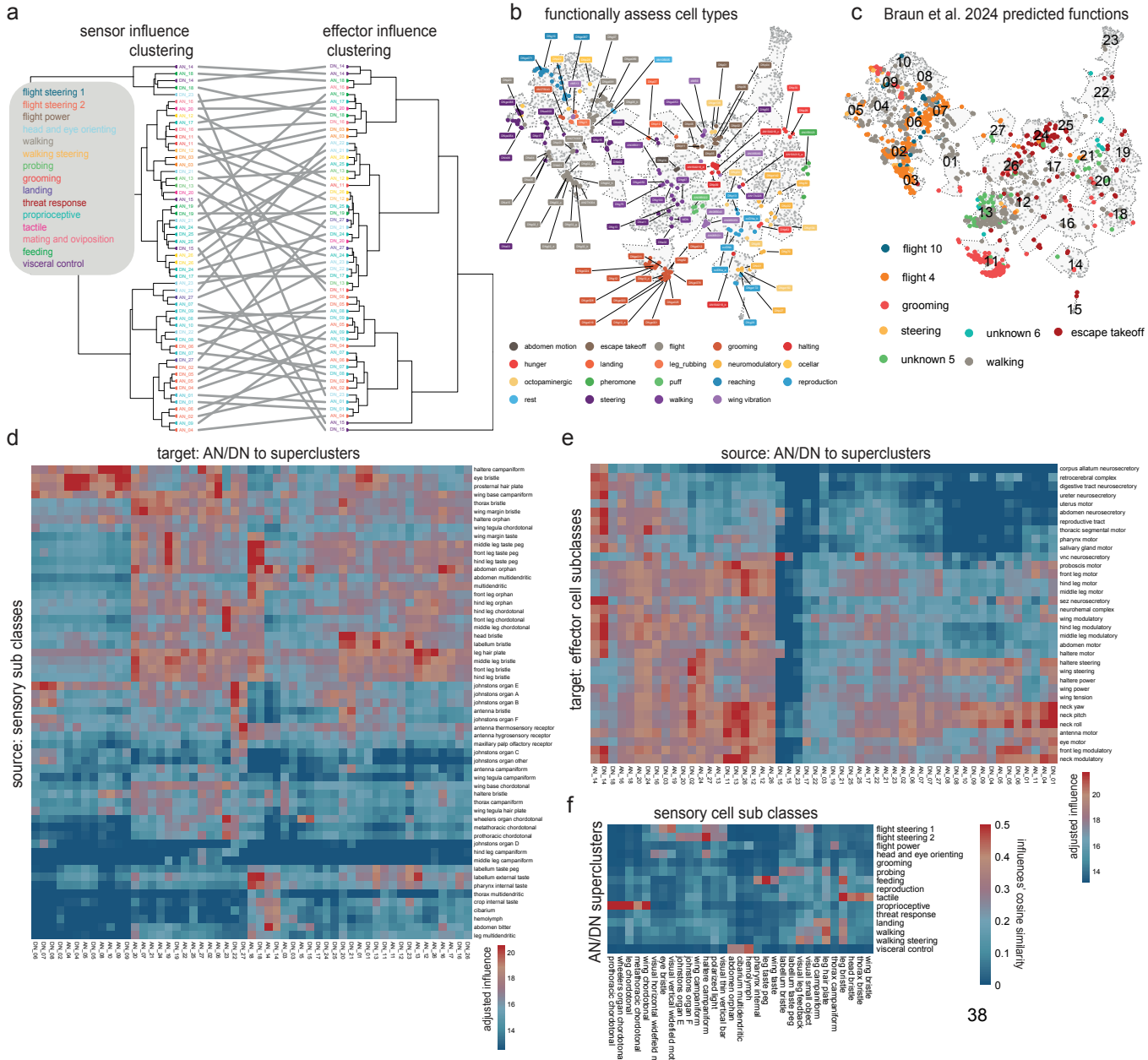
1171 g. Same as (f), but color indicates combinations across motor classes and visceral/circulatory classes.

1172 h. The effector cell map from **Fig. 2i**, color-coded by adjusted influence from example ANs and DNs. Bottom right, cells are color-coded
1173 by the side of the CNS on which their efferent axon exits. Note, we chose this adjusted influence cutoff because it is the “elbow” in the
1174 cumulative distribution of AN/DN-to-effector adjusted influences involving DNs and ANs with known behavioral functions; DNs and
1175 ANs used to identify this elbow were DNA02¹⁰⁴, DNA01¹⁰⁴, DNp01¹¹⁵, DNp02¹¹⁶, MDN (DNp50)⁹⁶, DNp42¹⁰³, DNG97⁹⁷, DNG100⁹⁷,
1176 DNG12¹⁰¹, DNG62⁹⁸, DNp07¹⁰⁰, DNp10¹⁰⁰, DNG14⁹⁵, DNA15¹¹⁴, DNb01¹¹⁴, DNp37¹³³, oviDNb⁷⁰, DNp20¹⁰⁷, DNp22¹⁰⁷, DNp25²⁸³,
1177 DNp44²⁸³, DNp27²²⁵, AN17A026¹⁰⁸ and AN19A018⁹⁷.

1178

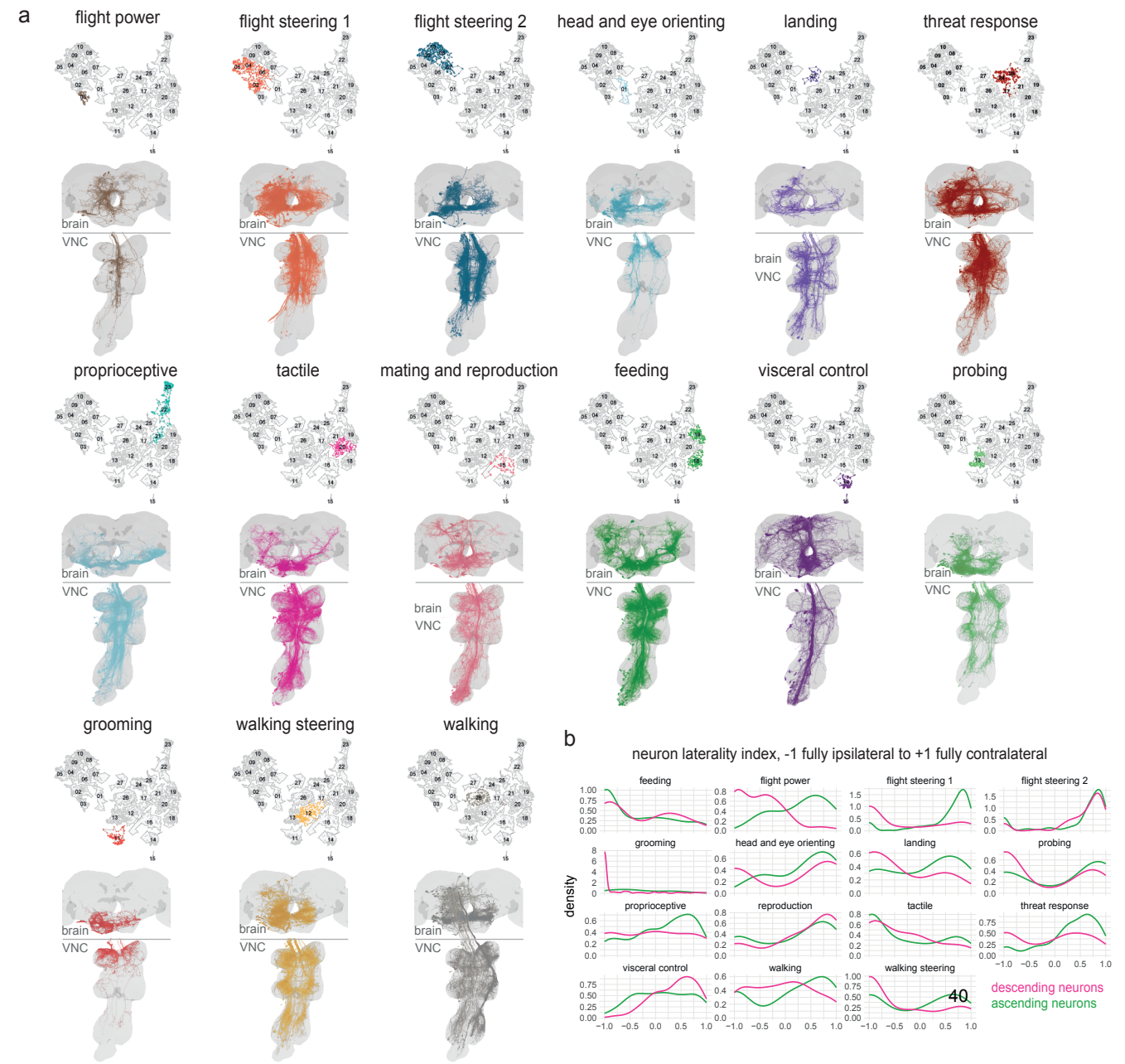
1179

1180



1181 **Extended Data Fig. 3: Influence streams to and from AN/DN clusters**

- 1182 a. Tanglegram showing the relationship between two methods of sorting AN/DN clusters (**Fig. 3a**). The left dendrogram sorts clusters
1183 based on the similarity of their adjusted influences from sensor cell subclasses. The right dendrogram sorts clusters based on the
1184 similarity of their adjusted influence to effector cell subclasses (right). Colors denote superclusters.
1185 b. Names of studied cell types in the field, and their positions in our UMAP space, built by AN/DN direct connectivity to other neurons of
1186 the CNS.
1187 c. Our AN/DN map from **Fig. 3a**, with functions assigned by Braun et al. (2024)⁹⁵. This earlier work only used direct FAFB DN-DN
1188 connectivity, and as a result, functional information was more limited than it is now.
1189 d. Adjusted influence from sensory neuron subclasses onto AN/DN neuron clusters.
1190 e. Adjusted influence from AN/DN clusters onto effector cell subclasses.
1191 f. Similarity of adjusted influence between specific sensory neurons and superclusters. Superclusters are rows; sensory neurons are
1192 columns.



1193

1194 **Extended Data Fig. 4: AN/DN morphologies by supercluster**

1195 a. Each subpanel shows all right-side neurons from one AN/DN supercluster in the UMAP embedding. Neuroglancer links for [flight](#)
1196 [power](#), [flight steering 1](#), [flight steering 2](#), [head and eye orienting](#), [landing](#), [threat response](#), [proprioceptive](#), [tactile](#), [mating and](#)
1197 [reproduction](#), [feeding](#), [visceral control](#), [probing](#), [grooming](#), [walking steering](#) and [walking](#).

1198 b. Distribution laterality index values, for each AN/DN supercluster. Each synaptic connection is signed by the anatomical side of BANC
1199 in which it is found (-1 for left, +1 for right). Laterality index is: $1 - \text{abs}(\text{mean of the postsynaptic score} - \text{mean of the presynaptic}$
1200 $\text{score})$. Each distribution is scaled so that the area under the curve is 1.

1201

1202

1203 Extended Data Fig. 5: CNS networks' cluster influence from sensors and to effectors

- 1204** a. UMAP embedding of BANC neurons, where each point is a neuron. This analysis uses all BANC neurons that meet four criteria: they
1205 are marked as proofread, they are intrinsic neurons of the CNS (not afferents or efferents), they have >100 incoming and outgoing
1206 connections, and no part of the cell is in the optic lobe (as the optic lobes are still undergoing proofreading). In total, 29519 neurons
1207 were used for this analysis, corresponding to 88% of cell-typed central brain and/or VNC intrinsic neurons.
- 1208** b. Proportion of each CNS network belonging to select super classes / cell classes.
- 1209** c. Mean adjusted influence of AN/DN superclusters onto input neurons of the mushroom body and central complex.
- 1210** d. Mean adjusted influence of mushroom body output neurons and central complex output neurons onto AN/DN superclusters.
- 1211** e. Mean adjusted influence of sensors onto CNS networks. Visual projection neuron cell types are included, although they are not
1212 peripheral sensory neurons.
- 1213** f. Mean adjusted influence of CNS networks onto effector cell subclasses.
- 1214** g. Mean adjusted influence of each CNS network into other CNS networks.

1215 Supplementary Data

1216 Supplementary Data 1: Annotations taxonomy

1217 Table of categories of annotations applied to BANC neurons and the list of terms used in each category. For region, side, flow,
1218 super_class, cell_class, cell_sub_class, cell_type, and hemilineage, only one term applies per neuron. For the other categories,
1219 neurons can be labeled with more than one term.

- 1220 • flow - from the perspective of the whole CNS, whether the neuron is afferent, efferent or intrinsic
- 1221 • super_class - coarse division, hierarchical below flow
- 1222 • cell_class - hierarchical below super_class
- 1223 • cell_sub_class - hierarchical below cell_class
- 1224 • cell_type - the name of the matched neuron from FAFB if it is a brain neuron or a DN or the name of the matched neuron from
1225 MANC if it is a VNC neuron or an AN. There are a few exceptions where those names did not define single cell types and were
1226 further split. This is hierarchical below cell_sub_class
- 1227 • region - region of the CNS; all neurons that have arbors in the optic lobe are considered optic_lobe and all neurons that fully transit
the neck connective between the brain and VNC are considered neck_connective
- 1228 • side - from the fly's perspective, the side on which the cell body is located or for afferent neurons, the side of the entry nerve.
- 1229 • cell_function - term briefly describing the function of the neuron, applied largely to afferent and efferent neurons
- 1230 • cell_function_detailed - more detailed information for the function of the neuron than cell_function, also applied largely to afferent
1231 and efferent neurons
- 1232 • peripheral_target_type - the sensor or effector structure/organ targeted by an afferent/efferent neuron.
- 1233 • body_part_sensory - the part of the body innervated by an afferent neuron
- 1234 • body_part_effector - the part of the body targeted by an efferent neuron. If known, this is the site of action when it is different from
1235 the body part innervated (e.g. wing power motor neurons innervate muscles located in the thorax but move the wing)
- 1236 • nerve - peripheral nerve (if applicable)
- 1237 • hemilineage - developmental lineage (NA for many neurons)
- 1238 • neurotransmitter_verified/neuropeptide_verified - neurotransmitter/neuropeptide of neuron, as reported in the literature
- 1239 • fafb_783_match_id/manc_121_match_id - segment ID of neuron from FAFB v783/MANC v1.2.1 that matches the BANC neuron
- 1240 • neurotransmitter_predicted - CNN-predicted primary neurotransmitter
- 1241 • other_names - names given to the neuron that are not the cell_type name

1243 1244 Supplementary Data 2: Updated annotations for FAFB Brain Neurons

1245 Contains metadata for brain neurons from the FAFB-FlyWire dataset that are integrated into BANC analyses. This enables comparison
1246 and integration between the BANC neck connective data and the comprehensive adult brain connectome. Cell type names are
1247 unchanged.

- 1248 • root_783 - FlyWire neuron ID (root_id in FAFB dataset release 783)
- 1249 • nerve - peripheral nerve (if applicable)
- 1250 • hemilineage - developmental lineage (NA for many neurons)
- 1251 • region - region of the CNS; all neurons that have arbors in the optic lobe are considered optic_lobe and all neurons that fully transit
the neck connective between the brain and VNC are considered neck_connective
- 1252 • flow - from the perspective of the whole CNS, whether the neuron is afferent, efferent or intrinsic
- 1253 • super_class - coarse division, hierarchical below flow
- 1254 • cell_class - hierarchical below super_class
- 1255 • cell_sub_class - hierarchical below cell_class
- 1256 • cell_type - Individual cell type name (e.g., ORN_DM6, ORN_VA1v). Not modified from original project
- 1257 • neurotransmitter_predicted - CNN-predicted primary neurotransmitter⁴⁶
- 1258 • neurotransmitter_verified - neurotransmitter, as reported in the literature

1260 1261 Supplementary Data 3: Updated annotations for MANC VNC Neurons

1262 Contains metadata for ventral nerve cord neurons from the MANC dataset that are integrated into BANC analyses. This enables
1263 comparison and integration between the BANC neck connective data and the comprehensive adult VNC connectomes. Cell type names
1264 unchanged.

- 1265 • bodyid - MANC neuron ID from v1.2.1
- 1266 • nerve - Peripheral nerve association (if applicable)
- 1267 • hemilineage - Developmental lineage (NA for many neurons)
- 1268 • region - region of the CNS; all neurons that have arbors in the optic lobe are considered optic_lobe and all neurons that fully transit
the neck connective between the brain and VNC are considered neck_connective
- 1269 • flow - from the perspective of the whole CNS, whether the neuron is afferent, efferent or intrinsic
- 1270 • super_class - coarse division, hierarchical below flow
- 1271 • cell_class - hierarchical below super_class
- 1272 • cell_sub_class - hierarchical below cell_class
- 1273 • cell_type - Individual cell type name (e.g., SNpp50, IN19A001). Not modified from original project
- 1274 • neurotransmitter_predicted - CNN-predicted primary neurotransmitter
- 1275 • neurotransmitter_verified - neurotransmitter, as reported in the literature

1277 1278 Supplementary Data 4: ANs and DNs with UMAP coordinates and cluster assignments

1279 Contains the ANs and DNs, along with their functional clustering based on connectivity patterns (Fig. 3a)

- 1280 • root_id - BANC neuron identifier when used in analysis
- 1281 • root_626 - BANC release v626 specific identifier
- 1282 • supervoxel_id - supervoxel identifier for position
- 1283 • position - 3D coordinates in BANC space (x, y, z in BANC raw voxel space)
- 1284 • UMAP1, UMAP2 - 2D embedding coordinates from connectivity-based UMAP analysis
- 1285 • side - from the fly's perspective, the side on which the cell body is located
- 1286 • region - region of the CNS (primarily neck_connective)
- 1287 • nerve - peripheral nerve (if applicable)
- 1288 • super_class - ascending, descending. Note, we only included flow == 'intrinsic' neurons
- 1289 • hemilineage - developmental lineage
- 1290 • cell_function - functional role description from our literature review
- 1291 • cluster - cluster assignment from **Fig. 3a**. The number defines the cluster identity. Note that ANs have AN_ appended in front of the number and DNs have DN_ appended, but cells with the same number belong to the same cluster, regardless of the prefix
- 1292 • super_cluster - AN/DN superclusters, the named cluster amalgamations used in this paper's figures
- 1293 • cell_type - BANC-specific cell type name, for DNs this preferentially comes from FAFB, for ANs from MANC
- 1294 • fabf_cell_type - corresponding cell type in FAFB dataset
- 1295 • manc_cell_type - corresponding cell type in MANC dataset

1297

1298 **Supplementary Data 5: Effector cells with UMAP coordinates and functional cluster assignments**

1299 Contains all efferent neurons, clustered by their functional properties and target effector systems (**Fig. 2i**). These neurons control 1300 movement, secretion and other output functions.

- 1301 • root_id - BANC neuron identifier when used in analysis
- 1302 • root_626 - BANC release v626 specific identifier
- 1303 • supervoxel_id - supervoxel identifier for position
- 1304 • position - 3D coordinates in BANC space (x, y, z in BANC raw voxel space)
- 1305 • UMAP1, UMAP2 - 2D embedding coordinates from connectivity-based UMAP analysis
- 1306 • side - from the fly's perspective, the side on which the cell body is located
- 1307 • region - region of the CNS
- 1308 • nerve - peripheral nerve
- 1309 • super_class - efferent type (motor, visceral_circulatory)
- 1310 • hemilineage - developmental lineage
- 1311 • cell_function - functional role (e.g. leg_motor, antenna_motor, neck_motor).
- 1312 • cluster - cluster assignment from **Fig. 2i**, as the cluster number with EFF_ appended (e.g., EFF_01)
- 1313 • super_cluster - effector cell groups, the named cluster amalgamations used in this paper's figures.
- 1314 • cell_type - BANC-specific cell type name
- 1315 • fabf_cell_type - corresponding cell type in FAFB dataset
- 1316 • manc_cell_type - corresponding cell type in MANC dataset

1317

1318 **Supplementary Data 6: CNS network analysis with spectral clustering and UMAP embedding**

1319 Contains neurons from spectral clustering analysis of the CNS connectivity (**Fig. 6a**), revealing network-level organisation beyond 1320 individual cell types. This analysis identifies functional networks that span multiple brain regions.

- 1321 • root_id - BANC neuron identifier when used in analysis
- 1322 • root_626 - BANC release v626 specific identifier
- 1323 • supervoxel_id - supervoxel identifier for position
- 1324 • position - 3D coordinates in BANC space (x, y, z in BANC raw voxel space)
- 1325 • UMAP1, UMAP2 - 2D embedding coordinates from connectivity-based UMAP analysis
- 1326 • side - from the fly's perspective, the side on which the cell body is located
- 1327 • region - region of the CNS
- 1328 • nerve - peripheral nerve (if applicable)
- 1329 • super_class - high-level functional category (various types including visual_projection, central_brain_intrinsic)
- 1330 • hemilineage - developmental lineage
- 1331 • cell_function - functional description (if known)
- 1332 • cluster - effector clusters (from **Fig. 2i**), which have the EFF_ prefix, and AN/DN clusters (from **Fig. 3a**), which have the AN_ or 1333 DN_ prefix (if applicable)
- 1334 • super_cluster - name of effector cell group or AN/DN supercluster (if applicable)
- 1335 • cns_network - CNS networks as determined by spectral clustering, 13 cluster cut
- 1336 • cell_type - BANC-specific cell type name
- 1337 • fabf_cell_type - corresponding cell type in FAFB dataset
- 1338 • manc_cell_type - corresponding cell type in MANC dataset

1339

1340 **Supplementary Data 7: Literature review on cell function for ascending, descending and visual projection neurons**

- 1341 • Cell_type - cell type names in the BANC connectome
- 1342 • Other_names - other names used for this cell type in the literature
- 1343 • super_class - high-level functional category, here only ascending, descending and visual projection
- 1344 • Cell_function - simple descriptive label for the 'function' of the cell type
- 1345 • Citations - short hand citations for the work that helped determine cell_function

1346 References

- 1347 1. White, J. G., Southgate, E., Thomson, J. N. & Brenner, S. The structure of the nervous system of the
1348 nematode *Caenorhabditis elegans*. *Philos. Trans. R. Soc. Lond. B Biol. Sci.* **314**, 1–340 (1986).
- 1349 2. Cook, S. J. et al. Whole-animal connectomes of both *Caenorhabditis elegans* sexes. *Nature* **571**, 63–71
1350 (2019).
- 1351 3. Verasztó, C. et al. Whole-body connectome of a segmented annelid larva. *eLife* (2025)
1352 doi:10.7554/elife.97964.2.
- 1353 4. Ryan, K., Lu, Z. & Meinertzhagen, I. A. The CNS connectome of a tadpole larva of *Ciona intestinalis* (L.)
1354 highlights sidedness in the brain of a chordate sibling. *Elife* **5**, (2016).
- 1355 5. Li, F. et al. The connectome of the adult *Drosophila* mushroom body provides insights into function. *Elife* **9**,
1356 (2020).
- 1357 6. Hulse, B. K. et al. A connectome of the *Drosophila* central complex reveals network motifs suitable for
1358 flexible navigation and context-dependent action selection. *Elife* **10**, e66039 (2021).
- 1359 7. Phelps, J. S. et al. Reconstruction of motor control circuits in adult *Drosophila* using automated
1360 transmission electron microscopy. *Cell* (2021) doi:10.1016/j.cell.2020.12.013.
- 1361 8. Azevedo, A. et al. Connectomic reconstruction of a female *Drosophila* ventral nerve cord. *Nature* (2024)
1362 doi:10.1038/s41586-024-07389-x.
- 1363 9. Cheong, H. S. J. et al. Transforming descending input into behavior: The organization of premotor circuits
1364 in the *Drosophila* Male Adult Nerve Cord connectome. (2024) doi:10.7554/elife.96084.1.
- 1365 10. Marin, E. C. et al. Systematic annotation of a complete adult male *Drosophila* nerve cord connectome
1366 reveals principles of functional organisation. *Elife* (2024) doi:0.7554/eLife.97766.1.
- 1367 11. Takemura, S.-Y. et al. A connectome of the male *Drosophila* ventral nerve cord. *Elife* (2024)
1368 doi:10.7554/elife.97769.1.
- 1369 12. Brooks, R. A robust layered control system for a mobile robot. *IEEE J. Robot. Autom.* **2**, 14–23 (1986).
- 1370 13. Maes, P. Modeling adaptive autonomous agents. *Artif. Life* **1**, 135–162 (1993).
- 1371 14. Scheffer, L. K. et al. A connectome and analysis of the adult *Drosophila* central brain. *Elife* **9**, (2020).
- 1372 15. Dorkenwald, S. et al. Neuronal wiring diagram of an adult brain. *Nature* **634**, 124–138 (2024).
- 1373 16. Zheng, Z. et al. A complete electron microscopy volume of the brain of adult *Drosophila melanogaster*. *Cell*
1374 **174**, 730–743.e22 (2018).
- 1375 17. Schlegel, P. et al. Whole-brain annotation and multi-connectome cell typing of *Drosophila*. *Nature* **634**,
1376 139–152 (2024).
- 1377 18. Hsu, C. T. & Bhandawat, V. Organization of descending neurons in *Drosophila melanogaster*. *Sci. Rep.* **6**,
1378 20259 (2016).
- 1379 19. Namiki, S., Dickinson, M. H., Wong, A. M., Korff, W. & Card, G. M. The functional organization of
1380 descending sensory-motor pathways in *Drosophila*. *Elife* **7**, (2018).
- 1381 20. Cande, J. et al. Optogenetic dissection of descending behavioral control in *Drosophila*. *Elife* **7**, (2018).
- 1382 21. Stürner, T. et al. Comparative connectomics of *Drosophila* descending and ascending neurons. *Nature*
1383 **643**, 158–172 (2025).
- 1384 22. Winding, M. et al. The connectome of an insect brain. *Science* **379**, eadd9330 (2023).
- 1385 23. Chen, C.-L. et al. Ascending neurons convey behavioral state to integrative sensory and action selection
1386 brain regions. *Nat. Neurosci.* **26**, 682–695 (2023).
- 1387 24. Cheong, H. S. J. et al. Organization of an ascending circuit that conveys flight motor state in *Drosophila*.
1388 *Curr. Biol.* **34**, 1059–1075.e5 (2024).

- 1389 25. Tuthill, J. C. & Wilson, R. I. Parallel transformation of tactile signals in central circuits of *Drosophila*. *Cell*
1390 **164**, 1046–1059 (2016).
- 1391 26. Strausfeld, N. J. *Arthropod Brains: Evolution, Functional Elegance, and Historical Significance*. (Harvard
1392 University Press, 2012).
- 1393 27. Fiore, V. G., Dolan, R. J., Strausfeld, N. J. & Hirth, F. Evolutionarily conserved mechanisms for the
1394 selection and maintenance of behavioural activity. *Philos. Trans. R. Soc. Lond. B Biol. Sci.* **370**, 20150053
1395 (2015).
- 1396 28. Cisek, P. Resynthesizing behavior through phylogenetic refinement. *Atten. Percept. Psychophys.* **81**,
1397 2265–2287 (2019).
- 1398 29. de Croon, G. C. H. E., Dupeyroux, J. J. G., Fuller, S. B. & Marshall, J. A. R. Insect-inspired AI for
1399 autonomous robots. *Sci. Robot.* **7**, eabl6334 (2022).
- 1400 30. Büschges, A. & Ache, J. M. Motor control on the move: from insights in insects to general mechanisms.
1401 *Physiol. Rev.* **105**, 975–1031 (2025).
- 1402 31. Macrina, T. *et al.* Petascale neural circuit reconstruction: automated methods. *bioRxiv* (2021).
- 1403 32. Dorkenwald, S. *et al.* FlyWire: online community for whole-brain connectomics. *Nat. Methods* **19**, 119–128
1404 (2022).
- 1405 33. Dorkenwald, S. *et al.* CAVE: Connectome Annotation Versioning Engine. *Nat. Methods* **22**, 1112–1120
1406 (2025).
- 1407 34. Hertweck, H. Anatomie und Variabilität des Nervensystems und der Sinnesorgane von. *Drosophila*
1408 *melanogaster* (1931).
- 1409 35. Ito, K. *et al.* A systematic nomenclature for the insect brain. *Neuron* **81**, 755–765 (2014).
- 1410 36. Court, R. *et al.* A systematic nomenclature for the *Drosophila* ventral nerve cord. *Neuron* **107**,
1411 1071–1079.e2 (2020).
- 1412 37. Eichler, K. *et al.* Somatotopic organization among parallel sensory pathways that promote a grooming
1413 sequence in *Drosophila*. *eLife* **12**, RP87602 (2024).
- 1414 38. Matsliah, A. *et al.* Neuronal parts list and wiring diagram for a visual system. *Nature* **634**, 166–180 (2024).
- 1415 39. Costa, M., Manton, J. D., Ostrovsky, A. D., Prohaska, S. & Jefferis, G. S. NBLAST: Rapid, Sensitive
1416 Comparison of Neuronal Structure and Construction of Neuron Family Databases. *Neuron* **91**, 293–311
1417 (2016).
- 1418 40. Schwartzman, G., Jourdan, B., García-Soriano, D. & Matsliah, A. Connectivity is all you need: Inferring
1419 neuronal types with NTAC. *bioRxiv.org* 2025.06.11.659184 (2025) doi:10.1101/2025.06.11.659184.
- 1420 41. Schlegel, P. *et al.* Information flow, cell types and stereotypy in a full olfactory connectome. *eLife* **10**,
1421 (2021).
- 1422 42. Tobin, W. F., Wilson, R. I. & Lee, W. A. Wiring variations that enable and constrain neural computation in a
1423 sensory microcircuit. *eLife* **6**, (2017).
- 1424 43. Takemura, S.-Y. *et al.* Synaptic circuits and their variations within different columns in the visual system of
1425 *Drosophila*. *Proc. Natl. Acad. Sci. U. S. A.* **112**, 13711–13716 (2015).
- 1426 44. Buhmann, J. *et al.* Automatic detection of synaptic partners in a whole-brain *Drosophila* electron
1427 microscopy data set. *Nat. Methods* **18**, 771–774 (2021).
- 1428 45. Yu, S.-C. *et al.* New synapse detection in the whole-brain connectome of *Drosophila*. *bioRxiv*
1429 2025.07.11.664377 (2025) doi:10.1101/2025.07.11.664377.
- 1430 46. Eckstein, N. *et al.* Neurotransmitter classification from electron microscopy images at synaptic sites in
1431 *Drosophila melanogaster*. *Cell* **187**, 2574–2594.e23 (2024).
- 1432 47. McKellar, C. E., Siwanowicz, I., Dickson, B. J. & Simpson, J. H. Controlling motor neurons of every muscle

- 1433 for fly proboscis reaching. *Elife* **9**, (2020).
- 1434 48. Schwarz, O. et al. Motor control of Drosophila feeding behavior. *Elife* **6**, (2017).
- 1435 49. Cui, X., Meiselman, M. R., Thornton, S. N. & Yapici, N. A gut-brain-gut interoceptive circuit loop gates
1436 sugar ingestion in Drosophila. *bioRxivorg* 2024.09.02.610892 (2024).
- 1437 50. Sterne, G. R., Otsuna, H., Dickson, B. J. & Scott, K. Classification and genetic targeting of cell types in the
1438 primary taste and premotor center of the adult Drosophila brain. *Elife* **10**, (2021).
- 1439 51. Suver, M. P., Medina, A. M. & Nagel, K. I. Active antennal movements in Drosophila can tune wind
1440 encoding. *Curr. Biol.* **33**, 780–789.e4 (2023).
- 1441 52. Cury, K. M. & Axel, R. Flexible neural control of transition points within the egg-laying behavioral sequence
1442 in Drosophila. *Nature Neuroscience* **26**, 1054–1067 (2023).
- 1443 53. Gorko, B. et al. Motor neurons generate pose-targeted movements via proprioceptive sculpting. *Nature*
1444 **628**, 596–603 (2024).
- 1445 54. Fenk, L. M. et al. Muscles that move the retina augment compound eye vision in Drosophila. *Nature* **612**,
1446 116–122 (2022).
- 1447 55. Schoofs, A. et al. Serotonergic modulation of swallowing in a complete fly vagus nerve connectome. *Curr.*
1448 *Biol.* **34**, 4495–4512.e6 (2024).
- 1449 56. Qin, J., Yang, T., Li, K., Liu, T. & Zhang, W. Pharyngeal mechanosensory neurons control food swallow in
1450 Drosophila melanogaster. *Elife* **12**, RP88614 (2024).
- 1451 57. Qian, C. S., Kaplow, M., Lee, J. K. & Grueber, W. B. Diversity of internal sensory neuron axon projection
1452 patterns is controlled by the POU-domain protein Pdm3 in Drosophila larvae. *J. Neurosci.* **38**, 2081–2093
1453 (2018).
- 1454 58. Hückesfeld, S. et al. Unveiling the sensory and interneuronal pathways of the neuroendocrine connectome
1455 in Drosophila. *Elife* **10**, (2021).
- 1456 59. Taylor, B. J. Sexually dimorphic neurons of the terminalia of Drosophila melanogaster: II. Sex-specific
1457 axonal arborizations in the central nervous system. *J. Neurogenet.* **5**, 193–213 (1989).
- 1458 60. Reinhard, N. et al. Synaptic connectome of the *Drosophilacircadian clock*. (2023)
1459 doi:10.1101/2023.09.11.557222.
- 1460 61. Deng, B. et al. Chemoconnectomics: Mapping Chemical Transmission in Drosophila. *Neuron* **101**,
1461 876–893.e4 (2019).
- 1462 62. Schlegel, P. et al. Synaptic transmission parallels neuromodulation in a central food-intake circuit. *Elife* **5**,
1463 (2016).
- 1464 63. McKim, T. H. et al. Synaptic connectome of a neurosecretory network in the Drosophila brain. (2024)
1465 doi:10.7554/elife.102684.1.
- 1466 64. Wolff, T. et al. Cell type-specific driver lines targeting the Drosophila central complex and their use to
1467 investigate neuropeptide expression and sleep regulation. *Elife* **14**, (2025).
- 1468 65. Talsma, A. D. et al. Remote control of renal physiology by the intestinal neuropeptide pigment-dispersing
1469 factor in Drosophila. *Proc. Natl. Acad. Sci. U. S. A.* **109**, 12177–12182 (2012).
- 1470 66. Nässel, D. R., Shiga, S., Mohrherr, C. J. & Rao, K. R. Pigment-dispersing hormone-like peptide in the
1471 nervous system of the flies Phormia and Drosophila: immunocytochemistry and partial characterization:
1472 PIGMENT-DISPERSING HORMONE IN FLIES. *J. Comp. Neurol.* **331**, 183–198 (1993).
- 1473 67. Yao, Z. & Scott, K. Serotonergic neurons translate taste detection into internal nutrient regulation. *Neuron*
1474 **110**, 1036–1050.e7 (2022).
- 1475 68. Monastirioti, M. Distinct octopamine cell population residing in the CNS abdominal ganglion controls
1476 ovulation in Drosophila melanogaster. *Dev. Biol.* **264**, 38–49 (2003).

- 1477 69. Rezával, C., Nojima, T., Neville, M. C., Lin, A. C. & Goodwin, S. F. Sexually dimorphic octopaminergic
1478 neurons modulate female postmating behaviors in *Drosophila*. *Curr. Biol.* **24**, 725–730 (2014).
- 1479 70. Wang, F. et al. Neural circuitry linking mating and egg laying in *Drosophila* females. *Nature* **579**, 101–105
1480 (2020).
- 1481 71. Dhawan, S., Huang, Z. & Dickerson, B. H. Neural connectivity of a computational map for fly flight control.
1482 *bioRxiv.org* 2025.05.29.656834 (2025) doi:10.1101/2025.05.29.656834.
- 1483 72. Lesser, E., Moussa, A. & Tuthill, J. C. Peripheral anatomy and central connectivity of proprioceptive
1484 sensory neurons in the *Drosophila* wing. *bioRxiv.org* (2025) doi:10.1101/2025.05.29.656810.
- 1485 73. Lee, S.-Y. J., Dallmann, C. J., Cook, A., Tuthill, J. C. & Agrawal, S. Divergent neural circuits for
1486 proprioceptive and exteroceptive sensing of the *Drosophila* leg. *Nat. Commun.* **16**, 4105 (2025).
- 1487 74. Walker, S. R., Peña-Garcia, M. & Devineni, A. V. Connectomic analysis of taste circuits in *Drosophila*. *Sci.
1488 Rep.* **15**, 5278 (2025).
- 1489 75. Bates, A. S. et al. Complete Connectomic Reconstruction of Olfactory Projection Neurons in the Fly Brain.
1490 *Curr. Biol.* **30**, 3183–3199.e6 (2020).
- 1491 76. Lee, K., Zung, J., Li, P., Jain, V. & Seung, H. S. Superhuman accuracy on the SNEMI3D connectomics
1492 challenge. *arXiv [cs.CV]* (2017).
- 1493 77. Mu, S. et al. 3D reconstruction of cell nuclei in a full *Drosophila* brain. *bioRxiv* 2021.11.04.467197 (2021)
1494 doi:10.1101/2021.11.04.467197.
- 1495 78. Bates, A. S. et al. The natverse, a versatile toolbox for combining and analysing neuroanatomical data.
1496 *Elife* **9**, (2020).
- 1497 79. Bates, A. S., Janssens, J., Jefferis, G. S. & Aerts, S. Neuronal cell types in the fly: single-cell anatomy
1498 meets single-cell genomics. *Curr. Opin. Neurobiol.* **56**, 125–134 (2019).
- 1499 80. Maitin-Shepard, J. et al. *Google/neuroglancer*: (Zenodo, 2021). doi:10.5281/ZENODO.5573294.
- 1500 81. European Organization For Nuclear Research & OpenAIRE. Zenodo. Preprint at
1501 <https://doi.org/10.25495/7GXK-RD71> (2013).
- 1502 82. Pospisil, D. A. et al. The fly connectome reveals a path to the effectome. *Nature* **634**, 201–209 (2024).
- 1503 83. Sadeh, S. & Clopath, C. Theory of neuronal perturbome in cortical networks. *Proc. Natl. Acad. Sci. U. S. A.*
1504 **117**, 26966–26976 (2020).
- 1505 84. Mastrogiuseppe, F. & Ostojic, S. Linking connectivity, dynamics, and computations in low-rank recurrent
1506 neural networks. *Neuron* **99**, 609–623.e29 (2018).
- 1507 85. Sompolinsky, H., Crisanti, A. & Sommers, H. J. Chaos in random neural networks. *Phys. Rev. Lett.* **61**,
1508 259–262 (1988).
- 1509 86. Liu, T. X., Davoudian, P. A., Lizbinski, K. M. & Jeanne, J. M. Connectomic features underlying diverse
1510 synaptic connection strengths and subcellular computation. *Curr. Biol.* **32**, 559–569.e5 (2022).
- 1511 87. Lin, A. et al. Network statistics of the whole-brain connectome of *Drosophila*. *Nature* **634**, 153–165 (2024).
- 1512 88. Manzo, A., Silies, M., Gohl, D. M. & Scott, K. Motor neurons controlling fluid ingestion in *Drosophila*. *Proc.
1513 Natl. Acad. Sci. U. S. A.* **109**, 6307–6312 (2012).
- 1514 89. Nässel, D. R. & Zandawala, M. Hormonal axes in *Drosophila*: regulation of hormone release and
1515 multiplicity of actions. *Cell Tissue Res.* **382**, 233–266 (2020).
- 1516 90. Mirochnikow, A. et al. Convergence of monosynaptic and polysynaptic sensory paths onto common motor
1517 outputs in a *Drosophila* feeding connectome. *Elife* **7**, (2018).
- 1518 91. Dickinson, M. H. & Muijres, F. T. The aerodynamics and control of free flight manoeuvres in *Drosophila*.
1519 *Philos. Trans. R. Soc. Lond. B Biol. Sci.* **371**, (2016).

- 1520 92. Dickerson, B. H., de Souza, A. M., Huda, A. & Dickinson, M. H. Flies regulate wing motion via active
1521 control of a dual-function gyroscope. *Curr. Biol.* **29**, 3517–3524.e3 (2019).
- 1522 93. Lesser, E. *et al.* Synaptic architecture of leg and wing premotor control networks in Drosophila. *Nature*
1523 (2024) doi:10.1038/s41586-024-07600-z.
- 1524 94. Simpson, J. H. Descending control of motor sequences in Drosophila. *Curr. Opin. Neurobiol.* **84**, 102822
1525 (2024).
- 1526 95. Braun, J., Hurtak, F., Wang-Chen, S. & Ramdya, P. Descending networks transform command signals into
1527 population motor control. *Nature* **630**, 686–694 (2024).
- 1528 96. Bidaye, S. S., Machacek, C., Wu, Y. & Dickson, B. J. Neuronal Control of Drosophila Walking Direction.
1529 *Science* **344**, 97–101 (2014).
- 1530 97. Sapkal, N. *et al.* Neural circuit mechanisms underlying context-specific halting in Drosophila. *Nature* **634**,
1531 191–200 (2024).
- 1532 98. Hampel, S., Franconville, R., Simpson, J. H. & Seeds, A. M. A neural command circuit for grooming
1533 movement control. *Elife* **4**, e08758 (2015).
- 1534 99. Bidaye, S. S. *et al.* Two brain pathways initiate distinct forward walking programs in Drosophila. *Neuron*
1535 **108**, 469–485.e8 (2020).
- 1536 100. Ache, J. M., Namiki, S., Lee, A., Branson, K. & Card, G. M. State-dependent decoupling of sensory and
1537 motor circuits underlies behavioral flexibility in *Drosophila*. *Nat. Neurosci.* **22**, 1132–1139 (2019).
- 1538 101. Guo, L., Zhang, N. & Simpson, J. H. Descending neurons coordinate anterior grooming behavior in
1539 Drosophila. *Curr. Biol.* **32**, 823–833.e4 (2022).
- 1540 102. Chen, C.-L. *et al.* Imaging neural activity in the ventral nerve cord of behaving adult *Drosophila*. *Nat.*
1541 *Commun.* **9**, 4390 (2018).
- 1542 103. Huoviala, P. *et al.* Neural circuit basis of aversive odour processing in Drosophila from sensory input to
1543 descending output. *bioRxiv* 394403 (2020) doi:10.1101/394403.
- 1544 104. Rayshubskiy, A. *et al.* Neural circuit mechanisms for steering control in walking Drosophila. (2024)
1545 doi:10.7554/elife.102230.1.
- 1546 105. Yang, H. H. *et al.* Fine-grained descending control of steering in walking Drosophila. *Cell* **187**,
1547 6290–6308.e27 (2024).
- 1548 106. Aimon, S., Cheng, K. Y., Gjorgjieva, J. & Grunwald Kadow, I. C. Global change in brain state during
1549 spontaneous and forced walk in Drosophila is composed of combined activity patterns of different neuron
1550 classes. *Elife* **12**, e85202 (2023).
- 1551 107. Suver, M. P., Huda, A., Iwasaki, N., Safarik, S. & Dickinson, M. H. An array of descending visual
1552 interneurons encoding self-motion in Drosophila. *J. Neurosci.* **36**, 11768–11780 (2016).
- 1553 108. Sen, R., Wang, K. & Dickson, B. J. TwoLumps Ascending neurons mediate touch-evoked reversal of
1554 walking direction in Drosophila. *Curr. Biol.* **29**, 4337–4344.e5 (2019).
- 1555 109. Lillvis, J. L. *et al.* Nested neural circuits generate distinct acoustic signals during Drosophila courtship.
1556 *Curr. Biol.* **34**, 808–824.e6 (2024).
- 1557 110. Fujiwara, T., Brotas, M. & Chiappe, M. E. Walking strides direct rapid and flexible recruitment of visual
1558 circuits for course control in Drosophila. *Neuron* **110**, 2124–2138.e8 (2022).
- 1559 111. Feng, K., Palfreyman, M. T., Häsemeyer, M., Talsma, A. & Dickson, B. J. Ascending SAG neurons control
1560 sexual receptivity of Drosophila females. *Neuron* **83**, 135–148 (2014).
- 1561 112. Kallman, B. R., Kim, H. & Scott, K. Excitation and inhibition onto central courtship neurons biases
1562 Drosophila mate choice. *Elife* **4**, e11188 (2015).
- 1563 113. Clowney, E. J., Iguchi, S., Bussell, J. J., Scheer, E. & Ruta, V. Multimodal chemosensory circuits

- 1564 controlling male courtship in *Drosophila*. *Neuron* **87**, 1036–1049 (2015).
- 1565 114. Ros, I. G., Omoto, J. J. & Dickinson, M. H. Descending control and regulation of spontaneous flight turns in
1566 *Drosophila*. *Curr. Biol.* **34**, 531–540.e5 (2024).
- 1567 115. Lima, S. Q. & Miesenböck, G. Remote control of behavior through genetically targeted photostimulation of
1568 neurons. *Cell* **121**, 141–152 (2005).
- 1569 116. Dombrovski, M. *et al.* Synaptic gradients transform object location to action. *Nature* **613**, 534–542 (2023).
- 1570 117. Zacarias, R., Namiki, S., Card, G. M., Vasconcelos, M. L. & Moita, M. A. Speed dependent descending
1571 control of freezing behavior in *Drosophila melanogaster*. *Nat. Commun.* **9**, 3697 (2018).
- 1572 118. González Segarra, A. J., Pontes, G., Jourjine, N., Del Toro, A. & Scott, K. Hunger- and thirst-sensing
1573 neurons modulate a neuroendocrine network to coordinate sugar and water ingestion. *Elife* **12**, (2023).
- 1574 119. Meiselman, M. R., Ganguly, A., Dahanukar, A. & Adams, M. E. Endocrine modulation of primary
1575 chemosensory neurons regulates *Drosophila* courtship behavior. *PLoS Genet.* **18**, e1010357 (2022).
- 1576 120. Söderberg, J. A. E., Carlsson, M. A. & Nässel, D. R. Insulin-producing cells in the *Drosophila* brain also
1577 express satiety-inducing cholecystokinin-like peptide, drosulfakinin. *Front. Endocrinol. (Lausanne)* **3**, 109
1578 (2012).
- 1579 121. Krashes, M. J. *et al.* A neural circuit mechanism integrating motivational state with memory expression in
1580 *Drosophila*. *Cell* **139**, 416–427 (2009).
- 1581 122. Buchsbaum, E. & Schnell, B. Activity of a descending neuron associated with visually elicited flight
1582 saccades in *Drosophila*. *Curr. Biol.* **35**, 665–671.e4 (2025).
- 1583 123. Kim, H., Park, H., Lee, J. & Kim, A. J. A visuomotor circuit for evasive flight turns in *Drosophila*. *Curr. Biol.*
1584 **33**, 321–335.e6 (2023).
- 1585 124. Babski, H., Codianni, M. & Bhandawat, V. Octopaminergic descending neurons in *Drosophila*:
1586 Connectivity, tonic activity and relation to locomotion. *Heliyon* **10**, e29952 (2024).
- 1587 125. McKellar, C. E. *et al.* Threshold-Based Ordering of Sequential Actions during *Drosophila* Courtship. *Curr.*
1588 *Biol.* **29**, 426–434.e6 (2019).
- 1589 126. Erginkaya, M. *et al.* A competitive disinhibitory network for robust optic flow processing in *Drosophila*. *Nat.*
1590 *Neurosci.* **28**, 1241–1255 (2025).
- 1591 127. Mahishi, D. & Huetteroth, W. The prandial process in flies. *Curr. Opin. Insect Sci.* **36**, 157–166 (2019).
- 1592 128. Semaniuk, U. *et al.* *Drosophila* insulin-like peptides: from expression to functions – a review. *Entomol. Exp.*
1593 *Appl.* **169**, 195–208 (2021).
- 1594 129. Zandawala, M., Marley, R., Davies, S. A. & Nässel, D. R. Characterization of a set of abdominal
1595 neuroendocrine cells that regulate stress physiology using colocalized diuretic peptides in *Drosophila*. *Cell. Mol. Life Sci.* **75**, 1099–1115 (2018).
- 1597 130. Kubrak, O. I., Lushchak, O. V., Zandawala, M. & Nässel, D. R. Systemic corazonin signalling modulates
1598 stress responses and metabolism in *Drosophila*. *Open Biol.* **6**, (2016).
- 1599 131. Jourjine, N., Mullaney, B. C., Mann, K. & Scott, K. Coupled sensing of hunger and thirst signals balances
1600 sugar and water consumption. *Cell* **166**, 855–866 (2016).
- 1601 132. Lehmann, F. O. Matching spiracle opening to metabolic need during flight in *Drosophila*. *Science* **294**,
1602 1926–1929 (2001).
- 1603 133. Wang, K. *et al.* Neural circuit mechanisms of sexual receptivity in *Drosophila* females. *Nature* **589**,
1604 577–581 (2021).
- 1605 134. Berendes, V., Zill, S. N., Büschges, A. & Bockemühl, T. Speed-dependent interplay between local
1606 pattern-generating activity and sensory signals during walking in *Drosophila*. *J. Exp. Biol.* **219**, 3781–3793
1607 (2016).

- 1608 135.Dallmann, C. J. *et al.* Presynaptic inhibition selectively suppresses leg proprioception in behaving
1609 Drosophila. *Neuroscience* (2023).
- 1610 136.Tanaka, R. & Clark, D. A. Neural mechanisms to exploit positional geometry for collision avoidance. *Curr.*
1611 *Biol.* **32**, 2357–2374.e6 (2022).
- 1612 137.Zhao, A. *et al.* A comprehensive neuroanatomical survey of the Drosophila Lobula Plate Tangential
1613 Neurons with predictions for their optic flow sensitivity. *eLife* (2024) doi:10.7554/elife.93659.1.
- 1614 138.Klapoetke, N. C. *et al.* Ultra-selective looming detection from radial motion opponency. *Nature* **551**,
1615 237–241 (2017).
- 1616 139.Hartman, A. K. *et al.* A cell type in the visual system that receives feedback about limb movement. *Curr.*
1617 *Biol.* (2025) doi:10.1016/j.cub.2025.06.055.
- 1618 140.Wei, H., Kyung, H. Y., Kim, P. J. & Desplan, C. The diversity of lobula plate tangential cells (LPTCs) in the
1619 Drosophila motion vision system. *J. Comp. Physiol. A Neuroethol. Sens. Neural Behav. Physiol.* **206**,
1620 139–148 (2020).
- 1621 141.Klapoetke, N. C. *et al.* A functionally ordered visual feature map in the Drosophila brain. *Neuron* **110**,
1622 1700–1711.e6 (2022).
- 1623 142.Wu, M. *et al.* Visual projection neurons in the Drosophila lobula link feature detection to distinct behavioral
1624 programs. *Elife* **5**, e21022 (2016).
- 1625 143.Panser, K. *et al.* Automatic segmentation of Drosophila neural compartments using GAL4 expression data
1626 reveals novel visual pathways. *Curr. Biol.* **26**, 1943–1954 (2016).
- 1627 144.Cazalé-Debat, L. *et al.* Mating proximity blinds threat perception. *Nature* **634**, 635–643 (2024).
- 1628 145.Turner, M. H., Krieger, A., Pang, M. M. & Clandinin, T. R. Visual and motor signatures of locomotion
1629 dynamically shape a population code for feature detection in Drosophila. *Elife* **11**, (2022).
- 1630 146.Sen, R. *et al.* Moonwalker descending neurons mediate visually evoked retreat in *Drosophila*. *Curr. Biol.*
1631 **27**, 766–771 (2017).
- 1632 147.Ribeiro, I. M. A. *et al.* Visual projection neurons mediating directed courtship in Drosophila. *Cell* **174**,
1633 607–621.e18 (2018).
- 1634 148.Hindmarsh Sten, T., Li, R., Otopalik, A. & Ruta, V. Sexual arousal gates visual processing during
1635 Drosophila courtship. *Nature* **595**, 549–553 (2021).
- 1636 149.Tanaka, R. & Clark, D. A. Object-displacement-sensitive visual neurons drive freezing in Drosophila. *Curr.*
1637 *Biol.* **30**, 2532–2550.e8 (2020).
- 1638 150.Garner, D. *et al.* Connectomic reconstruction predicts visual features used for navigation. *Nature* **634**,
1639 181–190 (2024).
- 1640 151.Kind, E. *et al.* Synaptic targets of photoreceptors specialized to detect color and skylight polarization in
1641 Drosophila. *Elife* **10**, (2021).
- 1642 152.Hardcastle, B. J. *et al.* A visual pathway for skylight polarization processing in Drosophila. *Elife* **10**, (2021).
- 1643 153.Geurten, B. R. H., Jähde, P., Corthals, K. & Göpfert, M. C. Saccadic body turns in walking Drosophila.
1644 *Front. Behav. Neurosci.* **8**, 365 (2014).
- 1645 154.Hardcastle, B. J. & Krapp, H. G. Evolution of biological image stabilization. *Curr. Biol.* **26**, R1010–R1021
1646 (2016).
- 1647 155.Dethier, V. G. *The Hungry Fly: A Physiological Study of the Behavior Associated with Feeding*. (Harvard
1648 University Press, Cambridge, Massachusetts, 1976).
- 1649 156.Coates, K. E. *et al.* The wiring logic of an identified serotonergic neuron that spans sensory networks. *J.*
1650 *Neurosci.* **40**, 6309–6327 (2020).
- 1651 157.Baerends, G. P. The functional organization of behaviour. *Anim. Behav.* **24**, 726–738 (1976).

- 1652 158.Tinbergen, N. *The Study of Instinct*. (Oxford University Press, 1951).
- 1653 159.Das, G. et al. Drosophila learn opposing components of a compound food stimulus. *Curr. Biol.* **24**,
1654 1723–1730 (2014).
- 1655 160.Tomchik, S. M. Dopaminergic neurons encode a distributed, asymmetric representation of temperature in
1656 Drosophila. *J. Neurosci.* **33**, 2166–76a (2013).
- 1657 161.Hulse, B. K., Stanoev, A., Turner-Evans, D. B., Seelig, J. D. & Jayaraman, V. A rotational velocity estimate
1658 constructed through visuomotor competition updates the fly's neural compass. *Neuroscience* (2023).
- 1659 162.Westeinde, E. A. et al. Transforming a head direction signal into a goal-oriented steering command. *Nature*
1660 **626**, 819–826 (2024).
- 1661 163.Mussells Pires, P., Zhang, L., Parache, V., Abbott, L. F. & Maimon, G. Converting an allocentric goal into
1662 an egocentric steering signal. *Nature* **626**, 808–818 (2024).
- 1663 164.Cisek, P. Cortical mechanisms of action selection: the affordance competition hypothesis. *Philos. Trans. R.
1664 Soc. Lond. B Biol. Sci.* **362**, 1585–1599 (2007).
- 1665 165.Steinmetz, N. A., Zatka-Haas, P., Carandini, M. & Harris, K. D. Distributed coding of choice, action and
1666 engagement across the mouse brain. *Nature* **576**, 266–273 (2019).
- 1667 166.Kiehn, O. Decoding the organization of spinal circuits that control locomotion. *Nat. Rev. Neurosci.* **17**,
1668 224–238 (2016).
- 1669 167.Kleinfeld, D., Berg, R. W. & O'Connor, S. M. Anatomical loops and their electrical dynamics in relation to
1670 whisking by rat. *Somatosens. Mot. Res.* **16**, 69–88 (1999).
- 1671 168.von Reyn, C. R. et al. A spike-timing mechanism for action selection. *Nat. Neurosci.* **17**, 962–970 (2014).
- 1672 169.Emanuel, S., Kaiser, M., Pflueger, H.-J. & Libersat, F. On the role of the head ganglia in posture and
1673 walking in insects. *Front. Physiol.* **11**, 135 (2020).
- 1674 170.Heinze, S. Unraveling the neural basis of insect navigation. *Current Opinion in Insect Science* vol. 24
1675 58–67 Preprint at <https://doi.org/10.1016/j.cois.2017.09.001> (2017).
- 1676 171.Buchanan, S. M., Kain, J. S. & de Bivort, B. L. Neuronal control of locomotor handedness in Drosophila.
1677 *Proc. Natl. Acad. Sci. U. S. A.* **112**, 6700–6705 (2015).
- 1678 172.Werkhoven, Z., Rohrsen, C., Qin, C., Brembs, B. & de Bivort, B. MARGO (Massively Automated Real-time
1679 GUI for Object-tracking), a platform for high-throughput ethology. *PLoS One* **14**, e0224243 (2019).
- 1680 173.Popovych, S. et al. Petascale pipeline for precise alignment of images from serial section electron
1681 microscopy. *Nat. Commun.* **15**, 289 (2024).
- 1682 174.Saalfeld, S., Fetter, R., Cardona, A. & Tomancak, P. Elastic volume reconstruction from series of ultra-thin
1683 microscopy sections. *Nat. Methods* **9**, 717–720 (2012).
- 1684 175.Turner, N. L. et al. Synaptic partner assignment using attentional voxel association networks. in *2020 IEEE
1685 17th International Symposium on Biomedical Imaging (ISBI)* 1–5 (IEEE, 2020).
- 1686 176.Alekseyenko, O. V., Lee, C. & Kravitz, E. A. Targeted manipulation of serotonergic neurotransmission
1687 affects the escalation of aggression in adult male *Drosophila melanogaster*. *PLoS One* **5**, e10806 (2010).
- 1688 177.Alekseyenko, O. V., Chan, Y.-B., Li, R. & Kravitz, E. A. Single dopaminergic neurons that modulate
1689 aggression in *Drosophila*. *Proc. Natl. Acad. Sci. U. S. A.* **110**, 6151–6156 (2013).
- 1690 178.Brown, M. P. et al. A subclass of evening cells promotes the switch from arousal to sleep at dusk. *Curr.
1691 Biol.* **34**, 2186–2199.e3 (2024).
- 1692 179.Aso, Y. et al. The neuronal architecture of the mushroom body provides a logic for associative learning.
1693 *Elife* 1–47 (2014).
- 1694 180.Barnstedt, O. et al. Memory-Relevant Mushroom Body Output Synapses Are Cholinergic. *Neuron* **89**,
1695 1237–1247 (2016).

- 1696 181. Busch, S., Selcho, M., Ito, K. & Tanimoto, H. A map of octopaminergic neurons in the Drosophila brain. *J. Comp. Neurol.* **513**, 643–667 (2009).
- 1698 182. Aso, Y. *et al.* Nitric oxide acts as a cotransmitter in a subset of dopaminergic neurons to diversify memory dynamics. *Elife* **8**, (2019).
- 1700 183. Cao, C. & Brown, M. R. Localization of an insulin-like peptide in brains of two flies. *Cell Tissue Res.* **304**, 1701 317–321 (2001).
- 1702 184. Carlsson, M. A., Diesner, M., Schachtner, J. & Nässel, D. R. Multiple neuropeptides in the Drosophila 1703 antennal lobe suggest complex modulatory circuits. *J. Comp. Neurol.* **518**, 3359–3380 (2010).
- 1704 185. Cavanaugh, D. J., Vigderman, A. S., Dean, T., Garbe, D. S. & Sehgal, A. The Drosophila circadian clock 1705 gates sleep through time-of-day dependent modulation of sleep-promoting neurons. *Sleep* **39**, 345–356 1706 (2016).
- 1707 186. Certel, S. J. *et al.* Octopamine neuromodulatory effects on a social behavior decision-making network in 1708 Drosophila males. *PLoS One* **5**, e13248 (2010).
- 1709 187. Chen, J. *et al.* Isoform-specific expression of the neuropeptide orcokinin in Drosophila melanogaster. 1710 *Peptides* **68**, 50–57 (2015).
- 1711 188. Chiang, A.-S. *et al.* Three-dimensional reconstruction of brain-wide wiring networks in Drosophila at 1712 single-cell resolution. *Curr. Biol.* **21**, 1–11 (2011).
- 1713 189. Chou, Y.-H. *et al.* Mating-driven variability in olfactory local interneuron wiring. *Sci. Adv.* **8**, eabm7723 1714 (2022).
- 1715 190. Croset, V., Treiber, C. & Waddell, S. Cellular diversity in the Drosophila midbrain revealed by single-cell 1716 transcriptomics. *Elife* **7**, e34550 (2018).
- 1717 191. Dacks, A. M., Christensen, T. A. & Hildebrand, J. G. Phylogeny of a serotonin-immunoreactive neuron in 1718 the primary olfactory center of the insect brain. *J. Comp. Neurol.* **498**, 727–746 (2006).
- 1719 192. Davis, F. P. *et al.* A genetic, genomic, and computational resource for exploring neural circuit function. *Elife* 1720 **9**, (2020).
- 1721 193. Schlichting, M., Díaz, M. M., Xin, J. & Rosbash, M. Neuron-specific knockouts indicate the importance of 1722 network communication to Drosophila rhythmicity. *Elife* **8**, (2019).
- 1723 194. Dolan, M.-J. *et al.* Facilitating Neuron-Specific Genetic Manipulations in Drosophila melanogaster Using a 1724 Split GAL4 Repressor. *Genetics* **206**, 775–784 (2017).
- 1725 195. Dolan, M.-J. *et al.* Neurogenetic dissection of the Drosophila lateral horn reveals major outputs, diverse 1726 behavioural functions, and interactions with the mushroom body. *Elife* **8**, e43079 (2019).
- 1727 196. Syed, S., Duan, Y. & Lim, B. Modulation of protein-DNA binding reveals mechanisms of spatiotemporal 1728 gene control in early Drosophila embryos. *Elife* **12**, (2023).
- 1729 197. Frenkel, L. *et al.* Organization of Circadian Behavior Relies on Glycinergic Transmission. *Cell Rep.* **19**, 1730 72–85 (2017).
- 1731 198. Gao, S. *et al.* The neural substrate of spectral preference in Drosophila. *Neuron* **60**, 328–342 (2008).
- 1732 199. Goda, T. *et al.* Drosophila DH31 neuropeptide and PDF receptor regulate night-onset temperature 1733 preference. *J. Neurosci.* **36**, 11739–11754 (2016).
- 1734 200. Guo, Y., Flegel, K., Kumar, J., McKay, D. J. & Buttitta, L. A. Ecdysone signaling induces two phases of cell 1735 cycle exit in Drosophila cells. *Biol. Open* **5**, 1648–1661 (2016).
- 1736 201. Hasenhuettl, P. S. *et al.* A half-centre oscillator encodes sleep pressure. *bioRxiv* (2024) 1737 doi:10.1101/2024.02.23.581780.
- 1738 202. Haynes, P. R., Christmann, B. L. & Griffith, L. C. A single pair of neurons links sleep to memory 1739 consolidation in Drosophila melanogaster. *Elife* **4**, e03868 (2015).

- 1740 203.Hergarden, A. C., Tayler, T. D. & Anderson, D. J. Allatostatin-A neurons inhibit feeding behavior in adult
1741 *Drosophila*. *Proc. Natl. Acad. Sci. U. S. A.* **109**, 3967–3972 (2012).
- 1742 204.Hermann-Luibl, C., Yoshii, T., Senthilan, P. R., Dirksen, H. & Helfrich-Förster, C. The ion transport peptide
1743 is a new functional clock neuropeptide in the fruit fly *Drosophila melanogaster*. *J. Neurosci.* **34**, 9522–9536
1744 (2014).
- 1745 205.Isaacson, M. D. *et al.* Small-field visual projection neurons detect translational optic flow and support
1746 walking control. *bioRxiv* (2023) doi:10.1101/2023.06.21.546024.
- 1747 206.Ito, M., Masuda, N., Shinomiya, K., Endo, K. & Ito, K. Systematic Analysis of Neural Projections Reveals
1748 Clonal Composition of the *Drosophila* Brain. *Curr. Biol.* **23**, 644–655 (2013).
- 1749 207.Jiang, H. *et al.* Natalisin, a tachykinin-like signaling system, regulates sexual activity and fecundity in
1750 insects. *Proc. Natl. Acad. Sci. U. S. A.* **110**, E3526–34 (2013).
- 1751 208.Jin, X. *et al.* A subset of DN1p neurons integrates thermosensory inputs to promote wakefulness via
1752 CNMa signaling. *Curr. Biol.* **31**, 2075–2087.e6 (2021).
- 1753 209.Johard, H. A. D. *et al.* Intrinsic neurons of *Drosophila* mushroom bodies express short neuropeptide F:
1754 relations to extrinsic neurons expressing different neurotransmitters. *J. Comp. Neurol.* **507**, 1479–1496
1755 (2008).
- 1756 210.Konstantinides, N. *et al.* Phenotypic convergence: Distinct transcription factors regulate common terminal
1757 features. *Cell* **174**, 622–635.e13 (2018).
- 1758 211.Konstantinides, N. *et al.* A complete temporal transcription factor series in the fly visual system. *Nature*
1759 **604**, 316–322 (2022).
- 1760 212.Krzeptowski, W. *et al.* Mesencephalic Astrocyte-derived Neurotrophic Factor regulates morphology of
1761 pigment-dispersing factor-positive clock neurons and circadian neuronal plasticity in *Drosophila*
1762 *melanogaster*. *Front. Physiol.* **12**, 705183 (2021).
- 1763 213.Landayan, D., Wang, B. P., Zhou, J. & Wolf, F. W. Thirst interneurons that promote water seeking and limit
1764 feeding behavior in *Drosophila*. *Elife* **10**, (2021).
- 1765 214.Lee, Y.-J. *et al.* Conservation and divergence of related neuronal lineages in the *Drosophila* central brain.
1766 *Elife* **9**, (2020).
- 1767 215.Liang, L. *et al.* GABAergic Projection Neurons Route Selective Olfactory Inputs to Specific Higher-Order
1768 Neurons. *Neuron* **79**, 917–931 (2013).
- 1769 216.Liu, X. & Davis, R. L. The GABAergic anterior paired lateral neuron suppresses and is suppressed by
1770 olfactory learning. *Nat. Neurosci.* **12**, 53–59 (2009).
- 1771 217.Lu, J. *et al.* Transforming representations of movement from body- to world-centric space. *Nature* **601**,
1772 98–104 (2022).
- 1773 218.Ma, D. *et al.* A transcriptomic taxonomy of *Drosophila* circadian neurons around the clock. *Elife* **10**, (2021).
- 1774 219.Mao, Z. & Davis, R. L. Eight different types of dopaminergic neurons innervate the *Drosophila* mushroom
1775 body neuropil: anatomical and physiological heterogeneity. *Front. Neural Circuits* **3**, 5 (2009).
- 1776 220.Mao, R. *et al.* Conditional chemoconnectomics (cCCTomics) as a strategy for efficient and conditional
1777 targeting of chemical transmission. *Elife* **12**, (2024).
- 1778 221.Martelli, C. *et al.* SIFamide Translates Hunger Signals into Appetitive and Feeding Behavior in *Drosophila*.
1779 (2017) doi:10.1016/j.celrep.2017.06.043.
- 1780 222.Matheson, A. M. M. *et al.* Addendum: A neural circuit for wind-guided olfactory navigation. *Nat. Commun.*
1781 **15**, 1903 (2024).
- 1782 223.Mattaliano, M. D., Montana, E. S., Parisky, K. M., Littleton, J. T. & Griffith, L. C. The *Drosophila* ARC
1783 homolog regulates behavioral responses to starvation. *Mol. Cell. Neurosci.* **36**, 211–221 (2007).

- 1784 224. Mauss, A. S., Meier, M., Serbe, E. & Borst, A. Optogenetic and pharmacologic dissection of feedforward
1785 inhibition in *Drosophila* motion vision. *J. Neurosci.* **34**, 2254–2263 (2014).
- 1786 225. Meiselman, M. R. et al. Recovery from cold-induced reproductive dormancy is regulated by
1787 temperature-dependent AstC signaling. *Curr. Biol.* **32**, 1362–1375.e8 (2022).
- 1788 226. Meschi, E., Duquenoy, L., Otto, N., Dempsey, G. & Waddell, S. Compensatory enhancement of input
1789 maintains aversive dopaminergic reinforcement in hungry *Drosophila*. *Neuron* **112**, 2315–2332.e8 (2024).
- 1790 227. Mollá-Albaladejo, R., Jiménez-Caballero, M. & Sánchez-Alcañiz, J. A. Molecular characterization of
1791 gustatory second-order neurons reveals integrative mechanisms of gustatory and metabolic information.
1792 (2024) doi:10.7554/elife.100947.1.
- 1793 228. Nässel, D. R. & Elekes, K. Aminergic neurons in the brain of blowflies and *Drosophila*: dopamine- and
1794 tyrosine hydroxylase-immunoreactive neurons and their relationship with putative histaminergic neurons.
1795 *Cell Tissue Res.* **267**, 147–167 (1992).
- 1796 229. Nässel, D. R., Enell, L. E., Santos, J. G., Wegener, C. & Johard, H. A. D. A large population of diverse
1797 neurons in the *Drosophila* central nervous system expresses short neuropeptide F, suggesting multiple
1798 distributed peptide functions. *BMC Neurosci.* **9**, 90 (2008).
- 1799 230. Ni, J. D. et al. Differential regulation of the *Drosophila* sleep homeostat by circadian and arousal inputs.
1800 *Elife* **8**, (2019).
- 1801 231. Niens, J. et al. Dopamine Modulates Serotonin Innervation in the *Drosophila* Brain. *Front. Syst. Neurosci.*
1802 **11**, 76 (2017).
- 1803 232. Palavicino-Maggio, C. B., Chan, Y.-B., McKellar, C. & Kravitz, E. A. A small number of cholinergic neurons
1804 mediate hyperaggression in female *Drosophila*. *Proceedings of the National Academy of Sciences* **116**,
1805 17029–17038 (2019).
- 1806 233. Pooryasin, A. & Fiala, A. Identified serotonin-releasing neurons induce behavioral quiescence and
1807 suppress mating in *Drosophila*. *J. Neurosci.* **35**, 12792–12812 (2015).
- 1808 234. Scheunemann, L., Plaçais, P.-Y., Dromard, Y., Schwärzel, M. & Preat, T. Dunce Phosphodiesterase Acts
1809 as a Checkpoint for *Drosophila* Long-Term Memory in a Pair of Serotonergic Neurons. *Neuron* **98**,
1810 350–365.e5 (2018).
- 1811 235. Scott, R. L. et al. Non-canonical ecdision hormone-expressing cells regulate *Drosophila* ecdysis. *iScience*
1812 **23**, 101108 (2020).
- 1813 236. Shang, Y., Claridge-Chang, A., Sjulson, L., Pypaert, M. & Miesenböck, G. Excitatory local circuits and their
1814 implications for olfactory processing in the fly antennal lobe. *Cell* **128**, 601–612 (2007).
- 1815 237. Shinomiya, K. et al. Candidate neural substrates for off-edge motion detection in *Drosophila*. *Curr. Biol.* **24**,
1816 1062–1070 (2014).
- 1817 238. Sinakevitch, I. & Strausfeld, N. J. Comparison of octopamine-like immunoreactivity in the brains of the fruit
1818 fly and blow fly. *J. Comp. Neurol.* **494**, 460–475 (2006).
- 1819 239. Sitaraman, D. et al. Serotonin is necessary for place memory in *Drosophila*. *Proc. Natl. Acad. Sci. U. S. A.*
1820 **105**, 5579–5584 (2008).
- 1821 240. Sizemore, T. R., Jonaitis, J. & Dacks, A. M. Heterogeneous receptor expression underlies non-uniform
1822 peptidergic modulation of olfaction in *Drosophila*. *Nat. Commun.* **14**, 5280 (2023).
- 1823 241. Song, T. et al. Dietary cysteine drives body fat loss via FMRFamide signaling in *Drosophila* and mouse.
1824 *Cell Res.* **33**, 434–447 (2023).
- 1825 242. Sun, L., Jiang, R. H., Ye, W. J., Rosbash, M. & Guo, F. Recurrent circadian circuitry regulates central brain
1826 activity to maintain sleep. *Neuron* **110**, 2139–2154.e5 (2022).
- 1827 243. Takemura, S.-Y. et al. Cholinergic circuits integrate neighboring visual signals in a *Drosophila* motion
1828 detection pathway. *Curr. Biol.* **21**, 2077–2084 (2011).

- 1829 244. Shinomiya, K. *et al.* A common evolutionary origin for the ON- and OFF-edge motion detection pathways
1830 of the Drosophila visual system. *Front. Neural Circuits* **9**, 33 (2015).
- 1831 245. Tanaka, N. K., Endo, K. & Ito, K. Organization of antennal lobe-associated neurons in adult Drosophila
1832 melanogaster brain. *J. Comp. Neurol.* **520**, 4067–4130 (2012).
- 1833 246. Turner-Evans, D. B. *et al.* The Neuroanatomical Ultrastructure and Function of a Biological Ring Attractor.
1834 *Neuron* **108**, 145–163.e10 (2020).
- 1835 247. Raghu, S. V. & Borst, A. Candidate glutamatergic neurons in the visual system of Drosophila. *PLoS One* **6**,
1836 e19472 (2011).
- 1837 248. Vitzthum, H., Homberg, U. & Agricola, H. Distribution of Dip-allatostatin I-like immunoreactivity in the brain
1838 of the locust *Schistocerca gregaria* with detailed analysis of immunostaining in the central complex. *J.*
1839 *Comp. Neurol.* **369**, 419–437 (1996).
- 1840 249. Waddell, S., Douglas Armstrong, J., Kitamoto, T., Kaiser, K. & Quinn, W. G. The amnesiac Gene Product Is
1841 Expressed in Two Neurons in the Drosophila Brain that Are Critical for Memory. *Cell* **103**, 805–813 (2000).
- 1842 250. Winther, A. M. E., Siviter, R. J., Isaac, R. E., Predel, R. & Nässel, D. R. Neuronal expression of
1843 tachykinin-related peptides and gene transcript during postembryonic development of Drosophila: TRP
1844 and Gene Transcript Expression in Drosophila. *J. Comp. Neurol.* **464**, 180–196 (2003).
- 1845 251. Wu, Y., Bidaye, S. S. & Mahringer, D. Drosophilafemale-specific brain neuron elicits persistent position-
1846 and direction-selective male-like social behaviors. (2019) doi:10.1101/594960.
- 1847 252. Xie, X. *et al.* The laminar organization of the Drosophila ellipsoid body is semaphorin-dependent and
1848 prevents the formation of ectopic synaptic connections. *Elife* **6**, (2017).
- 1849 253. Yurgel, M. E. *et al.* A single pair of leucokinin neurons are modulated by feeding state and regulate
1850 sleep-metabolism interactions. *PLoS Biol.* **17**, e2006409 (2019).
- 1851 254. Nern, A. *et al.* Connectome-driven neural inventory of a complete visual system. *Nature* **641**, 1225–1237
1852 (2025).
- 1853 255. Jones, J. D. *et al.* The dorsal fan-shaped body is a neurochemically heterogeneous sleep-regulating center
1854 in Drosophila. *PLoS Biol.* **23**, e3003014 (2025).
- 1855 256. He, K., Zhang, X., Ren, S. & Sun, J. Deep residual learning for image recognition. *arXiv [cs.CV]* (2015)
1856 doi:10.48550/ARXIV.1512.03385.
- 1857 257. Kingma, D. P. & Ba, J. Adam: A method for stochastic optimization. *arXiv [cs.LG]* (2014)
1858 doi:10.48550/ARXIV.1412.6980.
- 1859 258. Lin, T.-Y., Goyal, P., Girshick, R., He, K. & Dollár, P. Focal Loss for dense object detection. *arXiv [cs.CV]*
1860 (2017) doi:10.48550/ARXIV.1708.02002.
- 1861 259. Dale, H. Pharmacology and nerve-endings (Walter Ernest Dixon Memorial Lecture): (section of
1862 therapeutics and pharmacology). *Proc. R. Soc. Med.* **28**, 319–332 (1935).
- 1863 260. Sherer, L. M. *et al.* Octopamine neuron dependent aggression requires dVGLUT from dual-transmitting
1864 neurons. *PLoS Genet.* **16**, e1008609 (2020).
- 1865 261. Bogovic, J. A. *et al.* An unbiased template of the Drosophila brain and ventral nerve cord. *PLoS One* **15**,
1866 e0236495 (2020).
- 1867 262. Clements, J. *et al.* NeuronBridge: an intuitive web application for neuronal morphology search across large
1868 data sets. *BMC Bioinformatics* **25**, 114 (2024).
- 1869 263. Lu, S., Qian, C. S. & Grueber, W. B. Mechanisms of gas sensing by internal sensory neurons in Drosophila
1870 larvae. *bioRxiv.org* 2024.01.20.576342 (2024) doi:10.1101/2024.01.20.576342.
- 1871 264. Liu, Z. *et al.* Drosophila mechanical nociceptors preferentially sense localized poking. *Elife* **11**, (2022).
- 1872 265. Zhong, L., Hwang, R. Y. & Tracey, W. D. Pickpocket is a DEG/ENaC protein required for mechanical

- 1873 nociception in Drosophila larvae. *Curr. Biol.* **20**, 429–434 (2010).
- 1874 266.Guo, Y., Wang, Y., Wang, Q. & Wang, Z. The role of PPK26 in Drosophila larval mechanical nociception.
- 1875 *Cell Rep.* **9**, 1183–1190 (2014).
- 1876 267.Merritt, D. J. & Murphrey, R. K. Projections of leg proprioceptors within the CNS of the fly *Phormia* in
- 1877 relation to the generalized insect ganglion. *J. Comp. Neurol.* **322**, 16–34 (1992).
- 1878 268.Agrawal, S. *et al.* Central processing of leg proprioception in Drosophila. *Elife* **9**, (2020).
- 1879 269.Pratt, B. G. *et al.* Proprioceptive limit detectors mediate sensorimotor control of the Drosophila leg.
- 1880 *bioRxivorg* (2025) doi:10.1101/2025.05.15.654260.
- 1881 270.Chen, J. *et al.* A hormone-to-neuropeptide pathway inhibits sexual receptivity in immature Drosophila
- 1882 females. *Proc. Natl. Acad. Sci. U. S. A.* **122**, e2418481122 (2025).
- 1883 271.Ajabi, Z., Bates, A. S. & Drugowitsch, J. *Connectome Influence Calculator*. (Zenodo, 2025).
- 1884 doi:10.5281/ZENODO.15999930.
- 1885 272.Mayzel, J. & Schneidman, E. Homeostatic synaptic normalization optimizes learning in network models of
- 1886 neural population codes. *Elife* **13**, (2024).
- 1887 273.Ng, A., Jordan, M. I. & Weiss, Y. On spectral clustering: Analysis and an algorithm. *Neural Inf Process Syst*
- 1888 **14**, 849–856 (2001).
- 1889 274.dynamicTreeCut: Methods for Detection of Clusters in Hierarchical Clustering Dendrograms.
- 1890 *Comprehensive R Archive Network (CRAN)* <https://CRAN.R-project.org/package=dynamicTreeCut>.
- 1891 275.Melville, J. The Uniform Manifold Approximation and Projection (UMAP) Method for Dimensionality
- 1892 Reduction [R package uwot version 0.2.3]. *Comprehensive R Archive Network (CRAN)*
- 1893 <https://CRAN.R-project.org/package=uwot> (2025).
- 1894 276.Wickham, H. *et al.* Welcome to the tidyverse. *Journal of Open Source Software* vol. 4 1686 Preprint at
- 1895 <https://doi.org/10.21105/joss.01686> (2019).
- 1896 277.Wickham, H. Ggplot2. *Wiley Interdiscip. Rev. Comput. Stat.* **3**, 180–185 (2011).
- 1897 278.Support Functions and Datasets for Venables and Ripley's MASS [R package MASS version 7.3-65].
- 1898 *Comprehensive R Archive Network (CRAN)* <https://CRAN.R-project.org/package=MASS> (2025).
- 1899 279.lsa: Latent Semantic Analysis. *Comprehensive R Archive Network (CRAN)*
- 1900 <https://CRAN.R-project.org/package=lsa>.
- 1901 280.Matsliah, A. *et al.* Codex: Connectome Data Explorer. (2023) doi:10.13140/RG.2.2.35928.67844.
- 1902 281.Otsuna, H., Ito, M. & Kawase, T. Color depth MIP mask search: a new tool to expedite Split-GAL4 creation.
- 1903 *bioRxiv* 318006 (2018) doi:10.1101/318006.
- 1904 282.Schneider-Mizell, C. M. *et al.* Quantitative neuroanatomy for connectomics in Drosophila. *Elife* **5**, (2016).
- 1905 283.Marin, E. C. *et al.* Connectomics Analysis Reveals First-, Second-, and Third-Order Thermosensory and
- 1906 Hygrosensory Neurons in the Adult Drosophila Brain. *Curr. Biol.* **30**, 3167–3182.e4 (2020).
- 1907